© Daniel Aja

University of Cape Coast

UNIVERSITY OF CAPE COAST

MODELING THE EFFECTS OF LAND COVER MODIFICATIONS AND

SEA LEVEL RISE ON COASTAL MANGROVE PRODUCTIVITY: A

CASE STUDY OF ANLO BEACH COMPLEX WETLAND, WESTERN

REGION, GHANA

BY

DANIEL AJA

Dissertation submitted to the Department of Fisheries and Aquatic Sciences,

School of Biological Sciences, College of Agriculture and Natural Sciences,

University of Cape Coast in partial fulfillment of the requirements for the
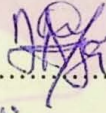
award of PhD in Integrated Coastal Zone Management

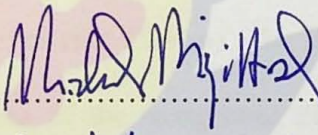SEPTEMBER 2022

DECLARATION

Candidate's Declaration

I hereby declare that this dissertation is the result of my original research and that no part of it has been presented for another degree in this university or elsewhere.
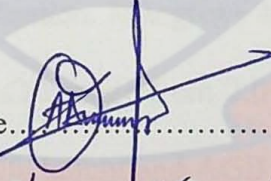
Candidate's Signature................................ Date...19/06/23.........

Name...Daniel Aja...

Supervisors' Declaration

We hereby declare that the preparation and presentation of this dissertation were supervised in accordance with the guidelines on supervision of dissertation laid down by the University of Cape Coast.

Principal Supervisor's Signature............................... Date...19. June. 2023

Name.....Dr. Michael Miyittah.............................

Co-supervisor's Signature............................... Date...20- 6 - 2023

Name...Dr. Donatus Bapentire Angnuureng.............

ABSTRACT

In this work, the underlying mechanisms in coastal wetlands were examined in relation to the long-term mangroves' response to anthropogenic activities and sea level rise. Geographic information systems and dynamic modeling methodologies were used. The complexity of mangroves makes it difficult to assess mangrove forests in tropical coastal locations using simply passive remote sensing techniques. In order to overcome these difficulties, a unique GIS method called GEE that combines optical satellite imagery and synthetic aperture radar was introduced. The effect of tidal currents on the mangrove ecosystem was investigated using a process-based model. Three model scenarios of 100 tidal cycle each were run, with three variables consisting of no sea level rise (constant), low sea level rise (0.3 m), and extremely high sea level rise (2.5 m). The findings indicate that between 2009 and 2019, the area of the mangroves decreased by roughly 16.9%. Overall accuracy of 99.1%, 84.6%, and 98.9% were recorded for three scenarios of 2019 classification. Mangrove height and AGB show that in year 2000, height and AGB range from 2.0 to 12.7 m and 0 - 368 mg ha^{-1}, respectively, while in 2020, height and AGB ranged from 2.0 - 6.3 m and 0 − 88 mg ha^{-1} respectively. The dynamic modeling results show that the relative hydro-period for the scenarios "no sea level rise (constant)", "low sea level rise (0.3 m)" and "extremely high sea level rise (2.5 m)" was 64%, 65% and 71%, respectively.
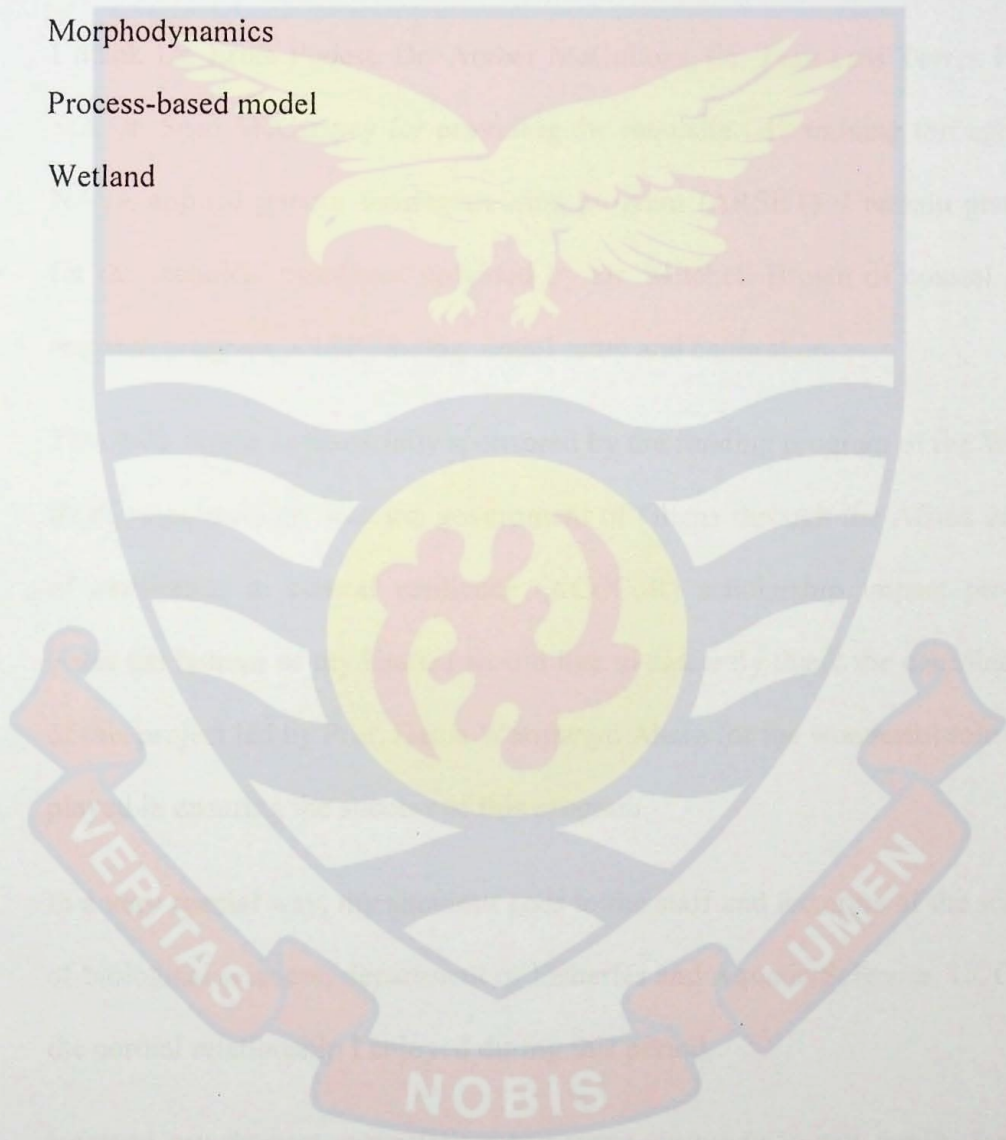
KEYWORDS

Google earth engine

Hydrodynamics

Hydroperiod

Mangrove ecosystem

Morphodynamics

Process-based model

Wetland

ACKNOWLEDGEMENTS

My heartfelt gratitude goes to my supervisors in the persons of Dr. Michael Miyittah and Dr. Donatus Bapentire Angnuureng for their time and in-depth contributions from day one to the completion of this work. I really enjoyed their wealth of knowledge and insightful advices.

I thank Dr. Erika Podest, Dr. Amber McCullum, Dr. Juan Luis Torres Perez and Dr. Sean McCartney for providing the requisite GIS training through the NASA applied remote sensing training program (ARSET). I remain grateful for the technical assistance provided by Dr. Mitchell Brown of coastal inlet research program (CIRP) during model setup and calibration.

This PhD degree is financially sponsored by the funding program of the World Bank in partnership with the government of Ghana through the Africa center of excellence in coastal resilience (ACECoR) scholarship impact project. From the bottom of my heart, I would like to sincerely thank the coordinators of this project led by Prof. Denis Wornlanyo Aheto for the wonderful role they played in ensuring the success of this program.

In a very special way, my shoutout goes to the staff and lecturers of the school of biological sciences, department of Fisheries and Aquatic Sciences, UCC for the cordial relationship I enjoyed during this period.

I extend my deepest appreciation and warm gratitude to my family for the support and prayers during this period.
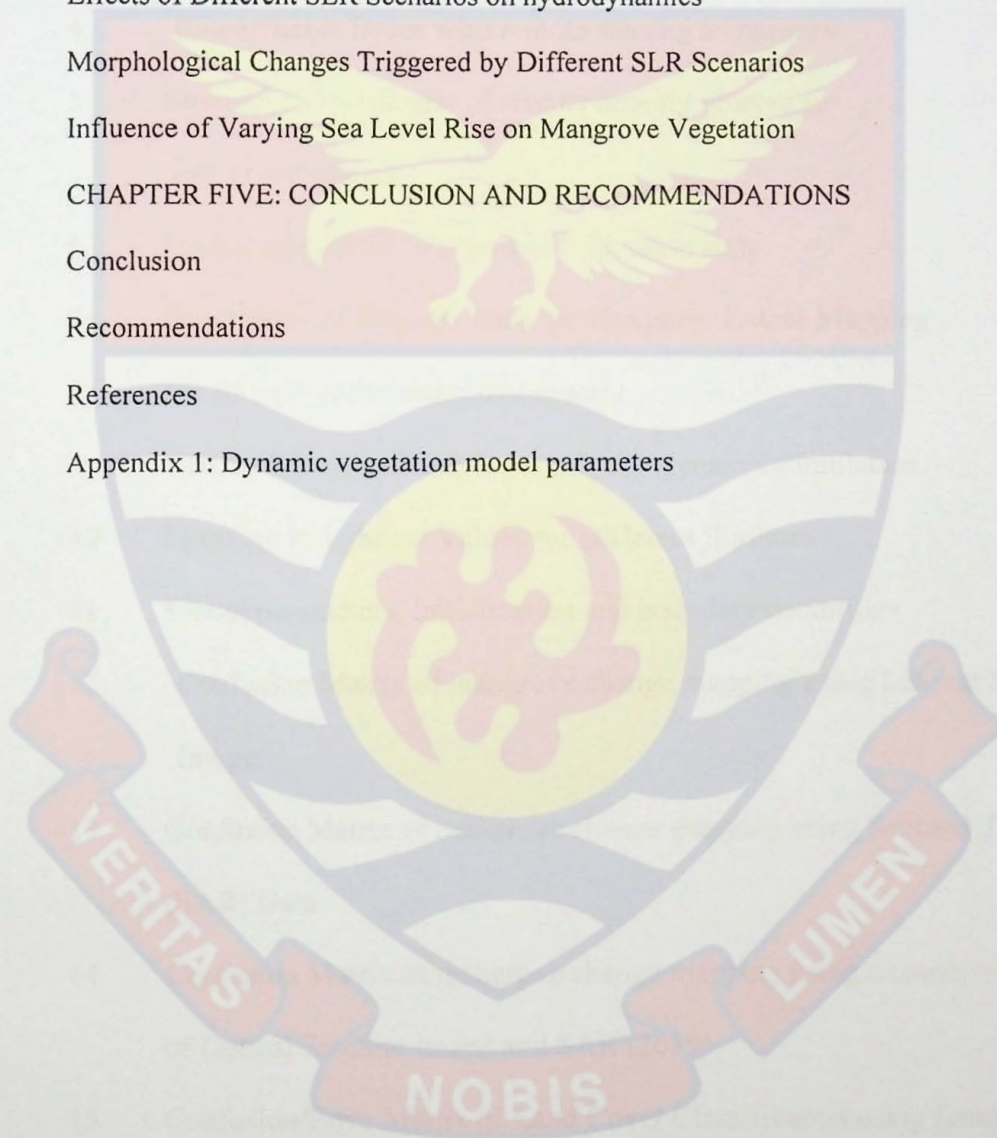
DEDICATION

To my lovely Family

TABLE OF CONTENT

LIST OF TABLES

LIST OF FIGURES

xv

LIST OF ABBREVIATION

ALOS	Advanced Land Observation Satellite
ETM+	Enhanced Thematic Mapper
GEE	Google Earth Engine
HH	single polarization of horizontally transmit and horizontally receive
NDVI	Normalized difference vegetation index
OLI	Operational Land Imager
TIRS	Thermal Infrared Sensor
PAL-SAR	Phase array L-Band synthetic aperture radar
SAR	Synthetic aperture radar
SDG	Sustainable development Goal
VV	single polarization of vertically transmit and vertical receive
SLR	Sea Level Rise
SLC	Sea Level Curve
CMS	Coastal modeling system
IPCC	Inter-governmental panel on climate change
NGO	Non-governmental Organization

CHAPTER ONE

INTRODUCTION

Mangroves which serve as a buffer between terrestrial and marine ecosystems, flourish and thrive in coastal regions with mean monthly air temperatures above 20 °C, with very few exceptions (Blasco et al., 2019). Although mangrove forests only make about 1% of total land area, they are thought to be the most carbon-rich ecosystems in the tropics and subtropics.

According to Bunting et al. (2018), mangrove forests in Africa covered about 2,746,500ha in 2010 and support the vulnerable coastal population by offering crucial ecosystem services like natural marine protection, mitigating coastal erosion, improving water quality, and providing alternative livelihoods (Gedan et al., 2011; Kuenzer and Tuan, 2013; Lee et al., 2014; Mondal et al., 2018). Mangroves cover about 7600 ha along the coast of Ghana and seven major mangrove species, including *Laguncularia racemose* (white mangrove), *Avicennia germinans* (black mangrove), *Rhizophora harrisonii* (red mangrove), *Rhizophora racemose* (Red mangrove), *Rhizophora mangle* (Red mangrove), *Acrostichum aureum* (Golden leatherback), and *Cornocarpus erectus* (Terrain mangrove), have been confirmed (Fatoyinbo and Simard 2013, Ellison et al., 2015; Nortey et al., 2016).

These ecosystems offer numerous vital functions, but they have undergone severe degradation and are in danger of disappearing (Alongi, 2012; Breithaupt et al., 2012). According to estimates, the rate of loss over the last two decades has been twice as fast as the rate of loss of terrestrial rainforest during same time (Mayaux, et al., 2005). A further estimate places the loss of

1

mangrove forests at roughly two-thirds during the past century, with an annual loss of 1-8% and a drop in global land area of at least 20–50% (more than 3.6 million ha) as a result (FAO, 2007; Miththapala, 2008; World Mangrove Network, 2012). Mangrove loss has been mostly linked to climate change and deforestation. It is crucial to have a better understanding of our coastal wetlands, but these habitats are challenging to evaluate and/or model because of how greatly their characteristics vary around the world (Meselhe et al., 2017).

Climate change is already having an impact, and it is anticipated that these consequences will grow in breadth and amplitude over time. According to reports, human activity is thought to be responsible for at least 50% of the observed global temperature increases since 1951, primarily through the emission of greenhouse gases from the production of oil and gas (Clarke et al., 2007). Coastal managers have sought to better inform the public about the negative effects that climate change will have on human and natural communities, as well as what may be done to lessen or prepare for such effects. Traditional research fields are constrained by their single-domain, single-boundary focus, which results in a restricted understanding of coastal ecosystems. Therefore, integrated modeling strategies are required to link the engineering, geomorphology, and ecology fields. Such multidisciplinary modeling methods would enhance comprehension of long-term landscape changes brought on by either human activity or extreme weather events (Meselhe et al., 2017).

The underlying mechanisms in coastal wetlands are examined in this work using a geographic information system and a dynamic modelling methodology. Through the use of the Google Earth Engine (GEE) platform, this study introduced a unique method that combines optical and radar images for more accurate mapping of mangroves and calculating their above-ground biomass density in order to precisely evaluate the effects of anthropogenic pressure on the temporal changes of mangrove. The response of mangroves to tidal current caused by sea-level rise as a climate change driver was simulated using the dynamic modeling methodology.

Study Background

Understanding coastal and marine processes is essential to quantify changes to the mangrove ecosystem. To track changes in mangrove forests, space-based technologies like remote sensing has the capability to collect data from previously unreachable areas (Son et al., 2015). For a more precise measurement of mangrove extent, several authors advise fusing optical satellite data and synthetic aperture radar (Attarchi and Gloaguen, 2014; Ayman et al., 2017; Hu et al., 2020).

A number of studies have been conducted on the extent of mangroves across Africa, including those by Kovacs et al. (2010), Salami et al. (2010), Omo-Irabor et al. (2011), De Santiago et al. (2013), Fatoyinbo and Simard (2013), Kuenzer et al. (2014), Hoppe-Speer et al. (2015) and Brown et al. (2016). Although many of the studies are global in scope, they lack the geographical explicit resolution necessary to follow locally the Sustainable Development

3

Goals (SDGs) that have been adopted by the African Union and the United Nations.

For natural capital and carbon accounting, structural factors like tree height and aboveground biomass (AGB) of forests are important considerations. They also provide soft defense for flood protection and play important roles in mitigating climate change by regulating the carbon balance on a global scale (Houghton, 2005). Deforestation has been identified as a significant source of greenhouse gas emissions worldwide and as a danger to the ecological services that mangrove forests supply (IPCC, 2007). Evaluation of plans intending to lessen the effects of climate change using natural solutions requires accurate quantification and monitoring of temporal and spatial changes in mangrove cover and biomass (Omar et al., 2014).

It has been underlined how crucial remote sensing is in this context as one of the main sources of spatial information (Fatoyinbo and Simard 2013, Lagomasino et al 2016). Given the complexity of the tropical mangrove forest ecosystem, remote sensing methods are not without their limits when assessing mangrove height and above-ground biomass. When it comes to obtaining structural information with accurate estimates at different scales, both active and passive remote sensing systems have their advantages and disadvantages (Son et al., 2015). In the tropics, cloud cover, the intricacy of the mangrove forest ecosystem, and saturation at specific biomass levels make it difficult to use only optical satellite technology for mangrove monitoring and assessment (Steininger, 2000; Omar et al., 2014).

4

Conventional mapping methods have been employed successfully by many researchers to offer data on forest structure, but these methods are constrained by the availability of images, the requisite computational power, and the required technical know-how (Gorelick et al., 2017; Yancho et al., 2020). In particular for mangrove mapping and monitoring, new techniques and technology are ushering in a new era (Wulder et al., 2018; Wang et al., 2019; Yancho et al., 2020). Cloud computing such as Google Earth Engine (GEE) platforms provide unprecedented access to a large collection of ready-to-use geospatial data and computing tools for quick and seamless processing (Gorelick et al., 2017; Yancho et al., 2020).

In more recent years, scientists have studied the dynamics of sea level rise (such as the nonlinear response of hydrodynamics to sea level rise), but there hasn't been much work done in Ghana or elsewhere in Africa to address the combined feedback processes and the evolution of many interrelated systems, such as the nonlinear response and the influence of hydrodynamics, morphology, and ecology under sea level rise. Changes in hydrological systems have a significant impact on coastal wetlands as a result of global climate change (Qiusheng, 2018). To better manage and maintain Ghana's wetland resources, it is therefore necessary to examine these dynamic changes. At the study site, there has been little research on mangrove productivity in terms of biomass density (Aheto et al., 2011; Nortey et al., 2016). However, none of the researchers took into account the long-term development paths of future mangrove behavior in terms of their productivity and some significant

5

long-term feedback processes (such as the relationships between hydroperiod and mangrove mortality in response to climate change).

Statement of the Problem

Coastal zones are subject to increasing economic activities driven primarily by mining activities and oil exploration and exploitation, including but not limited to port operations. These activities have given rise to other activities that have reportedly resulted in accelerated coastal erosion, coastal flooding and increased acidity, depletion of coastal resources (e.g., mangrove wetlands), and general pollution of coastal waters.

Although wetland protection has been prioritized by 159 nations through the Ramsar Convention since inception, wetlands continue to be threatened by various forms of anthropogenic activity (Ramsar Convention Secretariat, 2013). Due to population growth in coastal zones around the world, pressure on coastal wetland resources for agricultural intensification continues to increase. In addition, the effects of global climate variability on coastal wetlands through variations in hydrological systems are also pronounced (Qiusheng, 2018). We need to study these dynamic changes in the coastal zone, particularly in relation to mangrove ecosystem and to better manage and conserve our wetland resources.

Mangroves have been used as a traditional source for many products such as timber, fuel and food. Determining the biomass of mangrove forests is a useful way to estimate the amounts of these components. Accordingly, Aheto et al., (2011) state that the analysis of the existing biomass is one of the accepted

6

approaches of assessing the health of forest ecosystem. According to Friends of the Nation (2014), Anlo Beach wetland complex consists of relatively disturbed mangroves, which this work aims to quantify. The assessment of mangrove ecosystem in tropical coastal zone using only optical satellite data is hampered by cloud cover effects. In literature, most mangrove assessment in Ghana (Nortey et al., 2016; Aheto et al., 2011) have mostly been done using optical satellite imagery. In this study, an approach that combine optical and radar data to reduce the effect of cloud cover and enhance the accuracy of mangrove assessment was proposed.

It has been stated in literature that the impact of climate change on coastal wetlands through changes in hydrological systems are significant and can have far-reaching effects on these important ecosystems (Qiusheng, 2018). However, information on these impacts vis-à-vis the response of mangrove is limited in Ghana. In this study, a process-based model was used to simulate the impact of climate change such as sea level rise (SLR) on mangrove ecosystem.

Objective

The overall objective is to study the underlying processes causing changes in coastal wetlands through GIS and dynamic modeling, particularly in relation to the response of mangroves to anthropogenic activities and projected sea level rise scenarios.

Specific Objectives

The specific objectives are to:

1. map the spatial and temporal changes of mangrove and surrounding ecosystem between 2009 and 2019

2. investigate the effect of using passive or active remote sensing data on the accuracy of the modeling outputs.

3. assess the impacts of land modifications and Sea level rise on Mangrove productivity in terms of biomass density.

4. assess the dynamics of the wetland Morphology under varying sea level conditions.

Research hypotheses

Four hypotheses were tested in order to fulfill the above-mentioned specific objectives:

(1) There is no significant spatial modifications in the Land Cover of the study location over two time periods (2009 and 2019) in the study area.

(2) The type of satellite remote sensing (e.g., active or passive) has no effect on the accuracy of the model outputs

(3) There is no relationship between tidal hydrodynamics and Mangrove productivity and future forecasting is not possible.

(4) There is no possibility of understanding some feedback processes in the Mangrove wetland (e.g., the relationship between elevation and accretion) at longer-time scale in response to climate change.

Statistical Hypothesis

H_{o1} There is no significant Modifications in the Land Cover of the study location

8

H_{A1} There is significant Modifications in the Land Cover of the study location

H_{o2} Satellite remote sensing type has no effect on mangrove mapping accuracy

H_{A2} Mangrove mapping accuracy depends on satellite remote sensing type

H_{o3} There is no relationship between tidal hydrodynamics and Mangrove productivity

H_{A3} There is relationship between tidal hydrodynamics and Mangrove productivity

H_{o4} There is no possibility of understanding some feedback processes in the Mangrove wetland

H_{A4} It is possible to understand some feedback processes in Mangrove wetland

Justification

The world's coastal wetlands habitats and resources have come under tremendous pressure in recent decades. Human development and resource exploitation, coastal population growing at three times the global average, rising sea levels, changing climate and fluctuations in sediment transport due to river damming, coastal erosion control, etc.; all create unprecedented challenges. To address these challenges, the dynamics of coastal wetland zones must be better understood. However, information about this zone and its dynamics is difficult to obtain regularly and over large areas due to inaccessibility by land and sea.

Coastal environment managers need information and data on the possible effects of sea level rise in order to be alert and prepared for uncertainties under

9

future sea levels and to make accurate decisions for the management of human and natural communities. Mapping mangrove extent and change over time as well as modelling the imminent effects of sea level rise can help coastal managers focus on conservation practices.

CHAPTER TWO

REVIEW OF LITERATURE

The Importance of Coastal Wetlands Vegetation

Mangroves, seagrasses and salt marsh are some of the highly important vegetation along the coast which are responsible for the provision of a range of ecosystem services. Several scholars have demonstrated that these vegetations are highly efficient carbon sinks (Laffoley & Grimsditch, 2009; Duarte et al., 2010; Kennedy et al., 2010; Mcleod et al., 2011). Even with their comparatively small global coverage, coastal vegetation like mangroves, seagrasses and salt marsh sequester more carbon dioxide than their terrestrial counterparts, in addition to organic carbon, due to their productivity and efficiency in trapping sediments (Mcleod et al., 2011).

Coastal wetland vegetation provides vital breading space for various species of fish, shellfish as well as other animals and delivers sufficient food/nutrient availability to support vital natural community changes. Small wet-dry tropical estuaries provide the necessary foraging, spawning and nursery environments for benthic and pelagic organisms that are of recreational and/or commercial value (Sheaves et al., 2010). Coastal wetland vegetation represents a transition between marine and terrestrial environments and thus hosts a diverse set of fauna and flora (Ellison, 2009). Many organisms from the marine environment also migrate to coastal wetland vegetation to breed, particularly because the vegetation provides a haven from predators and strong wave action (Asbridge, 2018). Coastal wetland vegetation such as mangroves support some

11

endangered species such as proboscis monkeys, scarlet ibis and straight-billed ranger (Valiela et al., 2001).

Wetland vegetation also provides protection from coastal flooding by stabilizing sediments, which in turn dampen turbulence and currents, recycle nutrients, filter and enhance water quality (Hughes et al., 2009). Mangroves in particular provide coastal protection by mitigating flooding and storm events, including those associated with strong winds and waves in coastal areas, in part due to their high density, buttress root systems and often taller vegetation creating a complex vegetation structure (Asbridge, 2018). Several studies have reported that mangroves dampen violent storm surges, reducing their wave height by up to 20% above 100m. (Mazda et al., 1997; Chang et al., 2006; Alongi, 2008). They do this with the large networks of buttresses and pneumatophores that bind the sediment and cause reduced erosion as they impede water flow and slow wave speeds (Wolanski, 2007, Barbier et al., 2011).

Coastal wetland vegetation is often cited as hyperaccumulating systems due to their natural ability to purify contaminated water (Chiu et al., 2004). Coastal vegetation sediments can efficiently bind heavy metals, which are immobilized as sulfides in the absence of oxygen, with high organic matter composition and low pH (Peters et al., 1997). This suggests the potential of wetland vegetation for phytoremediation, which can be used for industrial wastewater treatment (Chen et al., 2009) to provide a low-cost and low-maintenance approach to wastewater treatment (Conley et al., 1991) and also

12

to remove most heavy metals and prevent them from reaching offshore ecosystems such as coral reefs (Wolanski, 2007).

Coastal wetland vegetation provides various economic and commercial values, for example by providing coastal protection, mangroves limit damage to businesses, property, agriculture and fisheries, and by sequestering carbon, mangroves can potentially bring blue carbon income to local residents and governments (Asbridge, 2018). Coastal communities have traditionally used wetland vegetation for a number of purposes, including local timber collection for building homes, boats, fishing poles and charcoal/firewood. Some mangrove leaves are traditionally used as food (e.g., fresh leaves of *Avicennia alba*) for humans and to feed animals, while others have medicinal values (e.g., the bark of *Rhizophora mucronata* has been used to treat diabetes) (Bandaranayake, 1998, Rahmatullah et al., 2010). Tannins and sap extracted from the bark of certain mangrove species can be used to improve the durability of fishing nets (Prasad, 2011) and to make medicines, sugar, insecticides and pesticides (Bandaranayake, 1998). Secondary products from these vegetations, including but not limited to fish, honey, wax and shellfish, also have commercial value and market demand.

Mangrove Ecosystem

Mangroves grow and thrive in a setting that acts as a buffer for both terrestrial and marine organism. Mangrove is a universally important ecosystem found in the intertidal tropical and subtropical zones as shown in the Figure 1. These ecosystems are mostly trees and shrubs found in flat areas of sand or mud adapted to estuarine or saline environments. They are really exceptional

13

because they can tolerate huge amounts of brackish water. Its ability to survive in oxygen-poor soils is because of the root adaptation. These ecosystems are of course beneficial to the survival of millions of people across the world. High on the list of these natural benefits, alongside carbon sequestration are the defense of seashore and man-made structure from severe storm, the raising of fish, and the making of charcoal. Mangroves cover less than 1% of the global land but are regarded to be the highest carbon-rich environments in the tropics and subtropics. Mangrove forest was included in the IPCC Strategic Plan for Climate Action through a series of wetland amendments (Lucas et al., 2014).
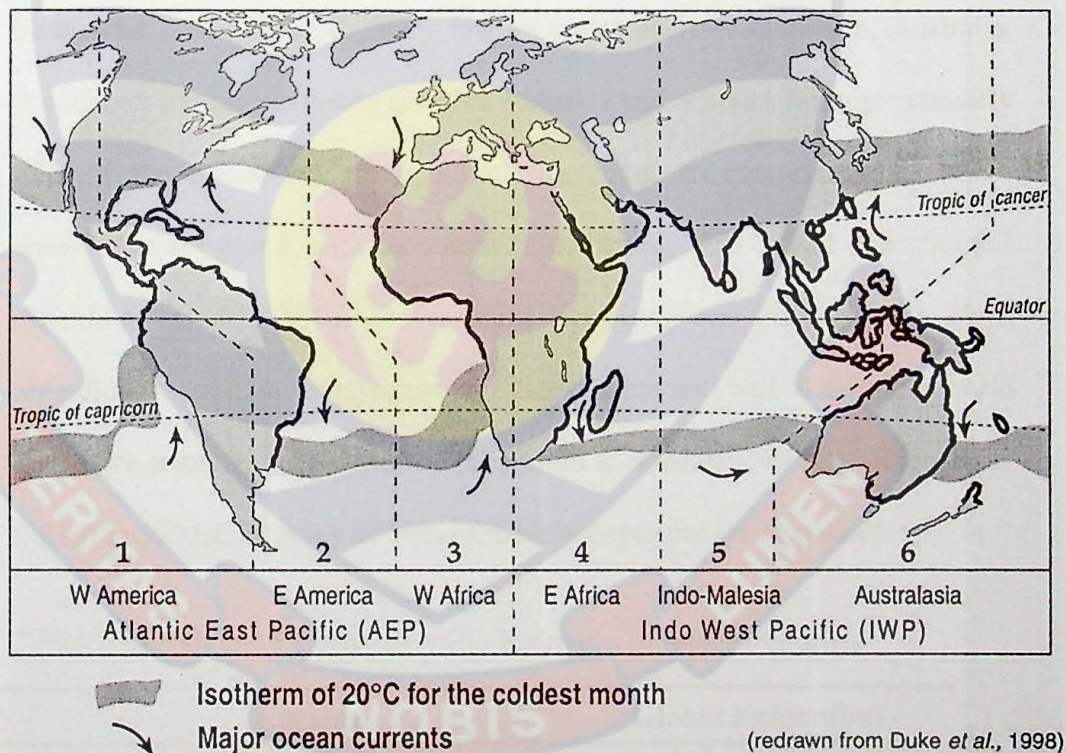
Figure 26: Global Mangrove Distribution (Cited in Blasco et al., 2019)

Mangrove forests survive mainly in coastal areas where the average temperature is above 20 °C and where, with rare exceptions, ground ice formation does not exist (Blasco et al., 2019). The distribution of mangroves is

14

dominant in six geographic zones of the world (Figure 1) (Chapman, 1976; Snedaker, 1982; Rao, 1987; Saenger & Bellan, 1995; Duke et al., 1998; Blasco et al., 2019). The predominant species of mangroves in these geographic zones are shown in Table 2. Dense mangrove forests with very tall mangroves (up to 60 m tall) are predominant in bioclimatic settings (Blasco et al., 2019; Simard et al., 2019). Mangroves can grow in arid regions in the form of short mono-specific stocks (Dodd et al., 1999). The Ganges Delta in Bengal hosts a substantial area of mangroves (> 600,000 ha) (Blasco et al., 2019). A study by Spalding et al., (1997) states that the entire global mangrove coverage is about 18,000,000 ha and most of it is found in South Asia and South-east Asia (Table 1). Very few countries such as Indonesia, Australia, Brazil and Nigeria dominate the area statistics and account for approximately 43% of the global mangrove out of the 70 or so countries where these ecosystems are found, with Indonesia alone having 23% and 12 countries 2/3 (Spalding et al., 1997). Government decisions and management plans regarding mangrove ecosystems in these countries will determine world mangrove status in the near future (Hamilton & Snedaker, 1984). Blasco et al., (2019) argue that as many as 30% of these ecosystems are degraded.

Table 2: Global and Country Specific Estimates of mangrove areas

Regions	Global Extent (ha)
South and Southeast Asia	7517300 (41.5%)
Australasia	1878900 (10.4%)
America	4909600 (27.1%)
West Africa	2799500 (15.5%)
East Africa and Middle East	1002400 (5.5%)
Total area	18107700

Main countries	Spatial Coverage (ha)
Indonesia	4250000
Australia	1150000
Brazil	1380000
Nigeria	1050000
Malaysia	640000
India	670000
Bangladesh	630000
Cuba	550000
Mexico	530000
Papua New Guinea	410000
Colombia	360000
Guinea	290000
Total	11910000

Source: Spalding et al. 1997, cited in Balsco et al., 2019

Mangroves cover around 0.7% of tropical and subtropical forest areas worldwide in over 118 nations (Bunting et al., 2018; Siikamaki et al., 2012; Donato et al., 2011; Page et al., 2011). Murdiyarso et al. (2015) argues that mangrove can sequester and store 3 to 4 times more carbon for each equivalent area of tropical forest. In particular, mangroves found in dominant peatlands are expected to store 25-50% higher organic carbon in the soil (Rovai et al., 2018) and host about 1.6% of entire biomass in tropical forest (Hutchison et al., 2014). For Africa, mangroves cover approximately 2,746,500 ha in the year 2010 and maintain vulnerable coastal populations by delivering vital ecosystem services, including storm surge mitigation, coastal erosion mitigation, water quality improvement and the provision of alternative

16

livelihoods ((Bunting et al., 2018; Mondal et al., 2018; Lee et al., 2014; Kuenzer & Tuan, 2013; Gedan et al., 2011).

Basically, studies evaluating and monitoring mangroves in Africa are unequally distributed (Pinki et al., 2019). There are several studies on the extent or dynamics of mangroves across Africa (Lagomasino et al., 2019; Brown et al., 2016; Hoppe-Speer et al., 2015; Kuenzer et al., 2014; De Santiago et al., 2013; Fatoyinbo & Simard, 2013; Omo-Irabor et al., 2011; Kovacs et al., 2010; Salami et al., 2010), but many of them are largely concentrated in a few countries. However, a large number of such research are global in nature, but lack a suitable spatial resolution for tracking local progress towards the achievement of Sustainable Development Goals. Mangrove ecosystem can help to achieve a number of SDGs, most notably Goal 6 and Goal 15 because they serve as important indicators for monitoring local, regional and global progress. Mapping mangrove extent both locally and globally is critical to understanding progress towards achieving these goals (Barenblitt & Fatoyinbo, 2020a).

There are different types of mangroves, mainly red, black and white (Figure 2). A report by Fatoyinbo and Simard (2013) shows that mangroves cover about 7,600 ha along the Ghana coast, seven major mangrove species are known in Ghana. These species are white mangrove, black mangrove, and red mangrove (Ellison et al., 2015; Nortey et al., 2016). Red mangroves are the most salt tolerant, white the least. Mangroves are generally short trees, but some can reach 60 m in height and can reach high levels of above-ground

17

biomass. In addition to structural differences, some may have large curved roots while others do not.
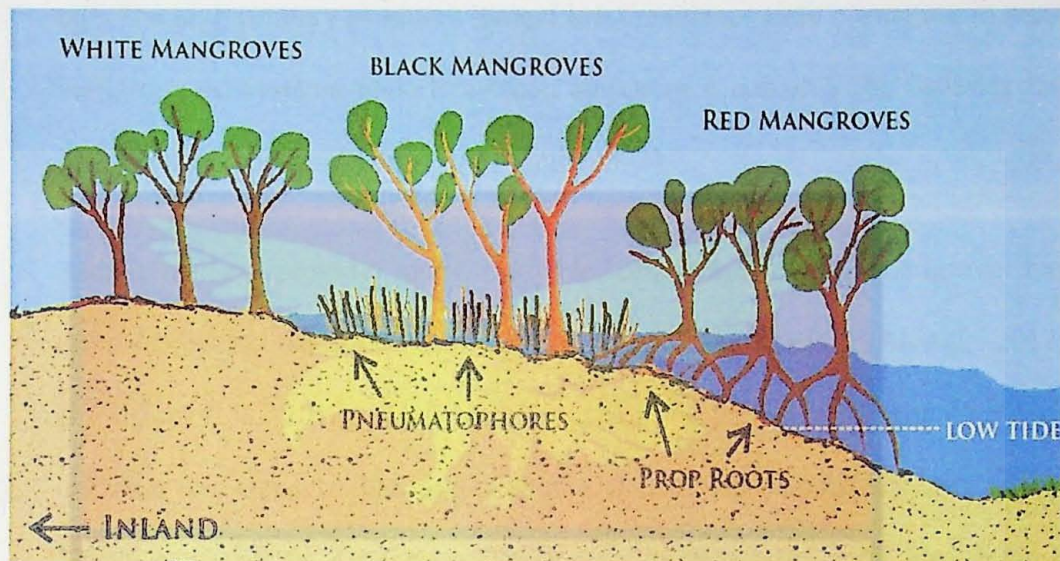
Figure 27: Different types of mangroves based on their Salt Tolerance
 Source: wetlandsandwildlife.wordpress.com

Mangrove Dynamics, Structure and Function

Extensive research has been carried out to improve our understanding of the structure and complexity of mangroves (Lugo et al., 1980; Twilley, 1982; Sassekumar & Loi, 1983; Adaime 1985; Duke, 1988; Lahmann, 1988; Woodroffe et al., 1988; Saenger & Snedaker, 1993; Fromard et al., 1998). Mangrove height ranges from 12 m to 20 m and rarely exceeds 25 m, litter falls from 12 - 16 t/ha/yr (dry matter) in the equatorial and sub-equatorial regions. Near the tropics, their mean height is about 8 to 12 m and the average annual litterfall is estimated at 8 t/ha. Within the temperate coastal zone, a place where mangroves are exceptional, mangrove height rarely exceeds 4 m and litter-falls decline to 4 t/ha/yr. (Blasco et al., 2019). Simard et al. (2019) emphasized that precipitation intensity, temperature variation and frequency of extreme events (e.g., cyclone) explain 74% of global dynamics in maximum

18

mangrove height, biomass density and litter drop, however they found the tallest mangrove canopy in Equatorial Africa where stocks are up to 62.8 m tall. The high primary productivity and brief residence time of manure in most mangrove ecosystems underlines their importance not only for fisheries but also for other species (Snedaker & Lugo, 1973).

Although they provide many valuable ecosystem goods, mangrove has experienced significant anthropogenic related degradation (Alongi, 2012; Breithaupt et al., 2012). It has been estimated that the rate of degradation over the past two decades has overwhelmed that of rainforest (Mayaux, et al., 2005). Most of the ecosystems (2/3) have disappeared in the last century, resulting in a loss of 1-8% mangroves per year and no less than 20-50% reduction in global land area (FAO, 2007; Miththapala, 2008; World Mangrove Network, 2012). The main reason for mangrove loss is deforestation for land conversion, principally for aquaculture development, establishment of salt pans, and other agricultural expansion. The rapid loss of mangroves to deforestation can contribute significantly to the total carbon emissions (Donato et al., 2011).

However, recent research suggests that the rate of global mangrove loss may now be reduced as the top threat from deforestation is declining from an initial estimate of 0.7% between 2000 and 2005 to around 0.16% to 0.39% per year in 2016 (Spalding et al., 2010; Hamilton & Casey, 2016). Therefore, most observed changes in the mangrove ecosystem can be attributed to climate variability which leads to temperature, precipitation and air pressure fluctuations. (Asbridge et al., 2015). Some of the challenges in mapping

mangrove ecosystems are the need for high-resolution imagery, as these ecosystems tend to cover a narrow band along the coast. Therefore, given the nature of mangrove areas that are more prone to cloud cover, it can sometimes be difficult to find cloud-free optical imagery over these areas. Additionally, the state of these ecosystems is dynamic due to ebb and flow differences, which can affect satellite signal.

Coastal Wetlands Vegetation Conservation

One of the first global efforts towards prudent use of wetlands by indigenous peoples, national and international action, is the 1971 Ramsar Convention with a commitment to help achieve sustainable development around the world. Mangroves have been designated according to the Ramsar Convention as a forested tidal wetland with 262 locations worldwide and an area of 27,000,000 ha (Ramsar, 2012; Lucas et al., 2014). National wetland inventories have been among the top priorities of Ramsar Convention signatories with the sole aim of ensuring judicious use of wetlands in different regions (Lucas et al., 2014). However, the challenges of the convention were the procedures used and data management, leading to the 2005 Ramsar resolution (MEA, 2005; Ramsar, 2005; Rosenqvist et al., 2007b; Lucas et al., 2014).

Recognizing the need for more accurate information on global mangroves, a number of initiatives have been implemented by several international organizations over the past four decades to improve our knowledge of mangrove forest conversion or loss for reference years. Major international initiatives include: (1) the conservation of migratory species of wild animals (CMS, 1979); (2) Convention on biological diversity (CBD, 1993); (3) the

20

United Nations Framework Convention on Climate Change (UNFCCC, 1992); (4) the Intergovernmental Science Policy Platform on Biodiversity and Ecosystem Services (IPBES, 2012). These efforts aim to provide better and improved data on habitat conversion and future trajectories (Lucas et al., 2014).

Accurately quantifying the extent of mangroves, through mapping is one of the key tools needed to support the Ramsar Protocols and any intergovernmental initiative aimed at enabling signatories to achieve the goal of the initiative. Maps like the JAXA Carbon Initiative Global Wetland Inventory, can also give information on the extent of disturbance due to flooding within the defined wetland areas. In addition, information on the impact of policy measures is required to assess their effectiveness in terms of prudent use of wetlands. This information is necessary to encourage sustainable development and policy adaptation and to ensure adequate representation of wetland types in the Ramsar List (MacKay et al., 2009).

One of the first global mangrove maps was created by combining previous maps, ground surveys and remote sensing data (Spalding et al., 1997). A global atlas of mangroves was updated by UNEP-WCMC and published in the year 2010 (Spalding et al., 2010). Giri et al. (2011) produced another revised baseline for world mangrove distribution based on Landsat data. The distribution baseline map serves as an important tool for mangrove conservation and management, as well as for systematically assessing the performance of the ecosystem goods they offer. On the other hand, a number of recent interventions have attempted to use more specific data on mangrove

21

services. These include, but are not limited to: (1) Mangrove Conservation Alliance (BirdLife International, 2011); (2) Mangrove Capital Program (Wetlands International); (3) International network for the conservation and sustainable use of Mangrove genetic resources.

The need for a coordinated effort to address issues related to the effect of climate variability on coastal ecosystems necessitated the creation of the blue carbon initiative by the United Nations Environment Program (UNEP). The program objectives are to promote research and develop strategies and programs for the conservation as well as the restoration of coastal ecosystems. These policies and programs include globally applicable measurement standards to support financial platforms (e.g., National Measurement, Reporting and Verification (MRV) Systems). Despite these interventions, timely and more accurate information on mangrove dynamic trends at the local, regional, and global scales has not been routinely and consistently provided. Closer look at the social and economic value of mangroves is also needed to guarantee that the ecosystems are not underestimated in decisions making regarding their use. Consistency in the use of spatial and temporal methods is crucial to guarantee adequate and more consistent estimations of extent within and between regions.

Conservation Efforts in Africa

There is ample evidence of the successful establishment of Mangrove plantations in West Africa and Central Africa involving governments, NGOs and local communities. For example, since 1993 there have been fragmented mangrove planting efforts in some parts of Africa, notably Senegal, Guinea

and Ghana (Gordon et al., 2015). By 2014, more than 450 ha of Mangrove plantation had been established in Central Africa and more than 60 ha of mangrove plantations had been created in West Africa (Armah et al., 2009). The plantations were established in these countries with the efforts of projects led by the state ministries responsible for mangroves, local communities and NGOs. Universities and parliamentarians have stepped up efforts of NGOs in Cameroon. In general, plantation establishment in West Africa (61.8%) was more strongly encouraged by government efforts, while in Central Africa, NGO efforts (51.9%) were more pronounced. Donor organizations include: European Union, PNUD, FIDA, GEF, FFEM, NC IUCN, SSNC, GTZ, AFD and PAFT.

Mangrove restoration activities in Ghana were integrated into some coastal projects between 1995 and 2000 (Armah et al., 2009). Examples of such initiatives are the Large marine ecosystem project in the Gulf of Guinea; The Lower-Volta mangrove project supported by the United Kingdom and a community campaign in Ghana involving two communities with additional help from an NGO (Resource & environment development organization (REDO)) and the Department of forestry in Winneba where over 6,000 reproductive plants have been planted; Obane mangrove restoration project in Ada with over 2000 seedlings of *Rhizophora sp.* and *Avicennia germinans* planted by people through community work (AMN, 2009).

Advances in Satellite Data Applications for Wetland Studies

Advances in systematic monitoring to understand changes in wetlands are needed to regulate how mangrove ecosystems are continuously changing due

23

to human-made impacts or natural drivers, or both (Pimple et al., 2018). Accurate quantification of temporal changes in mangrove ecosystem is essential for better understanding of many marine processes. Mapping of mangrove forests requires enormous amount of money for fieldwork because of the difficulties related to access within the mangrove ecosystem (Zhang et al., 2014). Space based technologies like remote sensing have tremendous capability to map changes in mangrove forests by capturing data from an otherwise inaccessible landscape (Son et al., 2015). Two main types of remote sensing data exist namely; passive remote sensing and active remote sensing. Active remote sensing provides data in the form of images (e.g., SAR) and in the form of altimeter, while passive remote sensing provides optical imagery (e.g., Landsat).

SAR and LiDAR Data Applications

SAR data is useful for assessing and mapping mangrove extent, even in the tropics where cloud effects are predominant (Vermeulen et al., 2005; Horritt, 2006; Mason et al., 2007; Schumann et al., 2007; Di Baldassarre et al., 2009; Long et al., 2014), due to the properties of the sensor backscatter mechanism and signal penetration for different targets (Musa et al., 2015). Because of its high penetrating power, SAR is suitable for land cover research as well as land use monitoring (Owe, et al., 2001). Table 3 and 4 show the interaction between Mangroves and Radar Signal at Different bands as well as the corresponding backscatter range. The higher the backscatter, the rougher the surface. For example, the reflectivity of SAR for an undisturbed body of water gives very little backscatter and very dark images. However, when the water

24

body is disturbed by wind, turbulence or surrounding vegetation, backscatter increases and produces a bright or gray image (Erika et al., 2020).

Several GIS and geospatial techniques have been applied for mangrove assessment (Long et al., 2014; Musa et al., 2015; Pinki et al., 2019). Most studies often use data from passive satellite such as Landsat due to their larger spatio-temporal coverage as well as easy data accessibility (Brown et al., 2016; Wang et al., 2019; Pinki et al., 2019). The recent availability of active satellite data with increasing spatio-temporal coverage has led many scientists to increasingly use data from SAR for a more accurate mapping of the mangrove changes (De Santiago et al., 2013; Thomas et al., 2018; Pinki et al., 2019).

Cloud cover conditions does not affect Radar imagery (SAR) and it has therefore been used to map mangrove changes over time (Thomas et al., 2017). The global availability of cloud free radar imagery since 1996 to the present has enabled few researchers to monitor mangrove extent worldwide (Thomas et al., 2018). For the assessment of mangrove changes, scientists use different classification systems and algorithm (Fatoyinbo et al., 2013; Giri et al., 2015; Kamal et al., 2015; Pinki et al., 2019). The novel cloud computing platform like Google Earth Engine (GEE) with unrestricted access to global mosaics of geospatial data are now increasingly accessible and provide straightforward analysis for large satellite imagery (Chen et al., 2017; Pinki et al., 2019). Google Earth Engine provides over 15 classification techniques using artificial intelligence, such as CART and RF for robust land cover classifications (Giri et al., 2015; Diniz et al., 2019; Shrestha et al., 2019).

25

Cloud computing procedure based on robust algorithms is very helpful for systematic monitoring and continuous assessment (Pinki et al., 2019).

European space agency (ESA) satellite-1 and - 2, which was launched from 1991 to 2011, ENVISAT advanced synthetic aperture radar which was commissioned from 2002 to 2012, and Canadian space agency (CSA) RADARSAT 1 (1995 to 2013) and RADARSAT-2 (2007 to present) are among the high-capacity space-borne SAR to monitor mangroves on a global scale, with C-band historical archives (Lucas et al., 2014). In addition, German space agency (DLR) successfully completed TandemX mission in 2010, comprising Terra-SAR-X and COSMO-SkyMed, forming a cluster of 4 sensors to provide X-band SAR imagery. However, the disadvantage of X- and C-band images captured by previous sensors is that systematic global coverage has not occurred over time and there are also issues of cost and complexity (Lucas et al., 2014). The TanDEM-X mission is very useful for mangrove monitoring, as the sensor-derived global digital elevation provides useful information on mangrove canopy elevation and above-ground biomass throughout its range (Lucas et al., 2014).

Changes in mangrove structure as a function of elevation changes can be estimated by comparing tree height estimates from the TanDEM-X with estimates from SRTM (Lucas et al., 2014). The major L-band sensors on a global scale are the Japanese earth resources satellite (JERS-1) and the advanced land observing satellite (ALOS) phased array L-band (PALSAR) which were used from 1992 - 1998 and onwards 2006 - 2011 respectively (Shimada & Ohtaki, 2010; Shimada et al., 2010; Lucas et al., 2014). These

two sensors represented efficient acquisition approaches that have yielded consistent pantropical and global L-band mosaics annually (Rosenqvist et al., 2000, 2007a; Lucas et al., 2014).

PALSAR-2 was launched in 2014 as a continuation of the mission to monitor the nearshore tropics and subtropics, specifically mangrove monitoring with reliable, efficient and cloud-free data around the world with better sensitivity to 3D wood structure of mangroves, allowing the retrieval of above-ground biomass (AGB) density (Lucas et al., 2007; Lucas et al., 2014). Part of JAXA's Carbon initiative was used to develop the Global Mangrove Watch (Lucas et al., 2007; Rosenqvist et al., 2010; GMW (JAXA), 2013; Lucas et al., 2014). Historical JERS-1 and PALSAR images alongside the Global Mangrove Watch were used by Giri et al. (2011) to improve Landsat-based mangrove base-maps for several years (e.g., 1996, 2007, 2008, 2009 and 2010) and changes detected by ALOS-2 PALSAR-2 were quantified. Baseline measurements of structure and aboveground biomass generated from SRTM, ICESAT and GLAS have been widely used for mangrove monitoring by a number of authors (Simard et al., 2006, 2008; Fatoyinbo & Simard, 2013; Lucas et al., 2014). The PALSAR image (L-band) can be used to differentiate huge (> 10 m) mangroves with buttress from those without as they have relatively low HH backscatter for the L-band (Lucas et al., 2007). Therefore, the combination of active and passive satellite data allows for the quantification of changes in both volume and structure, including tree species losses and gains (Lucas et al., 2014).

Radar remote sensing works in interferometrically when the data is acquired from multiple single acquisition of the same target from different sensor positions. Interferogram refers to the change in signature of topography, noise/speckle, displacement, cloud effects, and baseline error between two SAR images. The importance of phase differences in interferometric data such as InSAR allows detection of land cover change (Lucas et al., 2014). Dellepiane et al. (2004) used this feature to identify flooded areas over wetlands. Their method was based on the concept of fuzzy connectivity, which can spontaneously select shorelines from two different InSAR images due to consistency in the images. InSAR images calibrated with satellite altimetry data have been applied successfully to estimate sea level changes (Kim et al., 2009; Jung et al., 2010). Non-flooded areas, flooded vegetation and water bodies were distinguished based on backscatter and interferometric consistency (Musa et al., 2015). Interferometric data were used to categorize forest age (Pinto et al., 2012) and to estimate tree crown height (Simard et al., 2006, Simard et al., 2008, Fatoyinbo et al., 2013, Lagomasino et al., 2015, Lee et al., 2015, Simard et al., 2019).

Table 2: Radar Signal Interaction with Mangroves at Different bands

Type of Band	Depth of Penetration	Backscatter Type
K	Few tens of centimeters	Straight bounce
X	Up to 1/3 of canopy height (Lorey's height)	Straight bounce, volume scatter for small canopy size and double bounce that increases at low biomass
C	higher penetration and coherence	Straight bounce, volume scatter for small canopy size and double bounce that increases at low biomass
L	Very high penetration	Dominant direct bounce in tall forest. Volume scattering dominate in shorter forest. Double bounce increases at low biomass and in open forests.
P	Similar to L-band with high Microwave penetration into Canopy	Dominant direct bounce in tall forest. Volume scattering dominate in shorter forest. Double bounce increases at low biomass and in open forests slightly higher than L-band

Source: SERVIR SAR Handbook Chapter 6 by Marc Simard

LiDAR is another method with the ability to precisely capture the 3D aspect of mangroves and can therefore be applied to assess the biomass of forests with better reliability (Tianyu et al., 2020). LiDAR is one of the active satellites that effectively penetrates dense tree canopies and can be used to collect data about their structure (Lim et al., 2003; Tianyu et al., 2020). This technique is a key breakthrough in forest monitoring, as it is able to calculate canopy height, forest above-ground biomass including other structural parameters, and is non-saturating even under high-biomass bioclimatic conditions (Nsset et al., 2011;

29

Babcock et al., 2015). Airborne and space-based LiDAR are capable of obtaining large-scale data, but limitations in global coverage limit their application on a continental to global scale (Hu et al., 2016). The ICESAT mission was the only LiDAR instrument to generate global coverage data, which provided a vital source of data for estimating tree height and biomass (Tianyu et al., 2020). However, the mission ended up in orbit within 7 years.

Table 3: Backscatter Range for Mangroves

Radar Band	Shrub Mangrove	Tall Mangrove
P-band (HH polarization)	~ -17dB	~ -8dB (increases with AGB)
P-band (HV polarization)	~ -22dB	~ -14dB (increases with AGB)
P-band (VV polarization)	~ -10dB	~ -7dB (increases with AGB)
L-band (HH polarization)	~ -25dB to -15dB	Decreases from -5dB to -18dB with increase in AGB
L-band (HV polarization)	~ -25dB to -20dB	Decreases from -15dB to -22dB with increase in AGB
L-band (VV polarization)	~ -20Db to -12dB	Decreases from -8dB to -16dB with increase in AGB
C-band (HH polarization)	~ -12Db	~ -7dB
C-band (HV polarization)	-20 to -15Db	~ -14dB
C-band (VV polarization)	~ -12dB	~ -6dB

Apart from mangrove mapping, remote sensing products such as imagery, DEM, altimeter, etc. can be used as numerical model setup and validation (Pereira-Cardenal, et al., 2011). For example, estimates from satellites for river current, channel width, surface roughness, and water levels are used for

calibration and validation. Surface roughness is a very sensitive parameter that directly affects water level and flood extent (Schumann et al., 2007) and can be used to reduce outliers from the calculated water level (Woldemicheal et al., 2010). Satellite-generated flood maps were used to calibrate hydrological models for single and numerous flooding (Di Baldassarre et al., 2009). Satellite images of a particular event, taken almost simultaneously by two satellite sensors, were used by Di Baldassarre et al. (2009) to calibrate a hydrological model based on the 'possible' extent of flooding from the two images, and the result shows that satellite data can be reliable for flood mapping.

Optical satellite data

For several decades, remote sensing data collected via optical satellites for monitoring changes in mangrove extent around the world has been available with various limitations (Lucas et al., 2014). Recent high-resolution passive remote sensing (e.g., Worldview) deliver detailed information for mangrove extent mapping at local level, however global coverage is a serious limitation and the collection of this data is often not repeated (Wang et al., 2004; Proisy et al., 2007; Neukermans et al., 2008; Wang et al., 2008; Lucas et al., 2014). Mangrove assessments at regional level can be done with optical imagery of moderate resolution such as Landsat, SPOT, or ASTER but continuous detection of changes has proven difficult in most regions where cloud cover impedes steady observations from passive satellites (Spalding et al., 1997; Giri et al., 2011; Lucas et al., 2014).

31

Basically, previous worldwide maps of mangrove changes were generated from passive remote sensing data from various sources (Spalding et al., 2010). The mapping was essentially performed using multi-year data as cloud cover affects the information in a single time. Despite the disadvantages associated with optical data, mangrove baseline extent maps generated from them are valuable because such maps are difficult to generate from SAR data alone, irrespective of the fact that cloud cover effects are overcome. In particular, using only L-Band or C-Band SAR data to map the extent of mangroves is insufficient when mangroves are adjacent to other terrestrial forests and plantations, as there are similarities in the nature of their backscatter properties. It is generally easier to distinguish and map mangroves when bounded by sparsely vegetated surfaces, as they exhibit higher backscatter in both the L-Band and C-Band for HV and HH polarizations, although there may be confusion when there is high ground mangrove biomass with broad buttress systems due to the low backscatter associated with such mangrove (Lucas et al., 2007).

Increasingly, advances in satellite are being used to overcome this limitation, such as the use of Landsat sensors to intensify cloud-free observations by pixel mining and the application of synthetic aperture radar systems alone or in combination with optical imagery to enable observations independent of weather or lighting effects (Zhu & Woodcock, 2012; Nascimento et al., 2013). Another way out is to limit mangrove mapping to an area where there is a high presence of mangrove.

Satellite-derived DEM Data Applications (AGB and structure)

Estimates of mangrove stand height, carbon storage, and surface and underground biomass can be produced for a mapped area when the baseline of mangrove extent is already known. This can be derived either from allometric equations or from satellite estimates. (Comley & McGuinness, 2005). Most satellite estimations of above-ground biomass were generated using digital elevation model (SRTM) acquired in 2000 (Giri et al., 2011; Fatoyinbo & Simard, 2013), but using TanDEM-X mission, which was published in 2014 is another useful sensor for monitoring mangrove above-ground biomass, as the sensor-derived global DEM provides data to estimate mangrove height around the world (Lucas et al., 2014). By means of the canopy height estimates from TanDEM-X mission together with those from SRTM (Shuttle radar topographic mission) can show changes in the mangrove ecosystems (Lucas et al., 2014).

The satellite estimates of above-ground biomass can be further improved by integrating synthetic aperture radar imagery such as ALOS PALSAR data into the digital elevation model (Omar et al., 2014). Some studies performed in Australian mangroves show that where many buttress roots occurred, the raise in L-band backscatter with above-ground biomass was discontinued at an altitude of 8-12 m and backscatter decreased proportionally to the increase in above-ground biomass (Held et al., 2003). Exploiting backscatter mechanism in mangroves, a new mapping approach using the canopy elevation model (CHM) and SAR backscatter was developed to distinguish between mangroves with buttress roots and those without (Lucas et al., 2007). This

33

type of information can be applied to estimate the stages of mangrove regrowth and also infer species structure. More information on the researchable issues that remote sensing techniques can be applied are shown in Table 4. The strength and weakness of satellite sensors for mangrove studies are summarized in Table 5.

Table 4: Researchable issues with remote sensing techniques

Needed information	Target Audience	Primary Objective
Extent	Policy, Land holders	To delineate areas of conservation and exploitation
Social-economic and cultural values	Policy	To maintain and increase general well-being
Food security (actual and predicted quantity e.g., fish, game, fruit, grain)	Local population, commercial, government at all levels	Ensuring the continuous supply of food to the population
Fiber and fuel amounts	Local population, Commercial	To determine potential resources and ensure the sustainability of the mangrove habitat
Biochemical and genetic material	Commercial, Policy	Maintain habitat condition and biodiversity
Extent and rate of Mangrove removal	Conservation, policy, science community	Estimate area, trend of area loss, causes and consequences
Habitat structure and	Conservation, Science	Assessment of breeding

floristic composition	community	site status for species
Regeneration and restoration rates	Conservation, commercial, science community	Identify extensions, potential uses and sustainably used areas
Suitable Areas for Mangroves	Conservation, policy	To identify potential restoration areas
Extent and Mangrove zonation	Conservation	Assessing the role and potential of coastal protection
Sea Level Rise Impact	Policy, Science Community	Comprehend the effects of global climate variability
Soil loss and deposition	Land use workers	Indicates where mangrove loss and colonization are occurring
Hydrodynamics and quality of soil	Land use workers, Local authorities	View degraded areas for remediation
Biomass, Volume, Carbon stocks and cycling	Policy, research community, commercial	To measure current resources and quantify current and future carbon sequestration capacity

Table 5: Strength and weakness of remote sensing sensors for mangrove studies

	L-Band SAR			C-Band SAR	X-Band SAR	Optical RS	
	JERS-1	PALSAR	PALSAR-2			Landsat	SPOT/ ASTER
Cloudless images	✓	✓	✓	✓	✓		
Sensitive to vegetation				✓	✓	✓	✓
Sensitive to structural component	✓	✓	✓				
Sensitive to biomass	✓	✓	✓				
Worldwide acquisition	✓	✓	✓	✓	✓	✓	✓
Time series data	✓	✓	✓		✓	✓	✓

Source: Lucas et al., 2014

Gaps and limitations of Satellite Application

Although active and passive remote sensing applications have been useful in mangrove monitoring and assessment, the measurements are not without limitations. Most limitations arise from sensor errors, data processing techniques, seasonal variations and measurement times, target distance, etc. Passive remote sensing is limited to daytime data collection and it is not very useful in cloud-prone areas because the target object can't be reached (Smith, 1997). There are a number of limitations with optical data; For example, the spatial resolution of optical satellite data is often coarse and may not deliver highly detailed resolution suitable to distinguish between vegetation types, the

36

sensor doesn't capture cloudless images and can't enter dense tree canopy. However, these limitations also depend on time, season and hydraulics during data collection (Sun et al., 2010).

The effectiveness of radar data for mangrove research is subject to weather conditions (e.g., wind and rain), angle of incidence, low vegetation and the instrument polarization mode used during data collection (Musa et al., `2015). For example, the HH polarization performs better for mapping mangrove extent compared to VH and VV polarizations. However, the latter are particularly useful for flood monitoring (Schumann et al., 2007). A source of confusion in SAR data is that certain features such as open water and low vegetation, urban areas and flooded areas, topography and flooded vegetation appear similar and present difficulties in data interpretation. Mapping mangrove extent using only radar data is challenging, especially when mangroves border forests.

The limitation of the satellite-supported digital elevation model lies in the data quality. The accuracy of the digital elevation model (DEM) data required for mangrove structural studies and other studies involving topographical considerations is dependent on the collection methods, handling, and surface features. Digital elevation models acquired from passive satellites tend to have high deviation, high RMSE and lower vertical accuracy than those derived from active satellites such as airborne LiDAR or SAR (Fraser & Ravanbakhsh, 2011). However, DEMs derived from optical satellites have wider coverage and are therefore valuable topographic data sources (Gorokhovich & Voustianiouk, 2006).

37

Novel Approach for Mangrove Mapping and Monitoring

Scientists are currently developing pioneering approaches to make satellite data more usable and to overcome current data limitations. For instance, cloud-masking can remove a greater percentage of clouds from optical images, increasing data availability. An example of these novel techniques is the google earth engine (GEE) which is a free cloud based geo-spatial processing platform built from a number of publicly available data. GEE gives access to many satellite imageries from a number of NASA and ESA satellites such as Landsat and Sentinel imagery. It works with a user-versus-server interface where users can work on objects through the server to instruct google for processing and to send the outcome back for display. By default, GEE projection is WGS84 with access to planetary scale data.

Sea Level Rise Effects on Coastal Areas

Currently, coastal areas face the threat of flooding, erosion, saltwater intrusion and other natural disasters as sea levels rise (Williams & Ismail, 2015). Along the Gulf of Guinea, sea level rise data shows more than 3 mm year^{-1} from 1993 to 2010 (ESA, 2012). It is projected that the SLR in Africa will increase by 10% (on average) compared to the global increase and that a 4°C temperature increase will increase the SLR to about 850-1250 mm by the period 2080-2100 (IPCC, 2013). A large population along the coast is at risk from coastal flooding and adaptation costs could rise to over 9% coastal Africa GDP (Niang-Diop et al., 2005).

There are approximately 33 countries and 7 islands that form the belt of the African coast, which are very productive environments affected by various

38

hazards caused by storm surges, floods, hurricanes and cyclones worsened by sea level rise. Most of these hazards have caused severe flooding and erosion, which has claimed many lives and valuable assets (El-Shahat et al., 2019). Socioeconomic impacts within African communities have also exacerbated their vulnerability, making the future impact of SLR even more devastating.

Analysis of in situ sea level measurements for Ghana from the Takoradi station from 1925 to 1970 (Figure 3) shows that sea level is rising by 2.1 mm/yr, which agrees with estimates elsewhere (IPCC, 2007; Woodworth et al., 2009). The measurements from 1970 to 1996 appear biased due to instrument aging and mechanical problems with the tide level (Figure 3). The gauge ultimately failed in 1996, and was later replaced in 2008, resulting in missing data from 1996 to 2008, making remote sensing data very important in identifying current sea level rise. The African center of meteorological application for development (ACMAD) predicted in 2016 that warming in Africa could reach 1.5°C at the end of 2050 and increase to 3°C after 50 years. This could worsen the impact and exacerbate the effects of continental climate change. This will aggravate the severity and speed of tide and possibly cause coastal flooding.
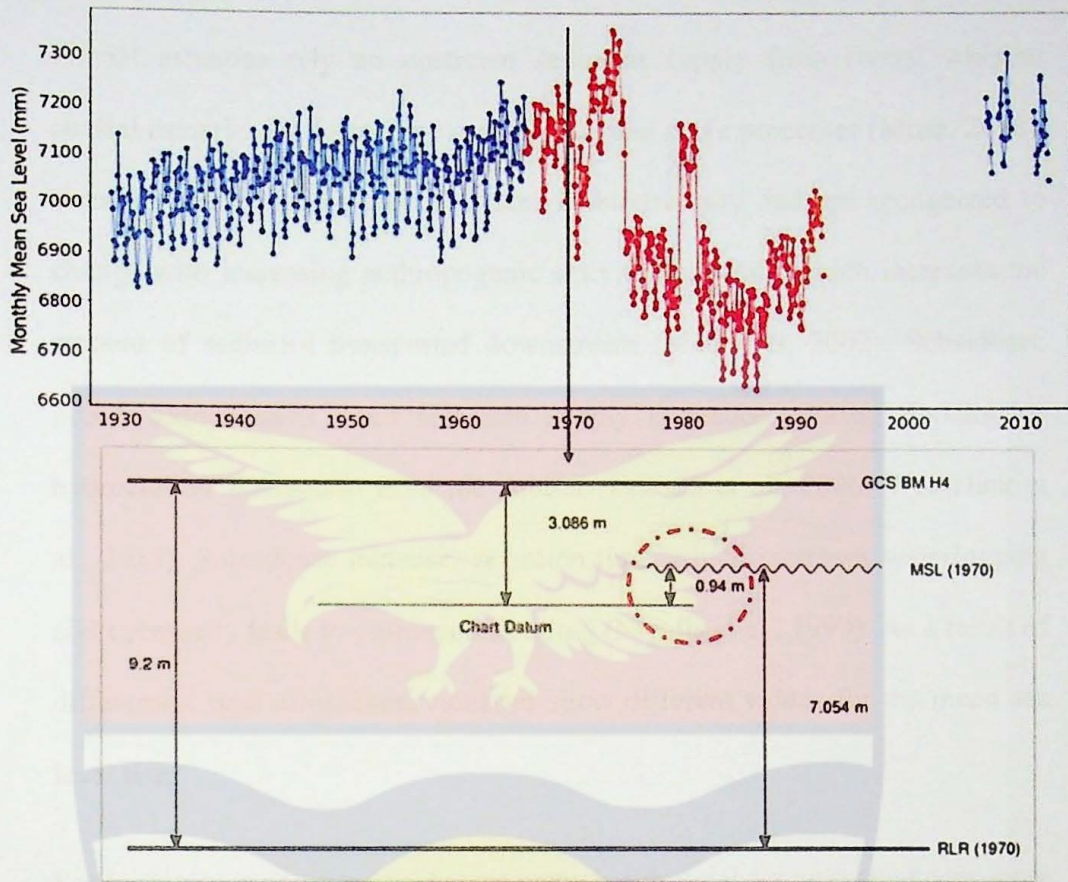
Figure 28: In-situ measurements and sea level analysis of Takoradi gauging station, Ghana. Source: Permanent service for mean sea level 2013; Cited in Isaac et al., 2017

Sea level rise can reduce the availability of freshwater for domestic use and affect the freshwater habitat of aquatic organisms (IPCC, 2007b; Van, et al., 2012). These impacts may not be uniform globally but may be subject to the dynamics of the social, physical and economic situations of coastal zone. Accordingly, different areas may experience different intensities of sea level. Relative sea level rise is the change in sea level with respect to land elevation at a given location. Its value is therefore greater where land subsidence occurs than in stable coasts. Coastal processes such as river channel flow, tidal currents and waves determine the unique characteristics of a particular coastal landform (Nicholls et al., 2007).

40

Fluvial estuaries rely on upstream sediment supply from rivers, whereas coastal estuaries are formed by coastal tidal and wave processes (Musa, 2018). Estuaries are typically very abundant in biodiversity and are recognized to change with increasing anthropogenic activity upstream, which increases the amount of sediment transported downstream (Mcmanus, 2002). Subsidence occurs along coasts when sediment supply is reduced during flooding or hydrocarbon abstraction from the aquifer (Ericson et al., 2006; Wesselink et al., 2015). Subsidence increases retention time, which increases waterlogging and eventually leads to prolonged flooding (Nicolls et al., 1999). As a result of differential land subsidence, estuaries show different values for the mean sea level rise.

Sea level rise is predicted to disrupt many biophysical activities that contribute to the development of mangrove terrain elevation. Sea level rise is expected to lengthen the hydroperiod, which may result in allochthonous sedimentation and possibly vertical accretion. Sediment accumulation results in increased nutrients that can affect the growth and decomposition of mangrove root (McKee et al., 2007; Lovelock et al., 2011b). Sea level rise increases water depth and allows tidal currents into the mangrove ecosystem and subsequently increases the rate of erosion (McKee et al., 2007). Sea level rise will aggravate waterlogging of the mangrove ecosystem, potentially affecting root growth in some mangrove species and leading to severe hypoxia (McKee, 1996). Sea level rise is likely to raise groundwater levels and increase saltwater intrusion, affecting plant growth. While few studies have examined the response of

41

mangroves to local sea level, it is evident that sea level changes may affect the mangrove ecosystem in a variety of ways.

Selected Indicators for Coastal Vulnerability

Vulnerability could be described as the inherent properties of an element that determine its susceptibility or level of proneness of an element (person, property or environment) to the adverse effects of hazards. The exposure indicators for this study were chosen because of the possible contributions to coastal flooding, seawater intrusion and erosion. All indicators are mainly real characteristics of the coast apart from nearness to the sea and population density, which are human variables.

Topographic Considerations

Topography is related to the height of an area above mean sea level and is an important indicator of how the area will be influenced by sea level rise because low-lying areas are easily flooded and there is a correspondingly greater risk of property damage from flooding and other storm processes (Van et al., 2012). Recent study by El-Shahat et al. (2019) points out that major coastal estuaries in Africa are flat, making them vulnerable to coastal flooding. This has resulted in eroded beaches (particularly sandy beaches) and increased soil and water salinity

Coastal Slope

Slope is a measure of steepness in relation to the adjacent land and is an important indicator of the vulnerability of the coast. The slope controls the overflow of water and subsequent flood. For this reason, places with gentle

42

slope are more susceptible to tide as compared to places with steep slope (Aich et al., 2014). El-Shahat et al. (2019) reports that 9% of the African country has a slope <0.1% (extremely vulnerable), 21% a slope between 0.1-0.5% (very vulnerable), 18% a slope between 0.5-1% (moderate vulnerable) and 28% have a slope <= 3% (low vulnerability), 24% have slopes > 3% (very low vulnerability). This indicates that large coastal estuaries in Africa have gentle slopes where slight increase in water level can inundate a huge area.

Geomorphology and Soil Type

Geomorphology is a term used to describe the formation of landscape patterns and the processes that shape them. The nature of coastal landform governs its vulnerability to erosion and its resilience to tidal forces. Rocky terrain and cliffs are less vulnerable, lagoons and estuaries are more vulnerable while beaches, deltas and offshore islands are highly vulnerable (Pendelton et al., 2010). During coastal flooding, flood water seeps into the soil depending on the size of the pores. This process relates to infiltration, which depends on soil type, structure and moisture content. The process of infiltration is a crucial factor in dealing with floods. Sandy soil has a higher infiltration rate than other soil types. The tidal erosion process relies on the gradient of slope, structure of the soil and rate of flow. Soil classification and its hydrological groups are shown in Table 6.

Table 6: Hydrological Soil Groups and Infiltration Rate

Soil Group	Rate of Infiltration (in/h)	Soil Description	Potential of Run-off
A	>= 30	Sand, loamy sandy	Low
B	0.15 to 30	Sandy loam, loam	Moderate
C	0.05 to 0.15	Sandy clay loam, silt loam	High
D	0 to 0.05	Clay loam, silt clay loam, sandy clay & clay	Very high

Source: National engineering handbook, 2009; Cited in Aja et al., 2019

Relative Sea Level Rise (RSLR)

RSLR refers to the height of the sea above a known datum, recorded with tide gauges and averaged over a year (Yin et al., 2012). The larger the RSLR, the more susceptible a place is. In recent decades, many scholars have focused on the impacts of relative sea level rise around the world (Gornitz et al., 2001; Walsh et al., 2004; Miller et al., 2013; Ezer et al., 2014; Wadey et al., 2017; Rehman et al., 2020), emphasizing the relevant exposure to coastal hazards for low-lying areas and small island states. The relative change in sea level is the result of the combined effects of polar ice cap advance or retreat (eustasy) and vertical tectonic movement, which show significant spatial and temporal variability (Fabrizio et al., 2020). Relative SLR can lead to a long-lasting retreat of many coasts worldwide by shifting the coast inland or by introducing sediments into inlet systems (Toimil et al., 2020). Varying the relative SLR

44

could have significant effects on near-shore hydrodynamics and lead to more cases of extreme thresholds (Wahl et al., 2017; Vousdoukas et al., 2018). This can potentially exacerbate tidal flow as a result of nonlinear interactions (Arns et al., 2017; Idier et al., 2017).

Yearly Rate of Shoreline Erosion

The extent of spatial soil erosion along the coast influences sea level rise response. Given coastal vulnerability, places affected by erosion are expected to be more vulnerable, while areas accumulating sediment are less vulnerable (Kumar & Kunte, 2012). Coastal erosion control in climate change context can be achieved by making accurate projections of long-term coastal changes (Toimil et al., 2020). Information about the annual rate of coastal erosion can be used to define setback limits, plan for the relocation of affected people or assets, anticipate potential losses to flood defences and recreation, and decide whether or not to implement protective measures such as beach replenishment (Jongejan et al., 2016; Stripling et al., 2017; Mehvar et al., 2018).

Average Range of Tide

The mean range of tide is the variance between averaged high tides and averaged low tides and it is directly related to coastal hazards resulting from sea level rise (Yin et al., 2012). Considering coastal susceptibility, places with wide range are more vulnerable compared to places with small range. Average range of tide is calculated using time-series tide data, but in situations where this data is unavailable, a hydro-dynamic model can be used to forecast tidal level (Kumar & Kunte, 2012). Tidal current affects sediment transport,

45

morpho-dynamics and alternately exposes or inundates much of the adjacent beach and inner surf zone (Davis, 1985).

Average Height of Wave

Wave moves sediment from a point to a different point along the coast. The theory of linear wave states that the energy from wave is comparative to wave height squared. Hence, wave height can be used as a substitution for wave energy (Yin et al., 2012). Places with higher waves are more susceptible than areas with low wave heights. Climate change is altering wave propagation (Wong et al., 2014; Morim et al., 2019). Fluctuations in wave propagation can increase or lead to a decrease in coastal drift (Idier et al., 2013) and can cause alterations in the rate of oscillation on seashores (Ranasinghe, 2016). Variations in wave conditions may increase erosion along the coast.

Population Density

Densely populated areas are more vulnerable to coastal disasters (Mclaughlin et al., 2002). Human settlement in coastal areas increases the cost of risk, coastline modification and the likelihood of erosion. El-Shahat et al. (2019) reports that Ghana is one of the fourteen countries in Africa with sizeable urban populations along the coast.

Nearness to the Coast

The nearness of assets to sea governs its vulnerability to storm surges, flooding, erosion and waves. As communities in high-flood-risk zones increase worldwide, the number of people exposed to flooding and other coastal hazards will most likely increase. Any increase in disasters, regardless of magnitude, will affect development efforts. Proximity of land to coast is a

46

very important parameter reflecting land exposure to SLR effects. Accordingly, areas located within 2.5 km to 5 km from the coast are at high risk (El-Shahat et al., 2019).

Coastal Resilience

Resilience originated from ecological discipline as a valuable theory for researchers in the area of environmental related hazards. According to Holling (1973), resilience is the measure of a system's capability to resist changes in state-variables, drive-variables and parameters. This theory emphases on an ecosystem's ability to quickly recover from a major disruption and continue to support its core functions. In coastal risk management, resilience has been described as the capacity of a system to bounce back from coastal hazards (Bruijn, 2004). For social-ecological system, Adger et al. (2002) describes resilience as the capacity of a system/structure to manage the impacts of external pressure while preserving the basis of life. Here, a system/structure refers to different organizational levels, which can be households, communities, economic sectors, or population groups (Brooks, 2003). For Buckle (2006), resilience means the capacity to survive loss, while Norris et al. (2008) defines resilience as a procedure that combines a number of adaptation abilities with positive operation after a disruption.

Resilience as an idea was seen in a web of socio-ecological systems (Folke et al., 1998; Adger, 2000; Folke, 2006). System resilience has to do with the ability of renewal, reformation as well as development in a socio-ecological system and the ability to preserve its uniqueness (Walker et al., 2004; Cumming et al., 2005; Maguire & Hagan, 2007). Three major attributes of

47

resilience occur in literature, regardless of different definitions from different disciplines (Carpenter et al., 2001). The first attribute has to do with the speed of recovery from disasters (Bruijn, 2004). Second deals with the extent of a disaster (Colding et al., 2003). The last attribute relates to the ability to acquire knowledge from disruptions and help build new things (Folke et al., 2002, Berkes & Seixas, 2005).

Consequently, the traditional method of measuring resilience in terms of the rate at which a system recovers may not explain its full meaning as multiple factors such as those relating to demography, economic, political, social, cultural, and geographic environment must be considered (Gaillard, 2007). Nonetheless, such factors are always changing at various stages of investigation (Adger, 1999; Buckle, 2006; Brouwer et al., 2007). Understanding the change/uncertainty, adaption and co-creation for self-reorganization have been shown to be important factors in building household resilience in Cambodia (Marschke & Berkes, 2006). Other researchers such as Marshall and Marshall (2007) identified the ability to learn, plan and self-reorganization among the factors that help measure an individual's resilience level at a study conducted in Australia.

Norris et al. (2008) identified socio-economic development, access to information/capital and community literacy as important skills that can build community resilience. Socioeconomic development in this context refers to growth in the economy, stability of livelihood and equitable circulation of resources for the people (Adger, 1999) and societal support systems between and within the community (Mathbor, 2007). Access to information refers to

48

early warning systems for providing information to the public. Community competency denotes the ability of members of the community to learn how to solve problem and collaborate. Resilience is multi-dimensional in nature and therefore it is hard to apply in reality (Cumming et al., 2005).

Marschke and Berkes (2006) used a subjective well-being method to implement resilience based on livelihood perspective in Cambodian. However, they used a qualitative method to study household and community well-being without quantifying indicators of resilience. Some researchers are of the opinion that well-being has to do with feeling and thinking (Copestake & Camfield, 2009). This type of subjective well-being approach has been generally accepted in livelihood research particularly in developing countries (Narayan et al., 2000). Adaptation can be more active in mitigating hazardous effect if the existing resilience of the system is properly assessed (Brooks, 2003). This will show how to change the characteristics of the system that directly affect its resilience, such as: the nature of the terrain, over population or lack of clean water, etc. System resilience indicates its capability to adapt and also to take advantage of disasters as a future opportunity (Alwang et al., 2001). Resilience is composed of physical components (e.g dikes) and nonphysical components (e.g past experiences).

Plans for resilience can be properly initiated for a system or carried out through casual series of events. Official resilience plans are properly planned prior to execution. Conversely, the informal resilience approach has been part of the traditional knowledge of the people for years. Unofficial approaches are: (1) Emergency response methods developed in time of hazard, (2)

49

attempts by the people to protect their property; these are mostly reactive in nature, depending on the readiness of individual resources (Bierbaum et al., 2013). Formal plans are usually intentional efforts by governments to improve people's livelihoods (Bachmair et al., 2012).

Coastal Adaptation and Mitigation Strategies along the West Africa Coast

The coastal zone of the Gulf of Guinea is currently facing an imminent transformation in terms of infrastructure, tourism, fisheries, agricultural expansion and general urban growth. Demographic pressure along the coast is leading to excessive natural resource degradation and unprecedented coastal pollution (World Bank, 2016). Especially, the coastal areas covering Ghana, Togo, Benin and Nigeria, are witnessing a high rate of erosion and sand mining, leading to the depletion of land and other assets. As sea levels keep on rising due to climate variability, coastal hazards along these areas have also increased (ESA, 2012). Sea level rise and its attendant effects require a reassessment of coastal protection plans and strategies (Musa, 2018). Coastal protection plans go beyond physical protection and include a combined impact of preparedness, mitigation and prevention (World Bank, 2016). Coastal research in the past showed that coastline was fairly stable but slightly influenced by sea level, nevertheless, the situation is different since 20th century as a result of anthropogenic intervention (Tilmans et al., 1991).

Coastal interventions that caused severe erosion within the Gulf of Guinea are the Port of Lagos (1908-1912), the Port of Cotonou (1960), the Akosombo Dam (1963), and the Port of Lome (1964). The construction of coastal harbors

caused erosion in the downward drift areas. For example, following the construction of the Port of Lome, erosion took its toll on densely populated areas downward the coast, threatening valuable coastal infrastructure and necessitating the construction of permanent groins to protect the affected areas. The Republic of Benin is also threatened by erosion due to the port of Cotonou in connection with sand mining at Seme (Addo et al., 2011).

The coast of Ghana is not spared as around 50% of the 550 km of coastline are highly endangered, particularly in the Volta Basin (NBCC, 2011). Ghana, with a large fishing community (about 2.9 million) along the coast, is severely affected by erosion due to natural and anthropogenic interference (Tilmans, Jakobsen & LeClerc, 1991). Rate of soil loss in Keta area has been reported to be between 8 and 10 m^{-year} because of the blocking of sediments from Volta River by the Akosombo Dam (Addo et al., 2011). Structural coastal defenses were built to protect the coastline around Keta from erosion (Nairn et al., 1998). Notable projects include the Keta Sea defense Project (KSDP), which was completed in 2004 and involved dredging, construction of groins, and evacuation of vulnerable people (Danquah et al., 2014). Keta Sea defense Project significantly decreased erosion at Keta area but amplified the severity of down-drift erosion in the areas east of the KSDP and around the Volta Estuary (Addo et al., 2011; Appiah, 2016).

The coastline of Nigeria (approx. 850 km) is home to the most densely populated cities in Africa. Notable among them is Lagos, which has a population of over 20 million and is constantly growing (NPC, 2010; World Population Review, 2017). Due to population pressures, the Lagos coast has

51

faced various man-made encroachments ranging from harbor construction, sand mining from the beach and dredging, as well as the new construction of non-natural islands, making the coast very dynamic. Human-induced interventions have affected the coasts of West Africa, creating changes of erosion and accretion patterns (Musa et al., 2015). Quite a lot of shoreline maintenance techniques have been employed to protect the shoreline, including sand nourishment, creation of groins and revetments (Orupabo, 2008).

Modeling the morphology and Hydrodynamics of Wetlands in a Data Scarce Areas

Numerical modeling of coastal dynamics in estuaries and wetlands is anchored on the principles of continuity, mass and momentum conservation. Considering a controlled volume of water in a channel for an unsteady flow, the principles of conservation of mass and momentum dictate that the mass inflow minus the mass outflow equals the rate of change of volume. The momentum equation explains the forces acting on a controlled volume of water. Dependent on the characteristics of a channel, averaging is performed so that the flow of water can be modeled using either one dimension, two dimensions, or three dimensions. In order to model wetland dynamics, in-situ data of water levels, soil friction and topographical information are important. However, the unavailability of data has set back many researchers, particularly in developing countries.

Two-Dimensional Modeling of Tides

Lamb (1932) made the first attempt to understand tidal processes through systematic studies of the linearization equations of motion. With the advent of computers, numerical models using finite difference elements for more accurate representation of tidal hydrodynamics gained importance (Leendertse, 1967). In the late 1960s, several researches were carried out at the University of Waterloo, Canada to study the flow properties of vegetated canals (Kowen et al., 1969). These studies included several laboratory experiments in which roughness elements were attached to a flume, then water flow was generated over the roughness elements, monitored and controlled by means of a pilot tube method to record velocity distributions. The study proposes using a logarithmic law to fit the standards of the roughness parameter and the intersection point to plot a vertical profile of the average velocity. This assumes that there is equilibrium over the roughness elements and that turbulence generation is balanced locally.

Numerical modeling was used by Li and Shen (1973) to forecast the transportation of sediment in a vegetation area using a turbulence superposition technique. The assumption was that local drag coefficients had a value of 1.2 and gave average drag coefficients of 1.1 for turbulent activities with no plant density, and they related the effects on sediment yield for different forms of tall vegetation. A quantitative approach to estimate manning's roughness as a measure of drag was developed by Petryk and Bosmajian (1975). This technique examines the depth of flow, which is either less than or equal to the highest vegetation, and is important in estimating the

variations in manning's roughness with respect to the change in depth. Alternatively, the use of biomechanical concepts and field methods to estimate the roughness of natural vegetation has been proposed by Kowen and Li (1980).

A mathematical model for estimating conservation of momentum in multi-connected flows was developed by Raupach and Shaw (1982). Following this mathematical approach, Raupach et al. (1986) performed several experiments that highlighted the nature of atmospheric flows over a vegetation using wind tunnel in a laboratory to generate currents and atmospheric flows over an artificial canopy of vegetation. The velocity measurement was obtained on the simulated canopy and several terms constituting the balance of kinetic energy within the canopy were estimated. Their results underscored the importance of turbulent kinetic energy over the canopy in channel flow modelling. Temporal domain separation was difficult in linear models because of local changes, leading to the development of time steps. This approach was able to solve the shallow water equation for tidal dynamics with higher accuracy and allowed the model to look more closely at tidal component relationships (Westerink, 1989). It was also considered that water circulation affects the overall performance of the model and a finite element technique was used to overcome instability because of nonlinear flow occurring at the water and land interface (Sidn & Lynch, 1988). In addition, the general wave equation was developed to solve the tidal motion equations using a finite element mesh that draws a clear boundary line for the model.

Based on the relationship between turbulence generation and energy transfer between aquatic plants, Nepf (1999) setup a model representing vegetation resistance and intensity of turbulence. D'Alpaos et al. (2006) advanced a numerical model to improve the cross-sectional view of channel flow, capturing sediment dynamics in the channel, vegetation changes and water flow resistance, and biomass gain as a result of vegetation. The effect of hydroperiod on vegetation survival on the indicated channel section is also captured by the model.

Despite the importance of the General Wave Continuity Equation (GWCE) in the linear flow model, field studies have shown that there is still room for improvement. Accordingly, Lüttich et al. (1992) developed the ADCIRC model, which uses finite element 2D and integrates depth while accounting for geometric boundaries, bathymetric differences, and elevation changes. The advanced circulation model was validated and used in different estuaries and flood plains for hydrodynamic tidal marsh productivity modeling as well as flood assessment (Bcaopoulos et al., 2008; Hagen et al., 2012; Alizad et al., 2014). Militello et al. (2004) documented the coastal modeling system (CMS), which calculates hydrodynamics, morphology and sediment changes under general tidal, wave and wind forcing. CMS can be coupled with the ADCIRC model (Luettich et al., 1992).

Tidal Wetland Analysis

Water inflow into any coastal wetland is primarily caused by tides. Tidal current account for most of the energy in the ocean and can therefore be predicted. Semi-diurnal tides account for about 80% of the kinetic energy

exchange processes on the inner and middle shelves (Blanton et al., 2004). The earliest models used for tidal simulation revealed significant differences between the theories and practical measurements. This has led to further advances in newer models that can better simulate tidal flow and circulation. There are basically two types of tidal circulation with a number of individual components, namely: semi diurnal and diurnal. Diurnal tides refer to daily tides with a single low tide and high tide on each tide day, while semi-diurnal tides refer to daily tides with two low tide and two high tides on each tide day. A tidal constituent refers to the push or pull exerted on the ocean by a massive body like the moon.

There are various tidal constituent and their changing relationship with the global ocean, resulting in daily fluctuations in tides in different locations. The National Oceanic and Atmosphere Administration (NOAA) considers 37 constituents to represent full tide. Of the 37 tidal components defined by NOAA, there are 8 major components of interest: N2, K2, M2, S2, K1, O1, Q1, and P1. The major lunar semi-diurnal tide with the greatest effect on ocean tides is designated M2 and occurs every 12.4 hours. The main solar semi-diurnal tide is denoted S2 and occurs every 12 hours. The elliptical lunar semi-diurnal tide which occurs every 12.7 hours, is N2. The luni-solar semi-diurnal tide, which occurs every 11.97 hours, is K2, while K1 is the daily lunar tide, which occurs every 23.9 hours. The second daily lunar tide that occurs every 25.8 hours is O1 and P1 is the solar daily tide occurring every 24 hours. Finally, Q1 is the Moon's major elliptical diurnal tide and occurs every 26.9 hours. Each of the constituents has a different frequency and amplitude,

56

creating a varying total collective tide when they come together. This phenomenon recurs after 15 days. Tidal components are key variables for most numerical models used to simulate tidal energy. Tidal responses occur at different frequencies, which are determined by combining astronomical frequencies and frequencies of nonlinear exchanges in Basic Principles (Parker, 1991).

In lagoons and estuaries, in addition to tides, other factors affecting water circulation within the area are wind, bottom roughness, water inflow, rainfall and evaporation, making the physical science behind estuarine circulation very complex. The estuary system is highly dependent on tidal, bathymetric, and bottom roughness conditions, as well as turbulence energy. Regardless of the complexity of estuaries and wetlands, the key feature is the interchange of flows within the system in averaging circulation (MacCready & Geyer, 2010). From first-generation models to current models with many improvements in tidal energy parameterization, the evolution of equilibrium flow continues to use similar assumptions and solutions.

The dynamics of a wetland is represented by the rate of accretion with respect to hydroperiod. The accretion itself results from the inorganic and organic entrapment of sediment and the production of organic matter within the wetland. There is a relationship between wetland accretion and biomass production with respect to the tidal hydroperiod (Morris, 2002). Therefore, if biomass productivity and its change because of sea level rise is modeled in coastal wetlands, the effects of sea level rise could be effectively quantified. Tidal dynamics can be modeled using a 2D hydrodynamic model to provide

sea surface elevation when a number of parameters are known as well as the site bathymetry (Alizad et al., 2015).

Models for Wetland Studies

In general, modeling the wetland environment is very difficult and has only gotten easier with the rapid growth of computer programming over the past several decades. Basically, the solution lies on the Navier-Stokes equations for shallow water using various numerical techniques. With a two-dimensional (2D) depth averaged model, the analyses become faster. Several studies have been performed on 2D models that do not account for wetland depth, most of this work had several limitations in predicting reality (Trepel et al., 2000; Ganju et al., 2016; Iglesias et al., 2019). Therefore, it is recommended to utilize a depth integrated 2D model that considers the depth of the wetland platform. The most commonly used 2D models for wetland studies are: WASP/DYNHYDR5, Surface water modeling system (ADCIRC and CMS) and Mike21 (Danish Hydraulic Institute) Delft3D, TELEMAC-MASCARET, SWASH, ROMS, MOHID, SELFE, Tuflow-FV, FVCOM etc.

The main difference between 3D and 2D models is that 3D bathymetry consists of several small cells that can create any desired volume. In 3D and 2D models, the volume of water is defined using bathymetry and the characteristics of the water and the area. Factors such as evaporation, barometric pressure and wind can be added for these types of models. They are essentially powered by gravity, air pressure and wind. The model is able to simulate various biological processes, physical processes and chemical

58

processes. The pro of 2D model over 3D model is that it is less time consuming both in terms of mesh generation and simulation time.

Strength of CMS Model for Nearshore Modeling

The coastal modeling system (CMS) is a 2D finite volume circulation and morphology model that solves the shallow water equation to calculate water surface elevations, current velocity and transportation of sediment on a quadtree grid (Militello et al., 2004). CMS has been integrated into the surface water modeling System (SMS). CMS has three sediment transport modules (Buttolph et al., 2006), which are linked to the CMS-flow to calculate morphological changes and sediment exchanges on grid cells (Buttolph et al., 2006). One more vital attribute of the model is the depiction of nonerodable cells which can be a coastal defense structure (Hanson & Militello, 2005).

CMS encompasses menus and control modules within SMS that permit the specification of input and output and the level of interaction among the various processes. SMS also comprises utilities for data visualization, result calculation, monitoring of simulation progress, and execution of the project. CMS-Flow is very effective for computation, simple to setup and has all the features essential for coastal engineers. The model has been used in many inlets and the sensitivity have been highly tested.

Researchable Issues using CMS Model

The Coastal Modeling System (CMS) was developed and verified in multiple researches dealing with bathymetric analysis. CMS was primarily used to study hydro-dynamic behaviors on the Texas coast (Brown et al., 1995). CMS has been used to assess water velocity fluctuations in the Gulf Intracoastal

Waterway (Militello & Kraus, 1998). CMS was used to analyze wind-forced circulation in the non-tidal bay of Baffin (Militello, 1998; Militello & Kraus, 2001). Militello, (2002) and Militello et al. (2003) used CMS to calculate flow velocity of one month time interval and changes in bed elevation. A successful coupling of CMS with ADCIRC was demonstrated by Militello and Zundel, (2002). CMS was used by the USA army corps of engineers (USACE) coastal inlet research program (CIRP) to calculate tidal and wave forced currents at an ideal inlet and ebb shoal for storm waves (Militello & Kraus, 2003). Another study by Militello and Zundel (2003) demonstrated how to couple CMS and STWAVE (a surface wave model) and its ability to compute morphologic changes and sediment transport. Current uses include the computation of hydro-dynamics and morphologic changes for both tidal and wave driven (Bounaiuto & Militello, 2004; Lin et al., 2004). Batten and Kraus (2006) used CMS flow to assess bank erosion at Mattituck Inlet, New York. Buttolph et al. (2006) described improvements in the two-dimensional circulation model (CMS) and its ability to compute sedimentation at inlets, shipping channels and adjacent beaches. Li et al. (2009) presented efforts to numerically model littoral sediment transport to simulate physical processes on high-energy coasts at the Bight of San Francisco, California. Snchez et al. (2011) utilized the coastal modeling system (CMS) to model the long-term morpho-dynamics of coastal barrier inlet systems.

Summary of Literature Review

Coastal vegetation like mangroves, seagrasses and salt marsh provide ecosystem services and sequester more carbon dioxide than terrestrial counterparts due to their productivity. They are beneficial to the survival of

millions of people. Mangroves have experienced significant anthropogenic degradation. Mapping mangrove extent is critical to understanding progress towards achieving SDGs, as it serves as indicators for monitoring local, regional and global progress. To address issues related to the effects of anthropogenic degradation and climate variability on coastal ecosystems, timely and accurate information on mangrove dynamic trends is needed. Though there have been several efforts to assess mangrove ecosystem in Africa, most of these studies have always used optical satellite imagery which is affected by cloud cover. In the present study, a new method that combines optical and radar imagery to reduce the effect of cloud cover was proposed. Also, the impact of climate change on mangrove ecosystem have been reported in literature. However, information on these impacts vis-à-vis the response of mangroves is limited in Ghana. Therefore, a 2D model was used to study the impacts of sea level rise on mangrove ecosystem.
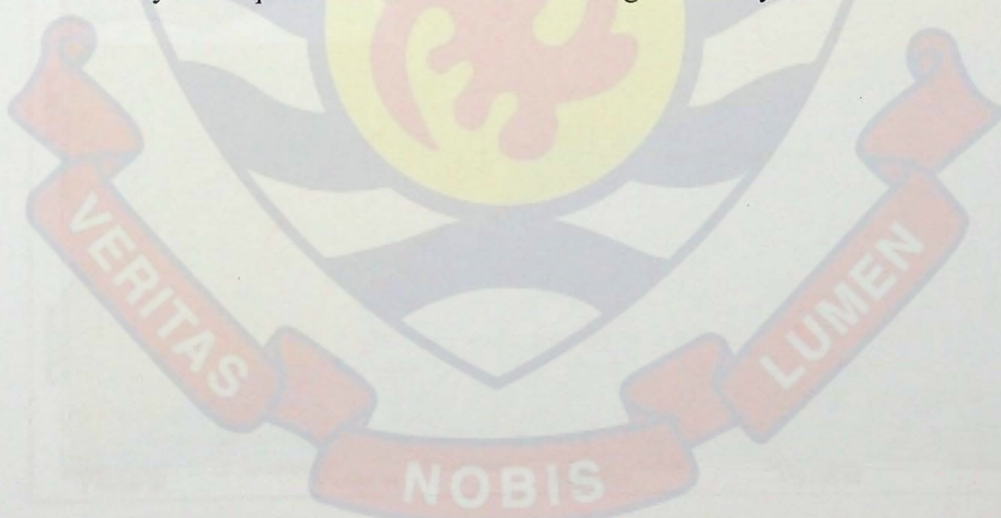
CHAPTER THREE

METHODOLOGY

Study Location

This study was conducted at the Anlo Beach Wetland complex which is situated along the coastal belt in Shama District, Western Region of Ghana as shown in Figure 4. The study domain covers about 50.42 km^2 and lies roughly within latitudes 5°1'30"N and 5°3'5"N, and longitudes 1°34'30"W and 1°37'30"W. The area is covered by relatively disturbed mangrove vegetation, lying within the plains of Pra River which opens directly into the Atlantic Ocean (Friends of the Nation, 2014).
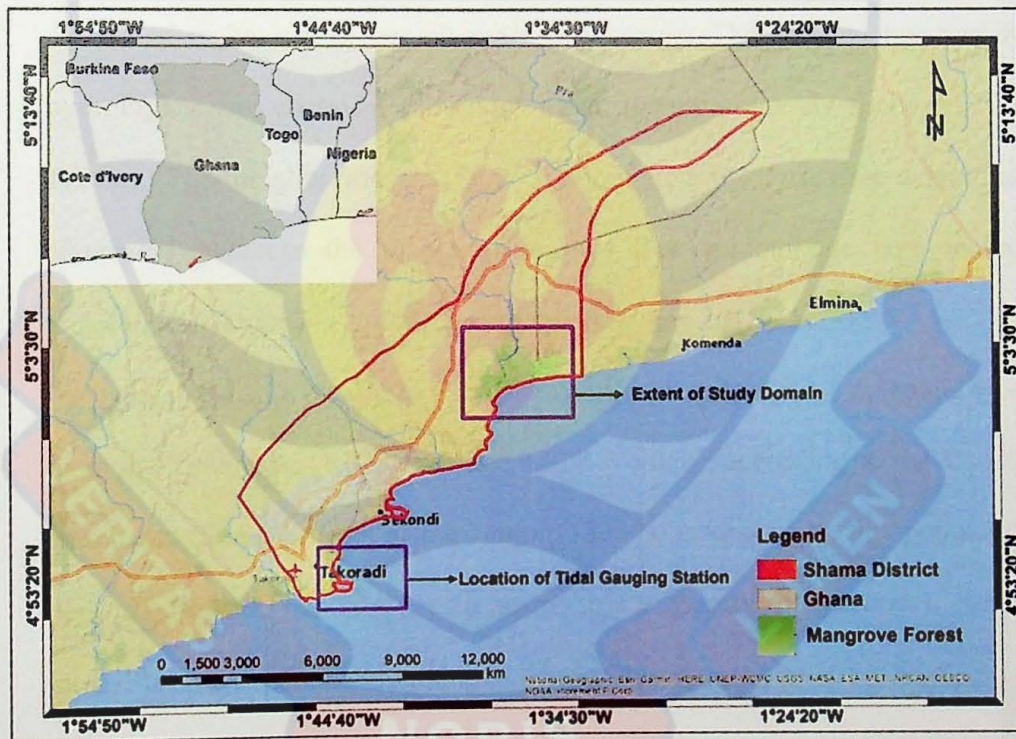
Figure 29: Map of study location

Anlo Beach is situated at the lower area of Pra River Basin which is characterized by high surface temperature of about 21.74°C to 31.6°C for minimum and maximum (Bessah et al., 2018). The climate of this area is classified as tropical monsoon (Am) (Kottek et al., 2006), with mean monthly

62

relative humidity greater than 70%, all year round (Kwabena et al., 2013). The dominant soil types in the upper part of the basin are Acrisols and Lixisols which are characterized by fairly high possibility for runoff (Ross et al., 2018), exposing the low parts of the watershed to water disasters during periods of heavy rainfall (Bessah et al., 2020).

A Friends of the Nation (2014) on-site survey found that the elevation is generally low and ranges from 0 - 42m, the shoreline has an uneven sandy beach, and the sea areas are typically open, with medium- to high-energy pounding surf as the dominant wave type. According to the Coastal Resources Center and Friends of the Nation (2010), the rate of coastline erosion has been calculated to be 100 m per 50 years on average. The wetland has varying hydrological and chemical conditions and it is predominantly shallow (0.25– 1.5 m). The neighboring marshes is dominated by *Paspalum vaginatum (Poaceae)*, whereas the mangrove species that predominate here include *Avicennia, Rhizophora,* and *Laguncularia* (Okyere, 2018).

An estimated 2,231 people live in the Anlo Beach community, the majority of them are fishermen (1,028 men and 1,203 women), according to the Coastal Resources Center/Friends of the Nation, (2010). Additionally, this population depends on the mangrove ecosystem for a variety of purposes, which intensifies the dynamics of land use change.

Research Design and Methodological Approach

To address the stated objectives, this study was organized into four sub-headings, namely mangrove extent mapping, mangrove structural assessment, hydrodynamic modelling, and mangrove growth or mortality under different SLR. A cloud-based computing through Google Earth Engine (GEE) was

implemented as a novel approach to mangrove assessment and monitoring. A field campaign was conducted for ground truthing and to capture domain characteristics which were fed into a remote-sensing based wetland Response Model with biological feedback, to forecast mangrove ecosystem responses to sea level rise as a climate driver. Radar and optical satellite data were used in GEE to study the impact of using different remotely sensed data on the precision of mangrove mapping and assessment.

Mangrove Extent Mapping

Mangrove extent maps were created by classifying both optical and radar images separately and in combination. The maps were created for two time periods, namely 2009 and 2019, to examine changes in mangrove extent over time. The Google Earth Engine database was filtered for Sentinel-1 imagery that is in Wide Swath (IW) interferometric mode, descending pass, 25 m resolution, VH and VV polarization and falls within the region of interest. The Sentinel-1 dataset was filtered by date to retrieve images from 2019. The 2009 ALOS PALSAR-2 image was acquired from the JAXA website (Table 7). The corresponding Landsat8 and Landsat 7 images were also retrieved from Google Earth Engine database. The images: Landsat 8 surface reflection Tier1, Landsat 7 surface reflection Tier1, Sentinel-1 image, PALSAR-2 image and global mangrove distribution data were called into the Google Earth Engine code editor. Then the images were visualized in the layer bar. A speckle filter was applied to the SAR images to minimize speckle noise (Ayman et al., 2017) and the speckle filtered images were also added to the layer bar (Figure 5). The Sentinel-1 dataset in the Google Earth engine is ready for analysis

because it has already undergone processing such as formal noise removal, terrain and radiometrically corrected. The ALOS PALSAR-2 data was converted from Log10 to decibels (db) using the formula below (Jaxa, 2006; Lavalle & Wright, 2009).

$$\gamma 0 = 10 \log 10 \langle DN^2 \rangle + CF \dots\dots\dots\dots\dots\dots\dots\dots\dots\dots\dots\dots\dots\dots\dots 1$$

Where $\gamma 0$ = Sigma naught in dB, DN = digital number (pixel value), CF (calibration factor) ~ -83.0 for the PALSAR data.

The quality of the optical images was improved by creating a function that removes cloud shadows (Hansen et al., 2013). The normalized difference vegetation index (NDVI) was calculated from the optical image to obtain a composite image, which was used as an information layer to inform the classifier (Nathan et al., 2018). Then the image was also added to the layers. This procedure was done with Landsat 8 (for 2019) imagery and Landsat 7 (for 2009) imagery.

Table 7: Description of Datasets used for Mangrove Extent Mapping

S/N	Data Type & Date	Description	Source
1	Sentinel 1 (2019)	A synthetic aperture radar (C-Band) with interferometric wide swath mode (IW), having a descending pass, a resolution of 25 m, dual polarization of VV and VH. Image Collection ID: ee.ImageCollection("COPERNICUS/S1_GRD"), more details can be found at https://developers.google.com/earth-engine/guides/sentinel1.	Google Earth Engine Platform Database
2	ALOS PALSA	A synthetic aperture radar at L-Band, having a 10^0 X 10^0 in longitude and latitude, a resolution of 25 m, dual	Japan

65

	R-2 (2009)	polarization of HH and HV, this data has been ortho-rectified and slope corrected. Image Collection ID: N06W002_09_sl_HH, N06W002_09_sl_HV available at http://www.eorc.jaxa.jp/ALOS/en/palsar_fn f/fnf_index.htm	Aerospace Exploration Agency (*JAXA*) EORC
3	Landsat 8 Surface Reflecta nce Tier 1 (2019)	Has been atmospherically corrected and contain five visible and near-infrared bands, two short wave infrared bands and two thermal infrared bands. Image Collection ID: ee.ImageCollection("LANDSAT/LC08/C01/T1_TOA"). More details at https://landsat.usgs.gov/	Google Earth Engine platform database
4	Landsat 7 Surface Reflecta nce Tier 1 (2009)	Has been atmospherically corrected and contain four visible and near-infrared bands, two short wave infrared bands and one thermal infrared band. Image Collection ID: ee. Image Collection ("LANDSAT/LE07/C01/T1_TOA"). More details at https://landsat.usgs.gov/	Google Earth Engine platform database
5	Global Mangro ve distribut ion vector (GMW) (2010)	A baseline global distribution map of mangroves for year 2010. GMW was produced by Aberystwyth University in collaboration with solo earth observation (soloEO) It provides geospatial information about mangrove extent and changes.	https://data.une p- wcmc.org/datas ets/45

Construction of Random Forest Model

The approach used in the current study follows that of Erika et al., (2020); Barenblitt and Fatoyinbo (2020b), where backscatter representative samples are collected for one land cover of interest. Supervised classification (random forest classification) involves the creation of training samples (Figure 5) to train the classifier (Pelletier et al., 2016; Shelestov et al., 2017). Training and

validation data for this work is based on field campaigns conducted between December 2020 and April 2021. The global mangrove distribution vector (Table 7) was also needed as reference data to guide the creation of training samples.
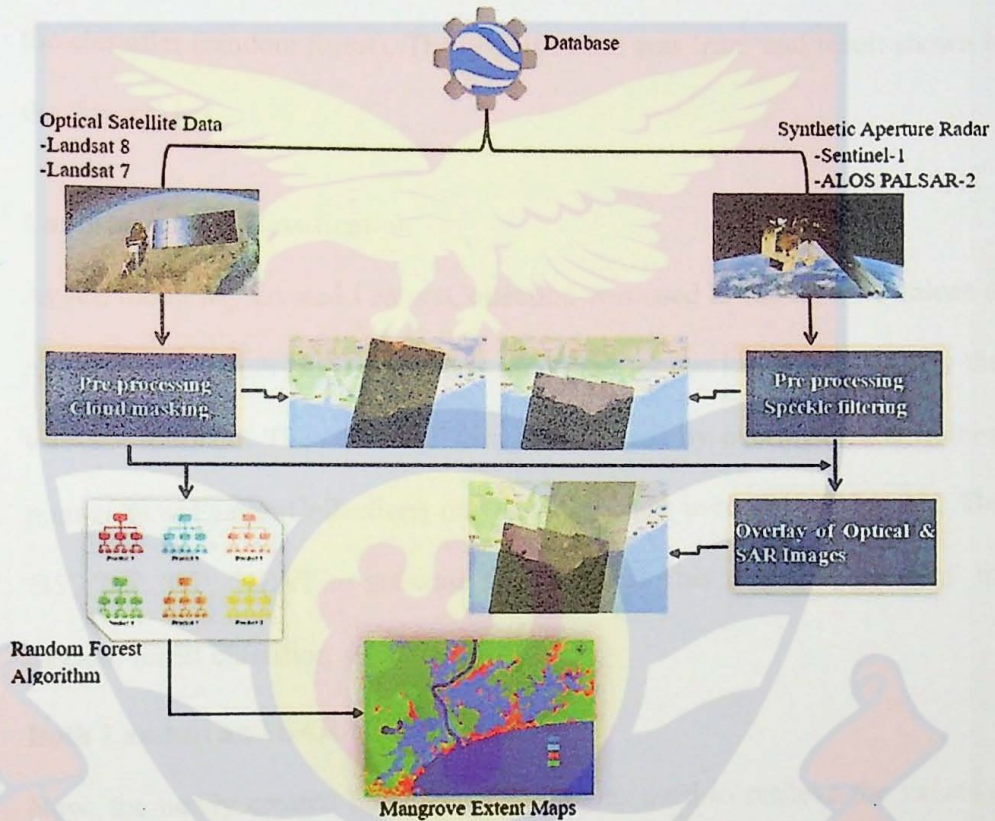
Figure 5: *Flowchart of Data Extraction and Random Forest Model*

SAR Classification

The speckle-filtered VH image was displayed and a polygon symbol was selected from geometry import box close to the drawing tool to add training data. Each newly created layer, e.g., open water, represents a class in the training data and was stored as a FeatureCollection named Landcover. Four different land cover classes were selected for: open water, mangroves, other vegetation/wetlands and bare land. The defined classes were merged to get a single collection here referred to as 'new FeatureCollection'.

67

The newly created FeatureCollection was used to retrieve the values of backscatter for each identified land cover for the Sentinel-1. The Sentinel-1 (SAR) image was defined and the training points were used to create the 'training' data (new FeatureCollection). This creates a 'training point' statistics based on the classes (new FeatureCollection) and was used to 'train' the classifier (random forest). The classification was 'run' and result shown in the 'layers' bar.

Landsat Image Classification

Again, the newly created FeatureCollection was used to retrieve the values of reflectance for each land cover class identified for the Landsat 8 imagery that was also defined. The 'training' data was created by overlaying the training points (new FeatureCollection) on the image and used 'B1', 'B2', 'B3', 'B4', 'B5', 'B6', 'B7', 'NDVI' to generate the statistics. This was used to 'train' the random forest classifier.

Both Landsat and SAR Classification

Now, the newly created FeatureCollection was used to retrieve the values of backscatter for each land cover class selected for both Landsat 8 and Sentinel-1 imagery. Both the optical and SAR images were defined and the training data were obtained by overlaying the training points on the defined image as shown in Figure 8. This was used to train the classifier (random forest). The classification was 'run' and the result shown in the 'layers' bar.

Comparison of Time Series

The processes described above were repeated using PALSAR-2 imagery (2009 imagery) and Landsat 7 imagery (2009 imagery). The mangrove

changes for the two time periods were calculated for each scenario using a function called 'reduce region' and the values were converted to hectares (Barenblitt and Fatoyinbo, 2020b).

Independent Assessment of Classification Accuracy

Overall, 1553 training sample points were created using stratified random sampling technique (Figure 7-9). The classification accuracy was evaluated using an error matrix according to the classifier. The training samples were divided randomly, using 1232 points (80%) to train the model and 321 points (20%) for validation. This eliminates systematic errors resulting from using the same sample points to training and validation (Pimple et al., 2018). The output of the stratified random sample points was exported to Google Drive and used to perform accuracy assessment independently in QGIS using the method described by Barenblitt and Fatoyinbo (2020b). This method involves using high-resolution satellite imagery available in QGIS to validate each point.
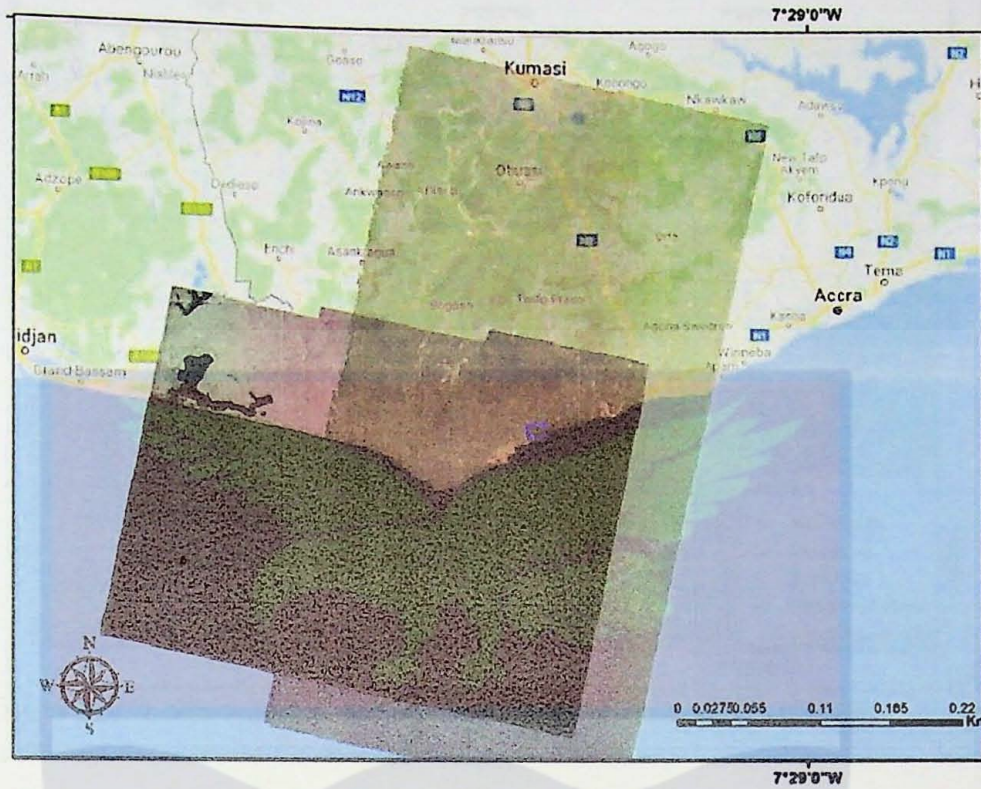
Figure 6: Optical and synthetic aperture radar image overlay
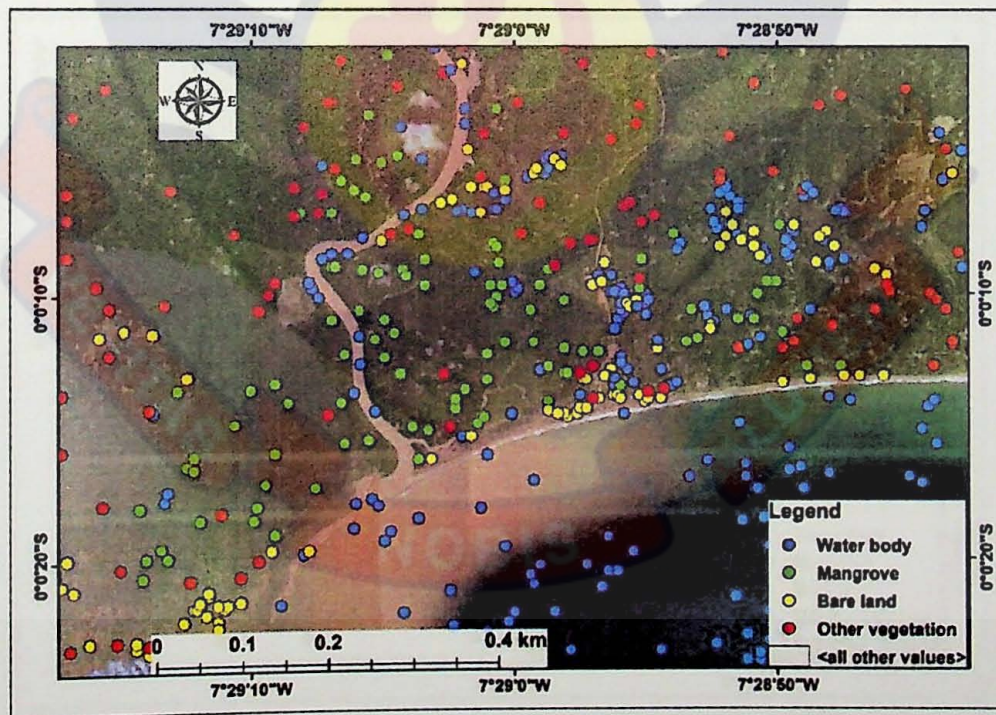
Figure 7: Independent Accuracy Assessment for the year 2019, Independent Accuracy Assessment for Landsat 8 Image

70
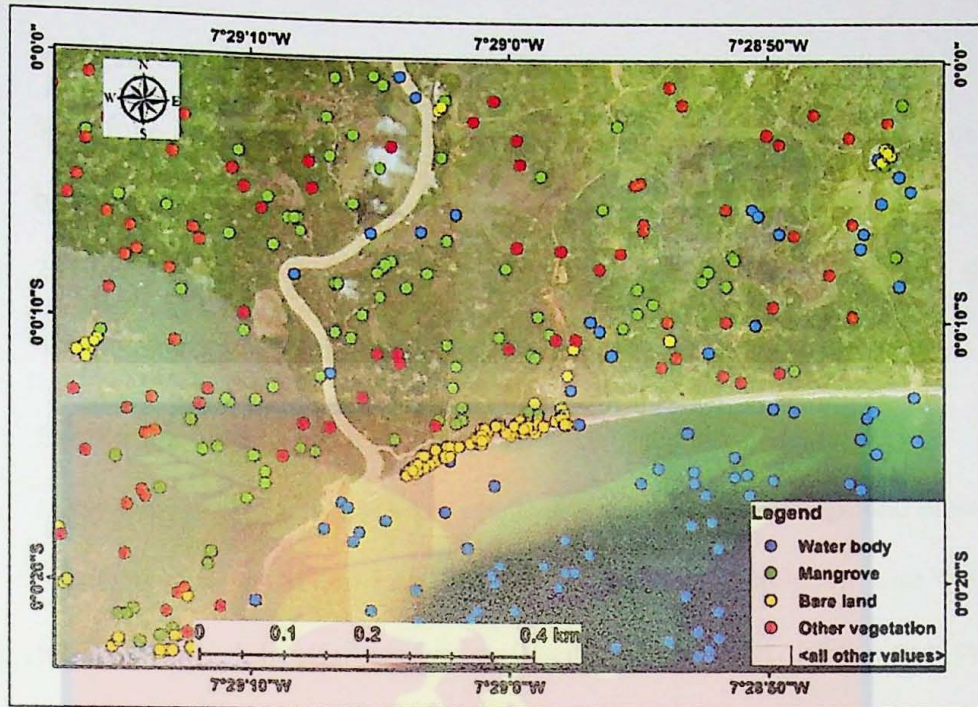
Figure 30: Independent Accuracy Assessment for the year 2019, Independent Accuracy Assessment for Sentinel-1 Image
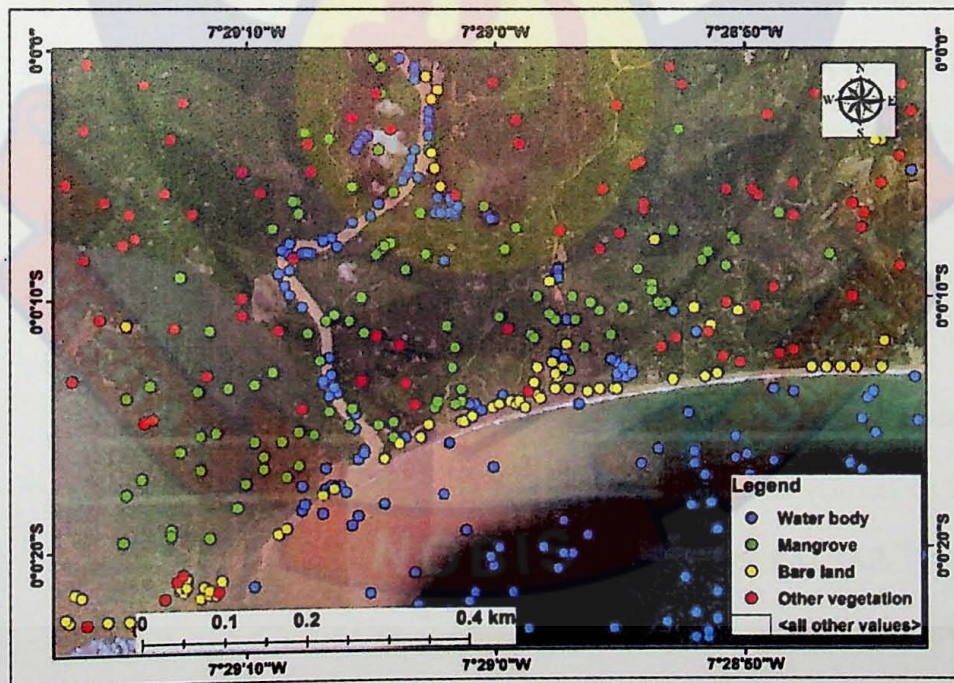
Figure 31: Independent Accuracy Assessment for the year 2019, Independent Accuracy Assessment for both Sentinel-1 and Landsat 8

Mangrove Structural Assessment

Mangrove above ground biomass (AGB) as at year 2000 was estimated using basal area weighted height estimates from the SRTM DEM (Simard et al., 2019). The AGB estimates from satellite was compared with field measurements to examine the temporal and spatial variation over time.

Estimation of Mangrove Stand Height

Mangrove canopy height is a key element in calculating aboveground biomass and carbon sequestration rates since it has a strong correlation with carbon turnover through litterfall production (Saenger & Snedaker, 1993; Rovai et al., 2016). In this study, Mangrove canopy height estimate was done using SRTM digital elevation measurement (Farr et al., 2007) generated in February 2000. Mangrove height estimation was done following an approach that had had been effectively applied at regional scales (Simard et al., 2008; Simard et al., 2006; Fatoyinbo & Simard, 2013). The SRTM DEM values represent a height that lies between the elevation of the ground and the canopy's highest point (aka Lorey's height) (Simard et al., 2008; Simard et al., 2006; Lagomasino et al., 2016). The maximum height is estimated to be 1.697 X (times) this value based on empirical data from field measurements (Simard et al., 2019). We used the global mangrove distribution vector to isolate mangrove areas and mask non-mangrove regions in the SRTM elevation data set (Giri et al., 2011). To estimate mangrove height, the SAR image (ALOS PALSAR-1) and the SRTM elevation model were clipped to the global mangrove distribution vector file (Figure 2). This extracts the backscatter values for the areas where the baseline mangrove vector indicates that there are mangroves. These values and the SRTM elevation were used to estimate the maximum canopy height

72

using a regression model that relates SRTM elevation measurements to maximum canopy height as described by Simard et al. (2019).

$$\text{SRTM } H_{max} = 1.697 \times H_{SRTM} \dots\dots\dots\dots\dots\dots\dots\dots\dots\dots\dots 2$$

where H_{SRTM} is the original DEM, and SRTM H_{max} is the new canopy height data set.

Estimation of Mangrove Above Ground Biomass

Once mangrove canopy height is established, estimates of above-ground biomass (AGB) can be generated from tree size and tree height components using allometric equations (Comley & McGuinness, 2005). The AGB of the mangrove forest in this study was estimated based on the relationship between mangrove biomass and canopy height (Simard et al., 2019; Lucas et al., 2014). The general equation that relates SRTM to canopy height and aboveground biomass is as follows:

$$\text{Aboveground Biomass (B)} = 3.25 \times H_{ba}^{1.53} \dots\dots\dots\dots\dots\dots\dots 3$$

Where, weighted height of basal area (H_{ba}) ~ 1.08*SRTM

Field Data Collection

Mangrove inventory involves either direct measurements of the biomass through destructive harvesting of specific trees, or indirect calculation from measurements of tree sizes and inferences using allometric equations (Chave et al., 2005; Keller et al., 2001). While the destructive method involves cutting down the trees, the non-destructive method relies on an allometric equation (Gibbs et al., 2007). Allometric formulars are gotten from various physical tree parameters such as DBH, height, crown diameter, etc. (Vashum &

73

Figure 32: Laying of Transect during Field Work

Figure 33: Mangrove Height Measurement during Field Work

Jayakumar, 2012). This method is used to evaluate biomass and carbon stock of trees without felling them. However, allometric equations are often site and species dependent. A universal allometric relationship described by Komiyama et al. (2005) is generally recommended for calculating above ground mangrove biomass on-site. This allometric equation is used in the current study to calculate above ground biomass for a number of individual trees in sample quadrants. The total biomass of the plot was gotten from the addition of all biomass values of each quadrant along the transect. The biomass was then expressed in milligram per hectare (mg/ha).

For this study, ground-based mangrove inventory data was collected using indirect estimation and systematic random sampling designs. Field surveys were conducted from December 2020 to April 2021 (Figure 12-14). In order to survey the mangroves, a 100-meter transect was created perpendicular to the shoreline using measuring tape. For sampling, four distinct 5 m × 5 m quadrants were set up 25 m apart. Four different 5m x 5m quadrants were set up for sampling, spaced 25m apart. Sampling points coordinates were recorded with a Garmin 64s GPS to capture specific areas in the field. The height and diameter measurements (DBH) were carried out for all mangrove species above 2m in all quadrants during the course of the field surveys. A calibrated long pole was used to measure the heights of each tree species. DBH was captured with Electronic Digital Calipers.

Site specific allometric equations are rare for mangrove, and thus universal equations are most frequently used. For this study, AGB was estimated using two different universal allometric equations (Chave et al., 2005; Komiyama et

75

al., 2005) and a regional allometric equation (Njana et al., 2015) which were developed specifically for mangrove since there is no published allometry for the study site. These allometries were chosen because they are primarily dependent on wood density and height. The universal pantropic equation by Komiyama et al. (2005) is given below:

$$AGB = 0.251 \, \rho \, D^{2.46} \quad \text{...} \quad (4)$$

Where,

AGB = above ground biomass (kg/tree), ρ = wood density (g cm^{-3}) and D = DBH (cm). This equation has a standard error of 8.5% (Komiyama et al., 2005; Fatoyinbo et al., 2018).

The universal model by Chave et al. (2005) for mangrove forests is given by equation (5):

$$AGB = 0.0509 \, \rho \, D^2 \, H \quad \text{...} \quad (5)$$

Where,

AGB = above ground biomass (kg/tree), ρ = wood density (g cm^{-3}) and D = DBH (cm) and H = height (m). This model integrates tree height information to reduce the standard error.

Another allometric equation which integrates height, DBH and wood density is given by Njana et al (2015) equation:

$$AGB = 0.353 \, \rho^{1.13} \, D^{2.08} \, H^{0.29} \quad \text{...} \quad (6)$$

Where,

AGB = above ground biomass (kg/tree), ρ = wood density (g cm^{-3}) and D = DBH (cm) and H = height (m).

These models were developed to estimate biomass of *Avicennia* and *Rhizophora* species which are also indigenous mangrove species in the study area. Wood density used in this study is from the World Agroforestry Wood Density Database as reported by Muhd-Ekhzarizal et al. (2017) and Fatoyinbo et al. (2018). Since the wood densities are not specific to Ghana, average value of 0.87 was used (Table 10).
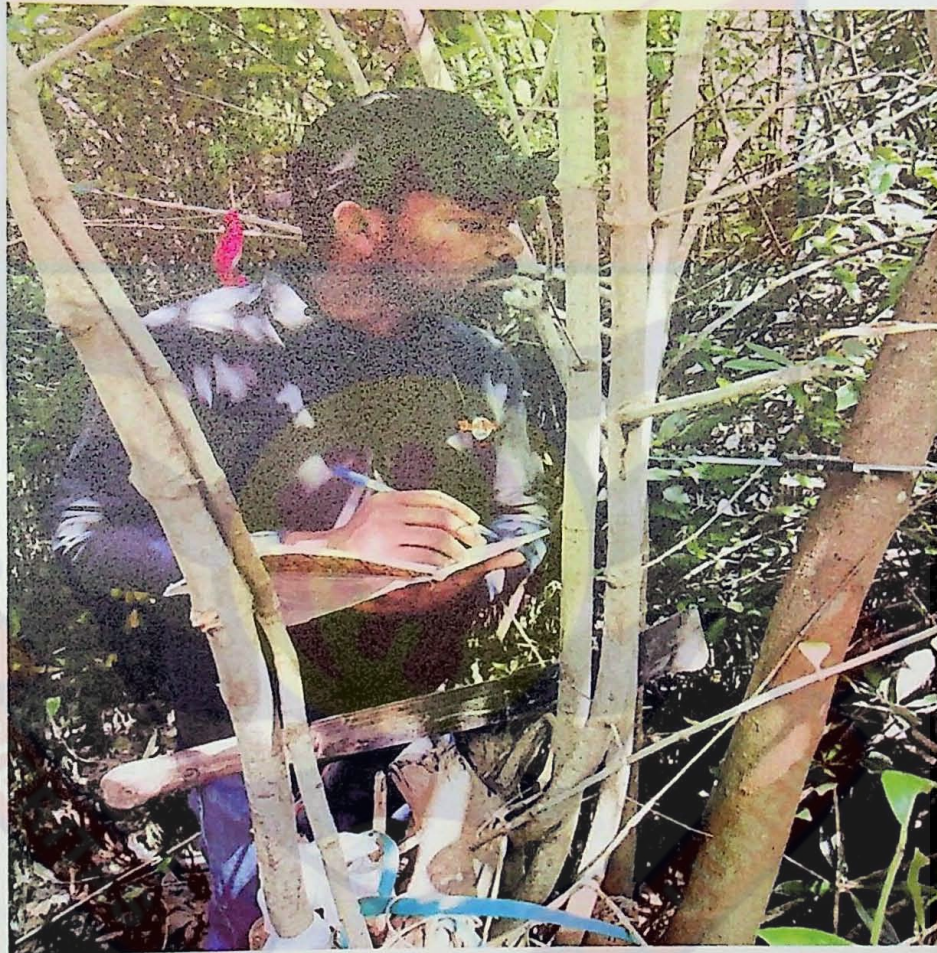
Figure 34: DBH Measurement During Field Work

77

Table 8: Wood density for mangrove species

Mangrove Type	Density (g cm^{-3})		
	Low	Mid	High
Avicennia marina	0.79	0.81	0.85
Bruguiera gymnorrhiza	0.63	0.84	1.05
Ceriops tagal	0.87	0.97	1.09
Heriteria littoralis	0.83	0.98	1.23
Lumnitzera racemosa	0.75	0.88	0.97
Rhizophora mucronata	0.94	1.02	1.12
Sonneratia alba	0.62	0.78	1.00
Xylocarpus granatum	0.59	0.70	0.83

Source: World agroforestry wood density database cited in Fatoyinbo *et al.* (2018)

Hydrodynamic and Morpho-dynamic Modeling

The general flowchart for conducting numerical modeling is shown in Figure 15. The planning phase includes meetings with supervisors to review the modeling objectives and key features that govern circulation and sedimentation in the study area.

78

```
┌─────────────────┐
│  Planning Stage │
└─────────────────┘
         │
         ▼
┌──────────────────────────────┐
│ Data Acquisition and preparation │
└──────────────────────────────┘
         │
         ▼
┌─────────────────┐
│   Model Setup   │
└─────────────────┘
```
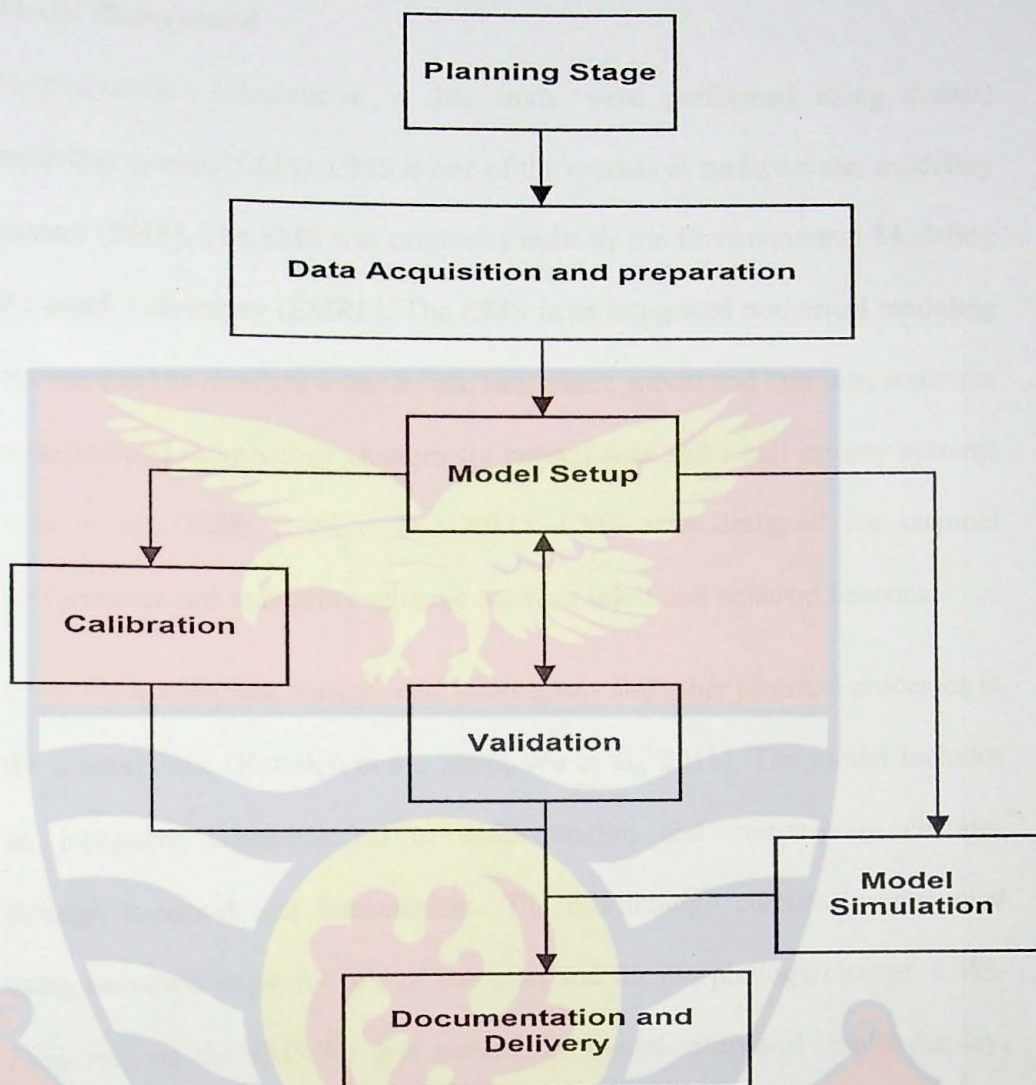
Figure 35: Overview of the General Modeling Steps

The data acquisition and processing were carried out. The main data for this study includes: bathymetry, shoreline profile, digital elevation model and sediment properties in the study area. A Google Earth image covering the entire study site was extracted and corrected, yielding structure and shoreline locations. All data collected provided enough information for the description of the physical processes going on in the study area and provided a strong basis for the configuration and calibration/validation of the CMS as outlined in the sections below.

79

Model Background

Hydrodynamic calculations in this study were performed using coastal modeling system (CMS). CMS is one of the models in surface water modeling system (SMS). The SMS was originally built by the Environmental Modeling Research Laboratory (EMRL). The CMS is an integrated numerical modeling system used to simulate water levels, near-shore waves and currents, sediment transport and morphology changes for coastal seas and small estuary systems (Lin et al., 2008; Reed et al., 2011). CMS was designed for channel performance and sediment exchange between inlets and adjacent beaches.

CMS-Flow computes currents and water levels and other physical processes in the coastal zone (Buttolph et al., 2006; Wu et al., 2011). The model includes an integrated representation of sedimentation and morphology changes through transport rate formulations. The morphology change is calculated using two-time steps, for rate of transport and for morphology change. CMS-Flow rely on the SMS for grid generation, model setup and results display. Classic applications of CMS-Flow involve analysis of both past, present and future performance of navigation channels; wave and current interactions in canals and near shipbuilding structures; and transport problems of sediment management within coastal inlets and surrounding beaches.

Underlying Equations and Numerical Principles

CMS Flow model uses 2D finite volume to solve the shallow water equation of conservation of mass and momentum. The relevant equations are resolved on a quadtree grid by means of a completely implicit finite volume technique. Finite volume method is based on the truth that many natural laws are similar

80

to the principles of conservation of momentum and mass. From this notion, the method develops a formulation comprising conservation of flow equations defined in an averaged sense over the grid cells. The strength of the finite volume technique is that it performs only flow evaluations for the element boundaries. This advantage also applies to non-linear problems, making the method robust for non-linear conservation laws usually encountered in sediment transport or water quality.

The general equations of mass and momentum conservation may be written as:

$$\frac{\partial h}{\partial t} + \frac{\partial (hu_j)}{\partial x_j} = 0 \dots\dots\dots\dots\dots\dots\dots\dots\dots\dots\dots\dots\dots\dots\dots\dots\dots\dots\dots\dots .7$$

$$\frac{\partial (hu_i)}{\partial t} + \frac{\partial (hu_i u_j)}{\partial x_j} - \varepsilon_{ij} f_c hu_j = -gh\frac{\partial \bar{\eta}}{\partial x_i} + \frac{\partial}{\partial x_j}\left(v_t h\frac{\partial u_i}{\partial x_j}\right) - \frac{1}{\rho}\frac{\partial}{\partial x_j}\left(S_{ij} + R_{ij}\right) -$$

$$m_b \frac{\tau_{bi}}{\rho} \dots\dots\dots\dots\dots\dots\dots\dots\dots\dots\dots\dots\dots\dots\dots\dots\dots\dots\dots .8$$

where

t = time (s), h = water depth (m), u_i = current velocity (m/s), f_c = Coriolis parameter (rad/s). ε_{ij} = 1, for $i = 1, j = 2$, ε_{ij} = -1, for $i = 2, j = 1$, and ε_{ij} = 0, otherwise, ρ = sea water density (~1025 kg/m^3); g = gravitational constant (~9.81 m/s^2), v_t = horizontal turbulent eddy viscosity (m^2/s), τ_{bi} = wave-averaged bed shear stress (Pa), m_b = bed slope coefficient, S_{ij} = wave radiation stress (Pa m), and R_{ij} = surface roller stress (Pa m). NB the full mathematical derivations of these equations are beyond the scope of this study.

Sediment Transport Formula

In CMS, sediment transport is modeled using the total load sedimentation equation (Sánchez & Wu, 2011):

$$\frac{\partial}{\partial t}\left(\frac{hC_t}{\beta_t}\right) + \frac{\partial(hU_jC_t)}{\partial x_j} = \frac{\partial}{\partial x_j}\left[V_s h \frac{\partial(r_sC_t)}{\partial x_j}\right] + \alpha_t\omega_s(C_{t*} - C_t)\dots\dots\dots\dots\dots\dots.9$$

where C_t = concentration of total load (kg/m^3), C_{t*} = concentration of total load equilibrium (kg/m^3), α_t = coefficient of total load adaptation, V_s = coefficient of sediment mixing (m^2/s), ω_s = velocity of sediment fall (m/s), r_s = suspended sediments fraction, and β_t = factor of total load correction.

The coefficient of total load adaptation is calculated as:

$$\alpha_t = \frac{Uh}{(L_t\omega_s)}\dots\dots\dots\dots\dots\dots\dots\dots\dots\dots\dots\dots\dots\dots.10$$

Where

L_t = the length of total load adaptation (m)

The bed change formular is as follows:

$$\rho_s(1 - \acute{p}_m)\frac{\partial z_b}{\partial t} = \alpha_t\omega_s(C_{t*} - C_t) + \frac{\partial}{\partial x_j}\left(D_s q_b \frac{\partial z_b}{\partial x_j}\right)\dots\dots\dots\dots\dots.11$$

Where

ρ_s = sediment density (kg/m^3), $\acute{p}_m$ = bed porosity, z_b = bed elevation(m), D_s = coefficient of empirical bed slope (constant), q_b = rate of transport of bed load mass (kg/m/s) (Sánchez et al., 2014).

Model Assumptions

George E. P. Box is known with saying that all models are wrong: some models are useful. This statement denotes that a model is only an abstraction of reality. Two dimensional models have been defined by scientists and

82

engineers with certain assumptions to enable mathematical solutions. These assumptions and its understanding allow the modeler to determine the suitability of a model to a specific scenario or set of conditions. If the physical phenomenon represented by the model do not match with the model formulation assumptions, the model is incorrect and less suitable. Here is a general numerical assumption: the calculation of hydrodynamics and sedimentation relies on the assumption of a constant bed topography and only the rate of sedimentation or erosion for this topography is calculated at each location.

Data Collection for Setting-Up and Parameterization of the Model

Data for the preliminary model construction, calibration, and prediction for this study was collected from December 2020 to May 2021. The field campaign followed the method described by Jose et al. (2017) and consisted of general identification of landforms of the study area, identification of dominant plant species, determination of in situ biomass density, measurements of critical hydraulic controls, retrieval of tidal gauge data (surface water level) and bathymetry. Figure 16 shows the overview of the approach as used in this study. The data requirements for this study are as presented in Table 9.

83
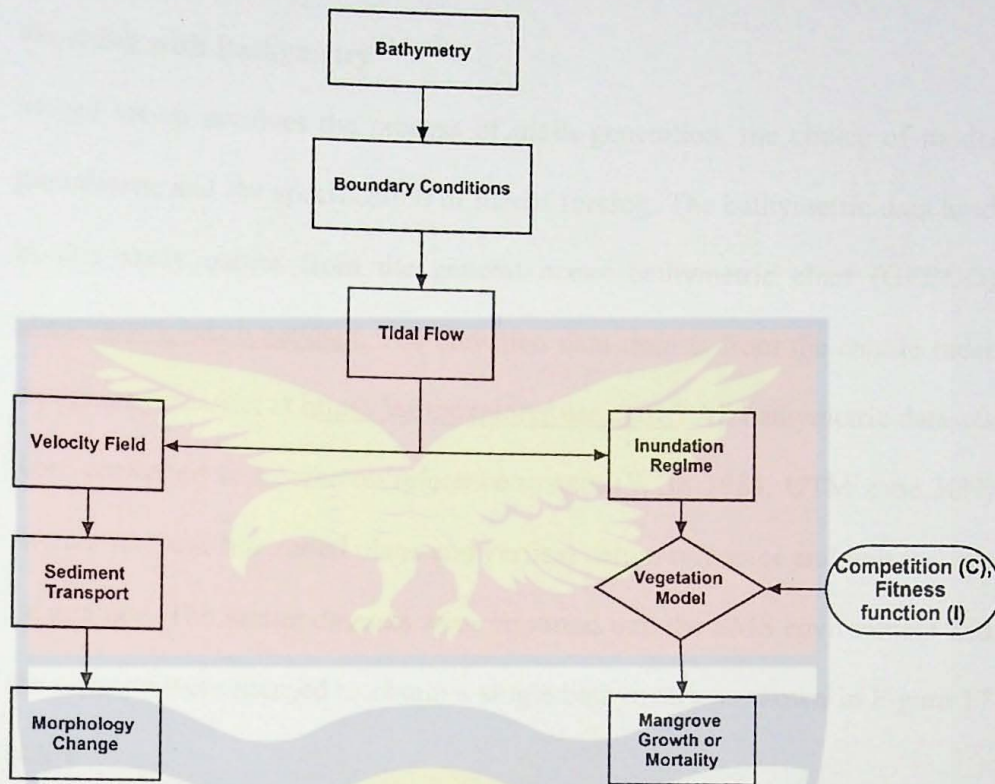
Figure 36: Overview of bio-morpho-feedback interactions incorporated into
the model

Required Data and Sources

Table 9: Required Data and Sources for Hydro-dynamic Simulation

S/N	Data Type	Source
1	Topographic data	USGS SRTM DEM https://earthexplorer.usgs.gov/
2	Bathymetric data	GEBCO https://www.gebco.net/data
3	Land cover data and Shoreline profile	USGS Website/Google Earth https://earthexplorer.usgs.gov/
4	Water level measurements	Gaging Station/ Copernicus Marine and ESA/CCI Product CMEMS
5	Biomass Density and Mangrove stand height	Field work
6	GPS Coordinates	Field work

Model Setup and Calibration

Working with Bathymetry

Model set-up involves the process of mesh generation, the choice of model parameters, and the specification of model forcing. The bathymetric data used in this study comes from the general ocean bathymetric chart (GEBCO) https://www.gebco.net/data. The elevation data used is from the shuttle radar topography mission at https://earthexplorer.usgs.gov/. All bathymetric datasets were converted to a common reference system (WGS 1984, UTM zone 30N) so that the same horizontal plane and vertical datum reference and unit (m) are maintained. The scatter datasets were imported into the SMS environment and the datasets were merged to obtain a single bathymetry as shown in Figure 17 below.
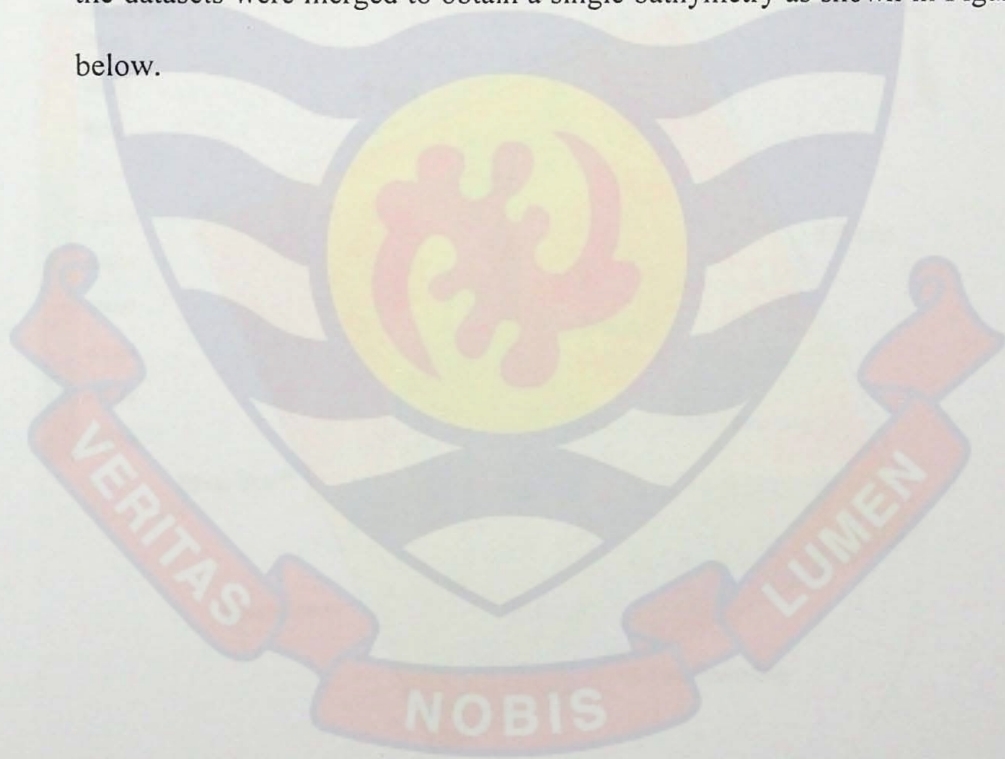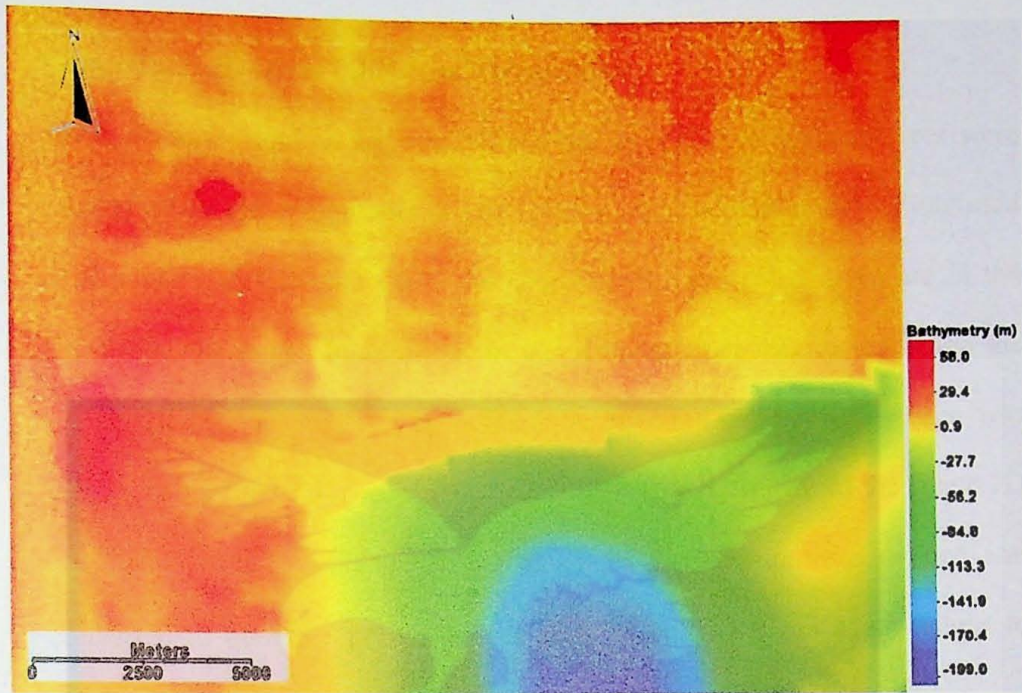
Figure 37: Merged Scatter Dataset (Bathymetric data)
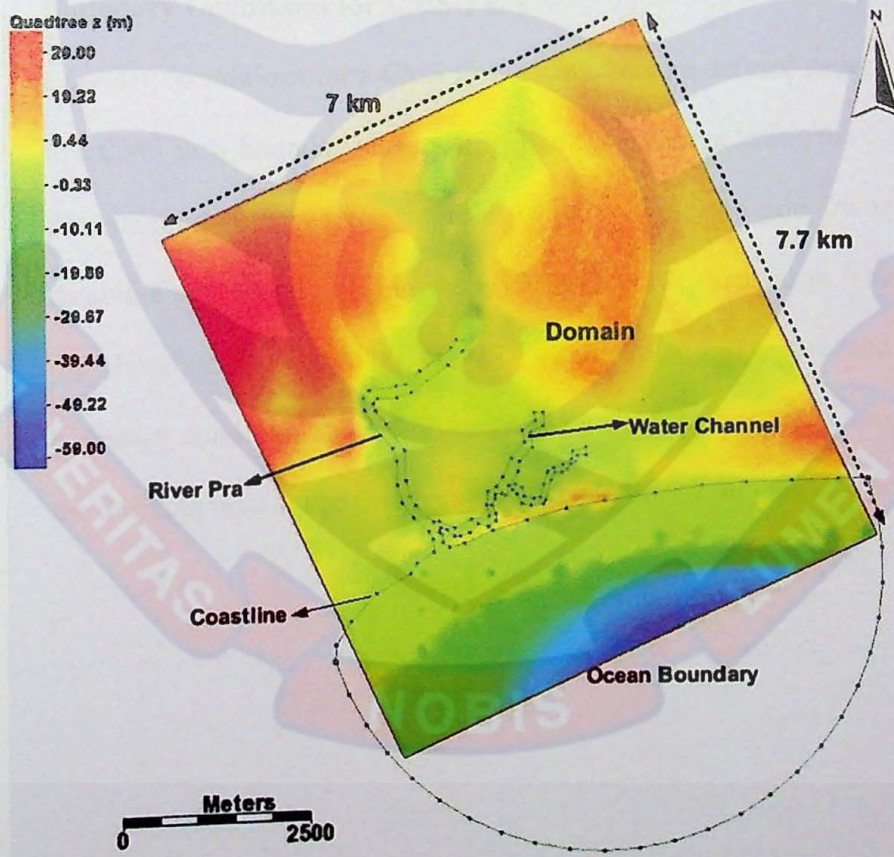
Figure 38: Quadtree Generator

86

Computational Grids (Quadtree Generation)

The bathymetry and an arc that defines the shoreline of the study area were used to create the computational grid (Figure 18). The bathymetry is imported as a scatter point dataset while the shoreline is represented as an arc in the CMS flow coverage. In addition, an elevation data set was included and the projection for the project was defined. A quadtree generator coverage was created and selected to become the active coverage. By means of the create 2D grid frame tool, the extent of the domain of computation was defined and converted to quadtree grids. This defines the cells, assigns depth values to each cell, and creates strings of cells around the boundaries.

Boundary Conditions for CMS-Flow

Boundary conditions for a CMS flow simulation are defined using feature arcs in a CMS flow boundary coverage. A boundary arc enclosing the ocean side of the quadtree grid was created from the top where the grid frame meets the shoreline arc, then following the grid frame border around to where it meets the shoreline arc again (Figure 17). Both the shoreline arc and the ocean boundary condition arc are unassigned by default. Boundary conditions and the defining tidal signals were assigned to the arc around the grid boundary.
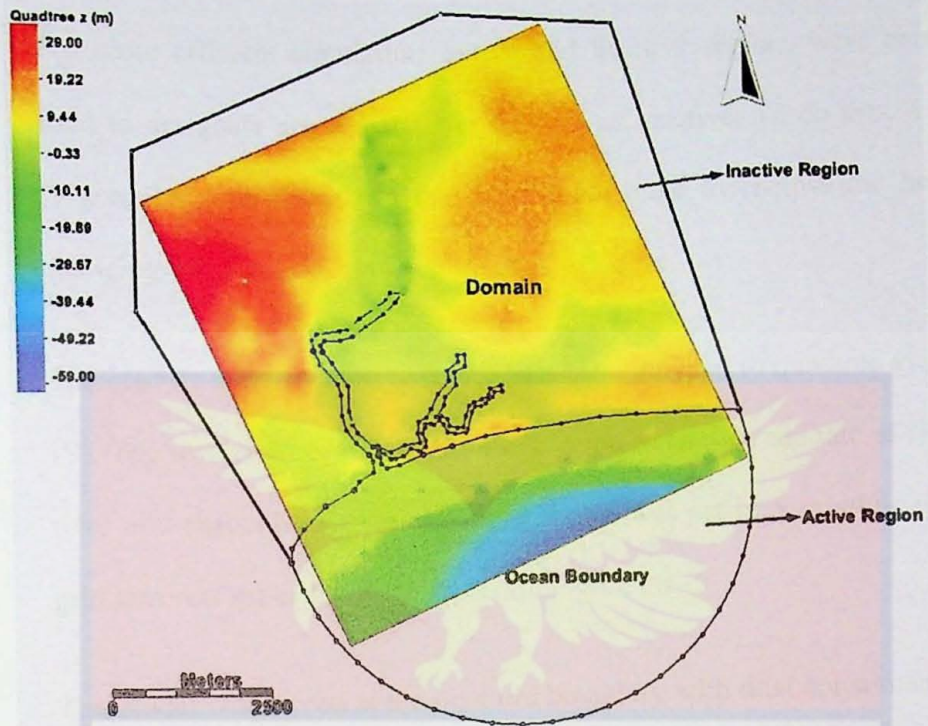
Figure 39: *Boundary Condition*
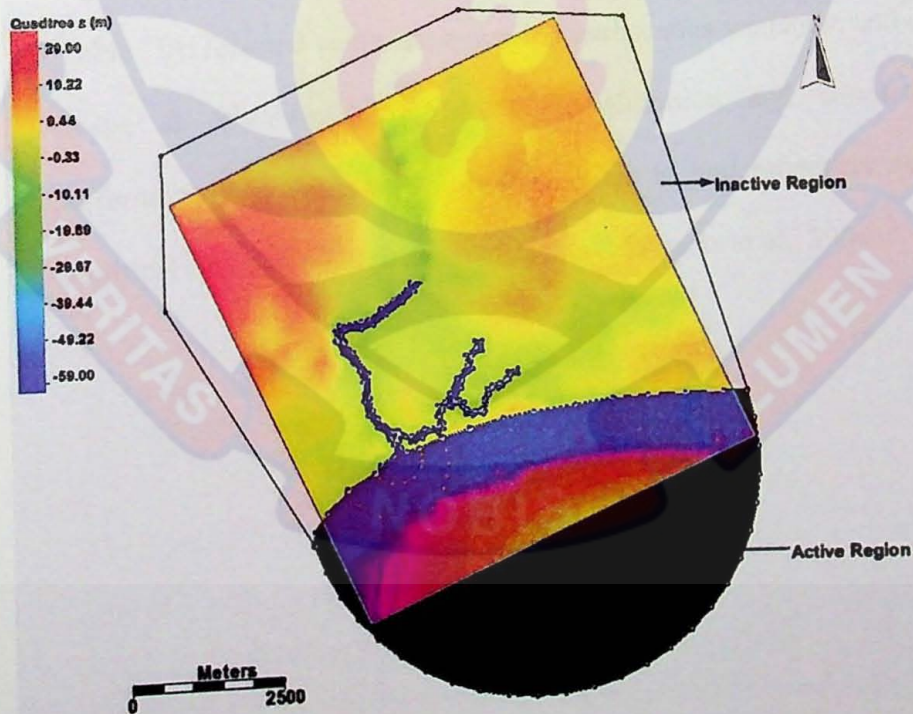
Figure 40: *Feature Polygon for Grid Generation*

88

For more efficient simulation, active and inactive regions were created and used to designate areas that never get wet as inactive. To do this, a polygon (Figure 18) was created in the activity coverage to enclose the land while changing the ocean region from inactive to active.

The activity classification coverage was then mapped to quadtree grid (Figure 19). The resolution of the grids was adjusted to capture the rate of flow in the river and channels. The minimum grid size was set to 5 m while the largest grid size was set to 160 m as shown in Figure 20.

The model was forced at the offshore boundary with tidal constituents and sea surface elevation generated using Copernicus Marine and the ESA/CCI product CMEMS (Figure 21). Manning roughness values were defined in the model based on the distribution of 3 classes of land cover exposed to tides (Table 10): forested wetlands; emerging herbaceous wetlands; and open water (Liège & Westerink, 2006). Model calibration and simulations were performed using these values as they relate to bed properties according to empirical data and numerical experiments (Mattocks et al., 2006).
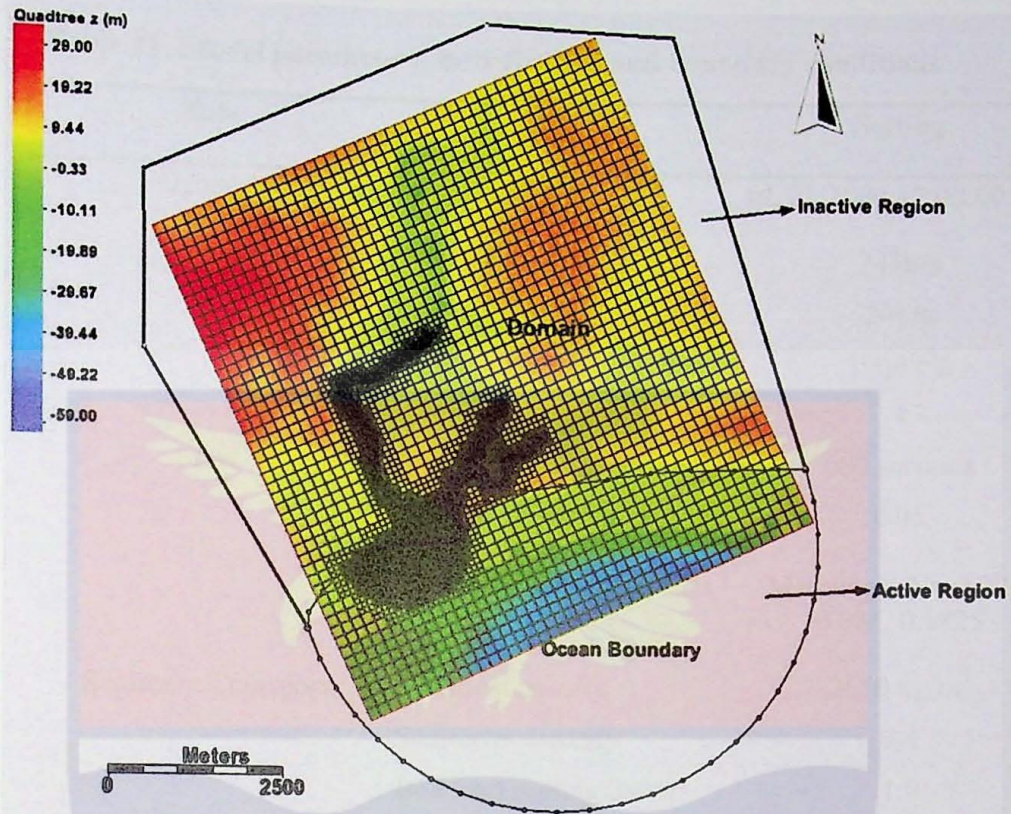
Figure 41: Quadtree Grid, Save Point and Grid Resolution Adjustment

Table 10: Manning Roughness Values for Different Surfaces

S/N	Land Cover Type	Manning roughness (n)
1	Built-up, open space	0.0404
2	Built-up, low intensity	0.0678
3	Built-up, medium intensity	0.0678
4	Built-up, high intensity	0.0404
5	Bare land	0.0113
6	Deciduous Forest	0.36
7	Evergreen Forest	0.32
8	Mixed Forest	0.40
9	herbaceous wetlands	0.1825
10	woody wetlands	0.086
11	open water	0.025

Source: Sánchez et al., 2011

90

Table 11: Model parameters, initialization and boundary conditions

Tab	Item	Setting
General	Start Date/Time	01/01/2000 12:00:00 am
	Simulation duration	744hrs
	Ramp duration	24hrs
	Solution Scheme	Implicit
	Number of threads	4
Flow	Hydro-dynamic time step	600 seconds
	Wetting and Drying depth	0.05
	Bottom Roughness Dataset	Manning's N= 0.025, 0.086, 0.1825
Sediment Transport	Sediment density	2650 kg/m^3
	Sediment porosity	0.4
	Bed load scaling factor	1.0
	Suspended load scaling factor	1.0
	Morphologic acceleration factor	100
	Bed slope diffusion coefficient	0.1
	Total load adaption length	10m
	Sediment size class diameter	0.26mm
	Minimum bed layer thickness	0.05m
	Maximum bed layer thickness	0.5m
Output	List1	[0][0.5][744]
	List2	[0][3][744]
	List3	[0][1][744]
	Water surface elevation	List1
	Current velocity	List1
	Morphology	[Checked]List2
	Transport	[Checked]List3

91

CMS Calibration and Simulation

A first step before the simulation of the hydrodynamics and morphodynamics was the calibration of the CMS model. The model calibration was performed using an established method, in which the most sensitive parameter (Manning's roughness) was manually adjusted. Manning roughness values were defined in the model based on the distribution of 3 classes of land cover exposed to tides (Table 10): woody wetlands; emerging herbaceous wetlands; and open water. Model calibration and simulations were performed using these values as they relate to bed properties based on empirical data and numerical experiments. Three different simulations of one month (one tidal cycle) were run with different values of Manning's roughness. The simulations aim to predict the influence of surface roughness on the ability of the model to calculate the water surface elevation. Simulated time series of water surface elevations were compared with measured water surface elevations. The goodness-of-fit statistics was used to assess model performance. The model was calibrated by comparing the simulated water surface-elevation results to gauge measurements, and the best fit was used for longer-term simulations. We calculated the goodness-of-fit statistics using the standard error of the estimate (Sy.x):

$$Sy.x = \sqrt{\frac{\sum(residuals^2)}{n-k}} \dots\dots\dots\dots\dots\dots\dots\dots\dots\dots\dots\dots\dots\dots\dots\dots\dots\dots 12$$

Where, n = number of values, k = number of parameters fit by regression.

The model parameters were specified as indicated in Table 11. The hydrodynamic model solves the shallow water equation and calculates the current velocities, the water surface-elevation and the morphology changes.

92

The model also calculates the relative hydroperiod, which was used in a vegetation model to study the potential impact of SLR on the mangrove ecosystem.

Sea Level Rise Scenarios

Imaginary open boundaries of CMS-Flow enable water exchange together with model-forcing, such as Water level variations. Fresh water inflows or water surface elevation can be specified along this boundary. Water level changes can be obtained from measurements of coastal tide gauges or composed of tidal constituents. In the CMS, the general formula for the water surface elevation (WSE) boundary is given by:

$$\tilde{\eta}_B = \tilde{\eta}_0 + \tilde{\eta}_E + \Delta\tilde{\eta} \dots\dots\dots\dots\dots\dots\dots\dots\dots\dots\dots\dots\dots\dots\dots\dots\dots\ 13$$

Where

$\tilde{\eta}_B$ = boundary water surface elevation, $\tilde{\eta}_0$ = initial boundary water surface elevation, $\tilde{\eta}_E$ = specified external boundary water surface elevation, and $\Delta\tilde{\eta}$ = water surface elevation off-set. The variables are measured in meter.

Longer term Simulation and Incorporation of Sea Level Rise Scenarios

For this study, sea level rise (SLC) curve scenarios were used to simulate the effects of sea level changes (Figure 21). Sea level rise forecasts based on various socioeconomic scenarios are the subject of periodic assessment reports from the Intergovernmental Panel on Climate Change (IPCC, 21). The National Oceanic and Atmospheric Administration (NOAA) created a web-based tool to determine worldwide future SLR rates based on the most recent IPCC forecasts and accounting for local land subsidence (Li & Brown, 2019). The SLR curves were obtained for the global ocean and were specified in the

93

assign boundary conditions section of the SMS interface. Since there is currently no local SLR projection, it is appropriate to apply global SLR scenarios in the study region.

The CMS model was run with different SLC scenarios to simulate the influence of SLR projections on the hydro- and morpho-dynamics of the area. Each simulation utilized one of three SLR scenarios for the 2100 projection, which included a low scenario (0.3 m), an extremely high scenario (2.5 m) and no sea level rise (constant) scenario.

The total simulation time was set to 31 days (corresponding to a complete tidal cycle) and a morphological acceleration factor of 100 was specified in the model control, which makes it equivalent to 100 tidal cycles (~8.4 years) condition (Styles et al., 2018). Process-based morpho-dynamic models such as CMS require enormous computing time for simulations. The morphological acceleration factor is therefore a valuable tool available in CMS to minimize simulation time (Lesser et al., 2004).
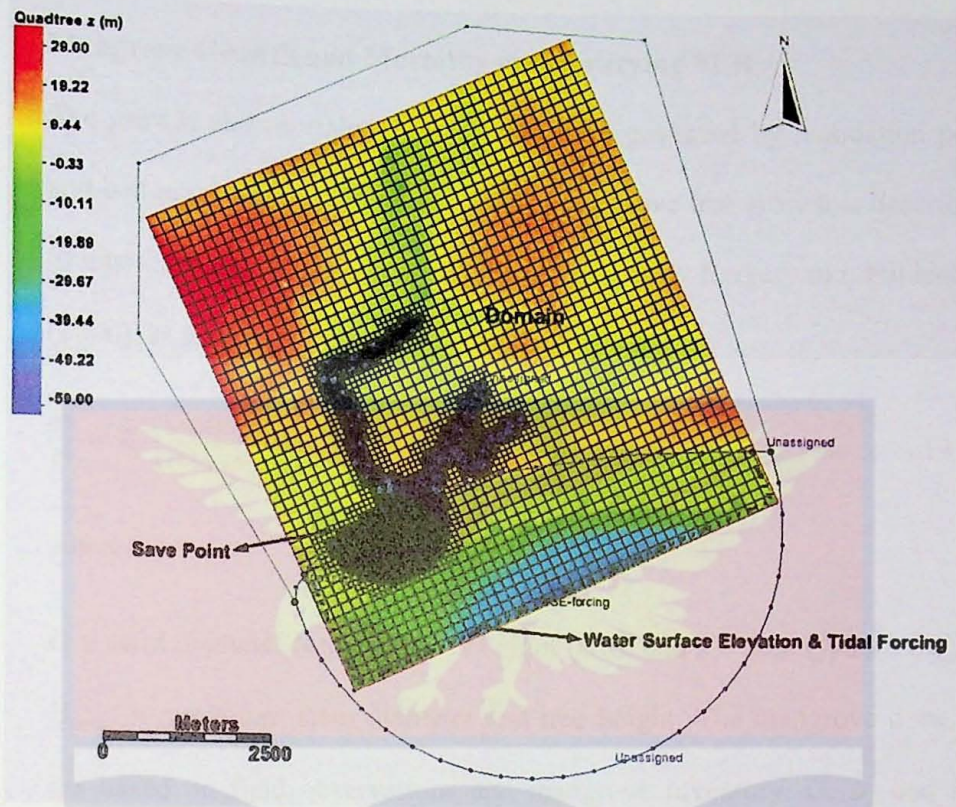
Figure 42: Model Control and Parameterization
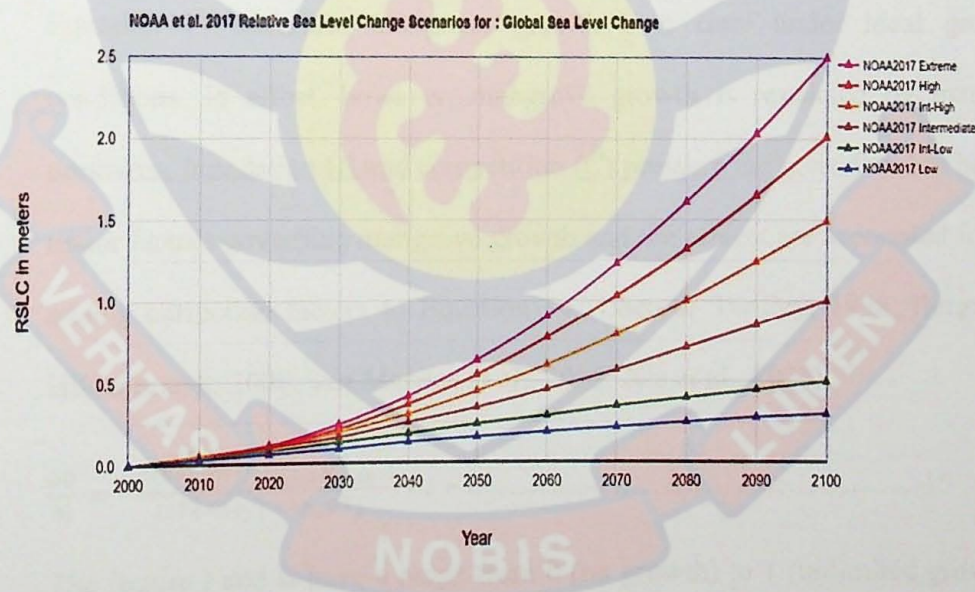
Figure 43: Sea level Rise Scenarios from Year 2000 - 2100

95

Mangrove Growth and Mortality under varying SLR

The growth and mortality of mangroves are governed by inundation periods and bed elevation (Krauss et al., 2008). Mangrove tree growth is described by Shugart (1984), Chen and Twilley (1998) and Berger and Hildenbrandt (2000), as follows:

$$\frac{\partial D}{\partial t} = \frac{GD(1-(DH)/(D_{max}H_{max}))}{(274+3b_2D-4b_3D^2)} \dotfill 14$$

where

D = stem diameter (cm), H = tree height (cm), and t = time (years). D_{max} and H_{max} = maximum stem diameter and tree height. The mangrove dimensions are based on field observations and mangrove inventory. G, b_2 and b_3 are growth parameters (van Maanen et al., 2015).

Equation 14 describes mangrove growth over time under ideal growth conditions. In effect, however, mangrove growth is restricted by external pressures. Inundation (I) and competition (C) pressure are considered to be the major factors governing mangrove growth and the effects are accounted for by adding correction factors to Equation 14 (Chen & Twilley, 1998; Berger & Hildenbrandt, 2000; van Maanen et al., 2015; Xie et al., 2020):

$$\frac{\partial D}{\partial t} = \frac{GD(1-(DH)/(D_{max}H_{max}))}{(274+3b_2D-4b_3D^2)} * I * C \dotfill 15$$

The factors I and C have a range from 0 (no growth) to 1 (unlimited growth). The inundation (I) depends on the hydroperiod and it is assumed that there is an optimal inundation regime where the rate of growth is highest ($I = 1$), with reduced growth rates ($I < 1$) when the mangroves are submerged for either longer or shorter periods (van Maanen et al., 2015). The growth and

96

development of the mangrove trees are therefore dependent on the regime of inundation and the bed elevation. This type of mangrove growth rate response to inundation has been previously demonstrated by Krauss et al. (2008). Competition between trees affects growth based on nutrient availability. The correction factor for competition (C) is thus a function of the mangrove trees biomass (van Maanen et al., 2015). Mangrove begins to die after prolonged periods of growth suppression due to external factors (Berger & Hildenbrandt, 2000). So, if $I = 1$ and $C = 1$, then tree growth is finest; while lower values mean tree growth is limited by flood stress and competition. If the product I*C in Equation (15) is below 0.5 for the period under consideration, mangrove density practically decreases (van Maanen et al., 2015; Xie et al., 2020).

$$I = a * p^2 + b * p + c \dots\dots\dots\dots\dots\dots\dots\dots\dots\dots\dots\dots 16$$

where p represents the relative hydroperiod (T(inundated)/T(tide)) and a, b, and c are constants which were set to -16, 16, and -3 (Appendix 1).

Equation (15) suggests that there is a maximum growth rate for a given hydroperiod. The assumption is that there is an ideal inondation regime when the growth rate is maximal ($I = 1$), with reduced rates of growth ($I < 1$) when the mangroves are inondated for either shorter or longer periods (van Maanen et al., 2015). The values of a, b and c were chosen such that $I = 1$ when the mangroves are flooded half the time ($p = 0.5$) (Xie et al., 2020).

$$C = \frac{1}{1+exp[d(B_{0.5}-B)]} \dots\dots\dots\dots\dots\dots\dots\dots\dots\dots\dots\dots\dots\dots\dots\dots 17$$

where

d is a constant = -0.00005 and $B_{0.5}$ is the value of B for which $C = 0.5$ and it is ~ 1.04·105 kg/ha

In this study, CMS was used to simulate the relative hydroperiod for different sea-level rise scenarios which was fed into the dynamic vegetation model to calculate inundation regime as well as competition stress, to give insight into mangrove response to hydro- and morphodynamics triggered by SLR. The relative hydroperiods were used in Equation 16 to calculate the inundation stress (I) and then Equation 17 was used to calculate the competition factor (C) based on the mangrove biomass density from the field work.
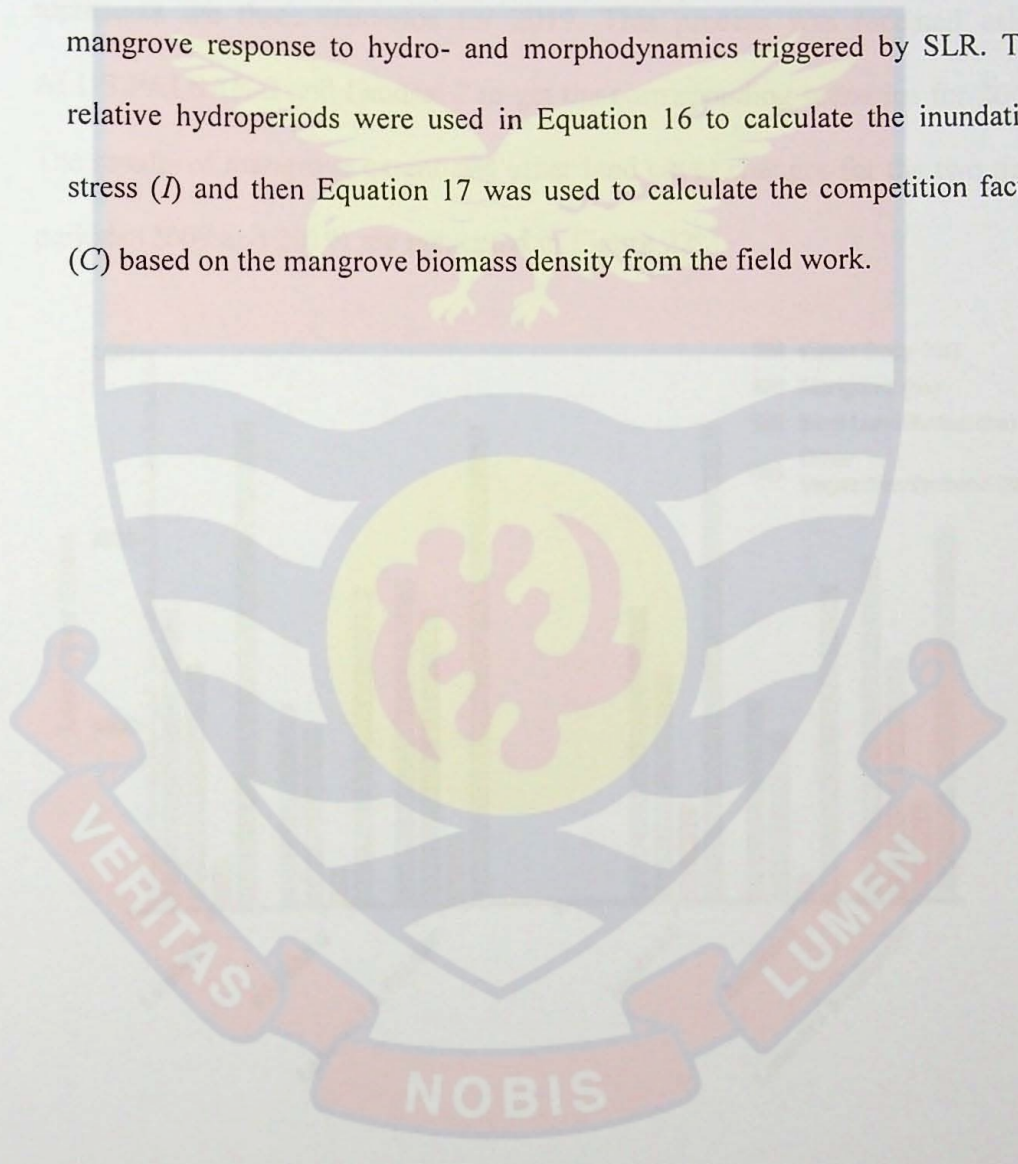
CHAPTER FOUR

RESULTS AND DISCUSSION

Mangrove Extent

Several iterations were run using different datasets of Sentinel-1, Landsat 8 separately and a combination of both (i.e., Sentinel-1+ Landsat 8) which represents the three scenarios for 2019. This process was repeated using ALOS PALSAR-2 and Landsat 7 to get the corresponding scenarios for 2009. The results of mangrove extent and other land cover changes for the two time periods (2009 and 2019) are presented in Figure 22.

Figure 44: LULC Change Detection for 2009 and 2019 using Different Classification Scenario

Three main classification scenarios were established to quantify the extent of mangroves and other land cover classes for two-time period: classification of optical data only, classification of SAR data only, and the third scenario
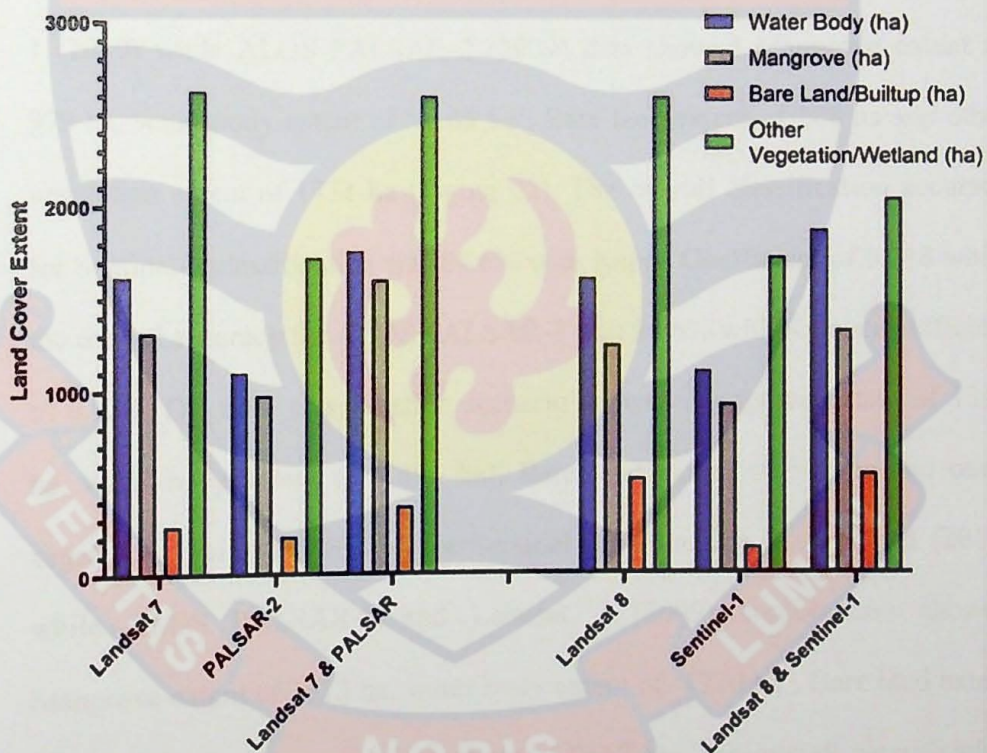
99

combined both optical and SAR data (Figure 23 - 28). The result of Landsat 8 data only (2019) showed Mangrove extent of 1259 ha, water body extent of '1622 ha', Bare land extent of 524 ha and other vegetation extent of 2617 ha while Landsat 7 (2009) data showed Mangrove extent of 1321 ha, water body extent of '1620 ha', Bare land extent of 266 ha and other vegetation extent of 2634 ha (Figure 22). The overall classification accuracy for Landsat 8 was 98.9% with Kappa Coefficient of 0.979 while the overall accuracy for Landsat 7 was 96.8% with Kappa Coefficient of 0.94. The second classification scenario showed Mangrove extent of 933 ha, water body extent of '1115 ha', Bare land extent of 144 ha and other vegetation extent of 1741 ha for Sentinel-1 (2019) while ALOS PALSAR-2 (2009) data showed Mangrove extent of 979 ha, water body extent of '1104 ha', Bare land extent of 208 ha and other vegetation extent of 1731 ha (Figure 22). The overall classification accuracy for Sentinel-1 classification was 84.6% with Kappa Coefficient of 0.718 while the overall accuracy for ALOS PALSAR-2 was 96.6% with Kappa Coefficient of 0.938. The third classification scenario showed Mangrove extent of 1340 ha, water body extent of '1891 ha', Bare land extent of 549 ha and other vegetation extent of 2062 ha for Sentinel-1and Landsat 8 combined (2019) while ALOS PALSAR-2 and Landsat 7 (2009) combination showed Mangrove extent of 1613 ha, water body extent of '1770 ha', Bare land extent of 370 ha and other vegetation extent of 2617 ha. The overall classification accuracy for both Sentinel-1 and Landsat 8 when combined together was 99.1% with Kappa Coefficient of 0.984 while the overall accuracy for both ALOS PALSAR-2 and Landsat 7 was 99.6% with Kappa Coefficient of 0.992. The error/confusion matrix of mangrove classification for each scenario are as

shown in Table 12-17. The result showed that the combination of optical imagery alongside synthetic aperture radar reduced the error of omission or commission of mangroves and increased the user's/producer's accuracy up to 99%.

Figure 45: Mangrove extent Map for the year 2009 for Optical Image only (Landsat 7)
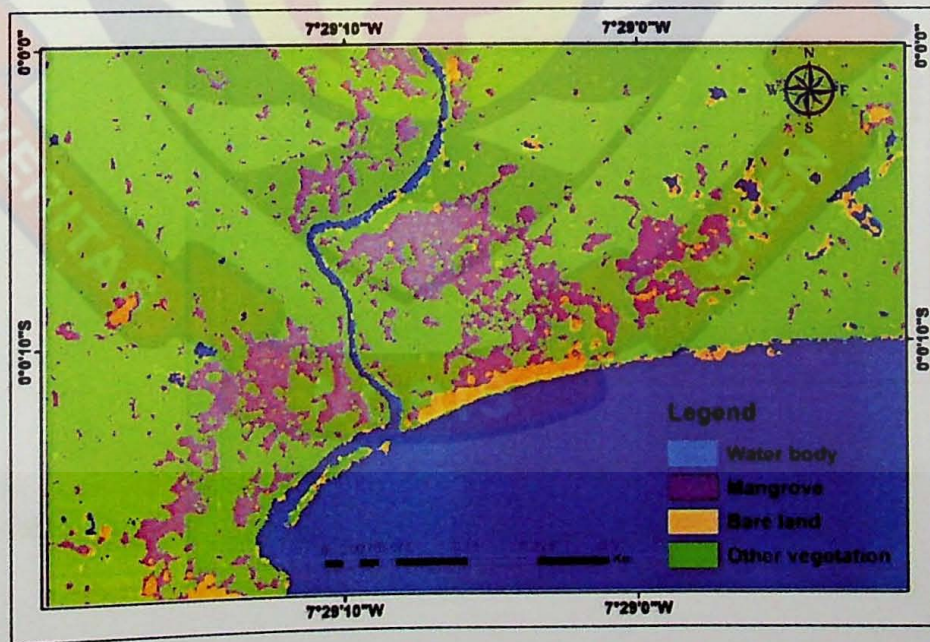
Figure 46: Mangrove extent Map for the year 2009 for PALSAR Image only
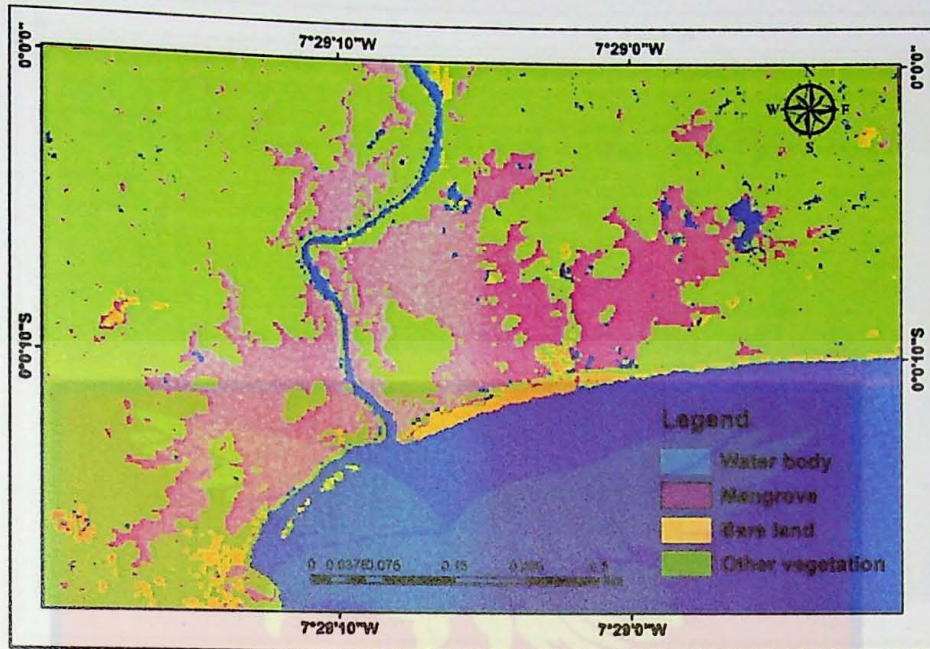
Figure 47: Mangrove extent Map for the year 2009 for both Optical and PALSAR Data
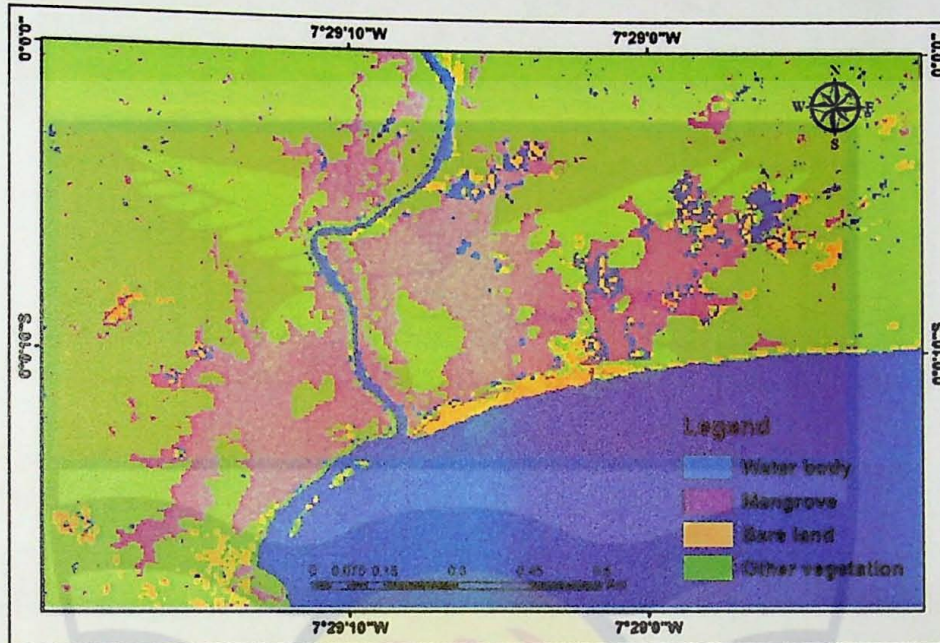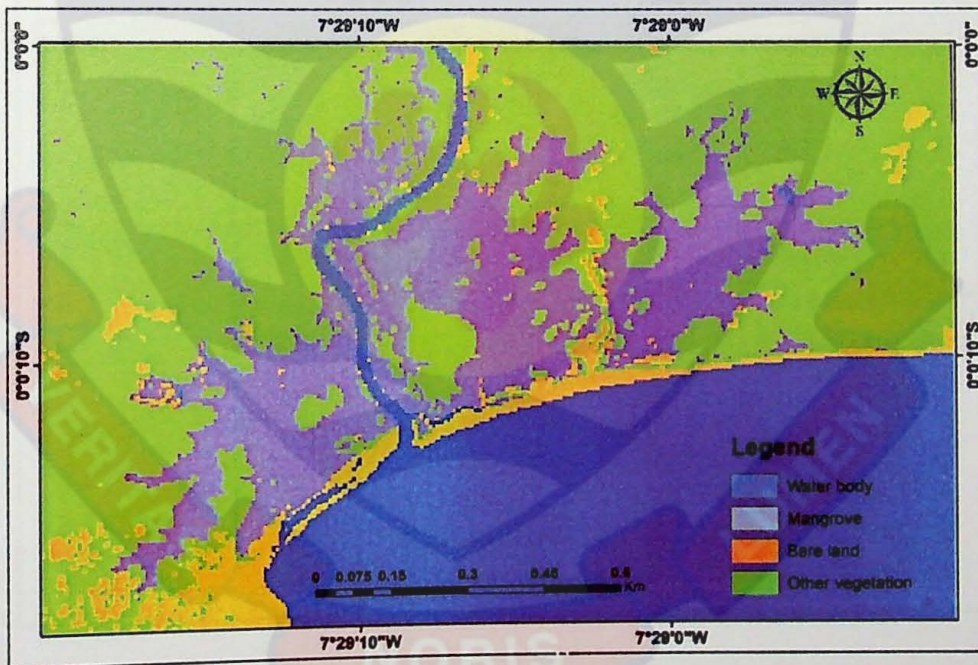

Figure 48: Mangrove change Maps for the year 2019 for Optical Image only (Landsat 8)
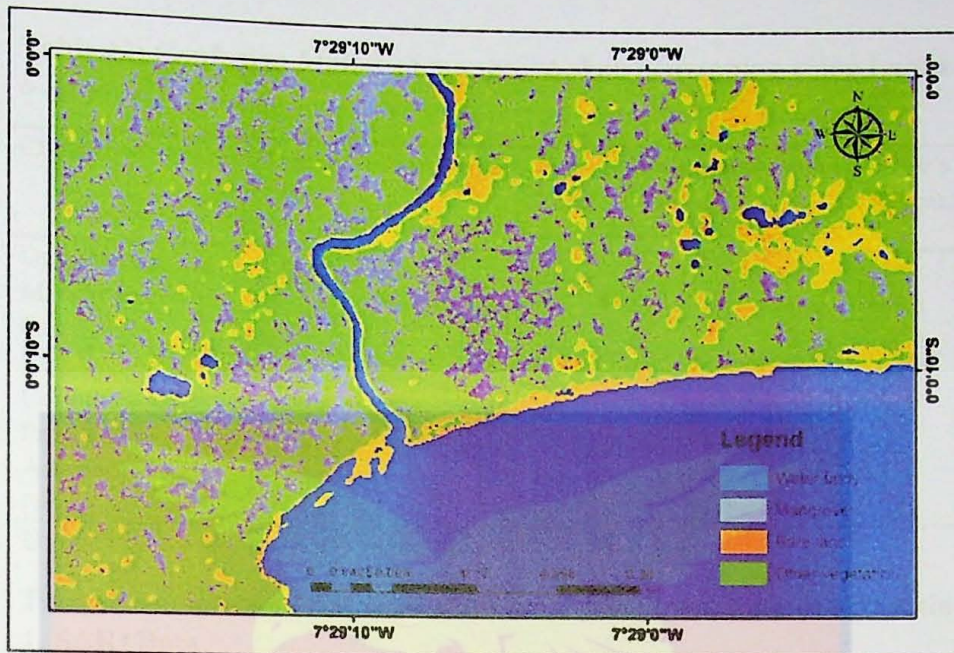
Figure 49: Mangrove extent Map for the year 2019 for Sentinel-1 Image only
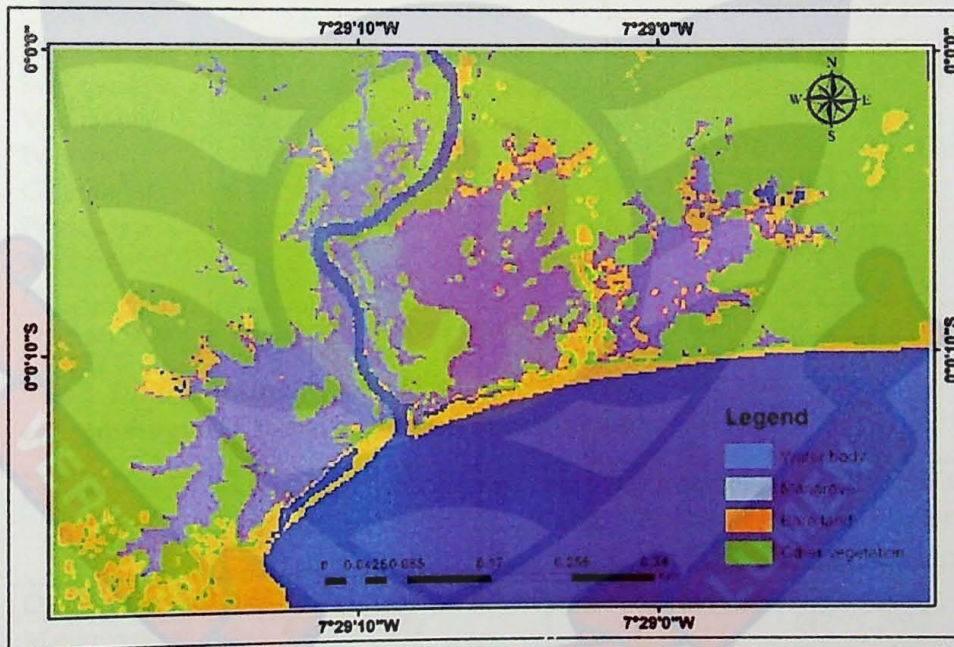
Figure 50: Mangrove extent Map for the year 2019, for both Optical and Sentinel-1 Data

Table 12: Confusion Matrix of mangrove change mapping using Landsat 8 Image

Classes	Open Water	Mangroves	Bare Land	Vegetation/ Wetland	Row Total	User's Accuracy (%)
Open Water	81	0	0	0	81	100
Mangroves	0	635	0	12	647	98.1
Bare Land	4	0	28	0	32	87.5
Vegetation/Wetland	0	3	0	942	945	99.7
Column Total	85	638	28	954	1705	
Producer's Accuracy (%)	95.3	99.5	100	98.7		

Overall Accuracy = 98.9%; Kappa Coefficient = 0.979

Table 13: Confusion Matrix of mangrove change mapping using Sentinel-1 (SAR) Data

Classes	Open Water	Mangroves	Bare Land	Vegetation/ Wetland	Row Total	User's Accuracy (%)
Open Water	79	0	2	0	81	97.5
Mangroves	0	521	0	126	647	80.5
Bare Land	2	0	23	7	32	71.9
Vegetation/ Wetland	0	119	6	820	945	86.8
Column Total	81	640	31	953	1705	
Producer's Accuracy (%)	97.5	81.4	74.2	86		

Overall Accuracy = 84.6%; Kappa Coefficient = 0.718

Table 14: Confusion Matrix of mangrove change mapping using a combination of Optical Satellite Image and SAR (2019)

Classes	Open Water	Mangroves	Bare Land	Vegetation/ Wetland	Row Total	User's Accuracy (%)
Open Water	81	0	0	0	81	100
Mangroves	0	642	1	4	647	99.2
Bare Land	0	0	32	0	32	100
Vegetation/Wetland	0	9	0	936	945	99
Column Total	85	651	33	940	1705	
Producer's Accuracy (%)	100	98.6	96.9	99.6		

Overall Accuracy = 99.1%; Kappa Coefficient = 0.984.

104

When mapping and monitoring coastal ecosystems over an extended period of time using solely optical satellite imagery, Mwita et al. (2012) and Wijedasa et al. (2012) noted a number of drawbacks. For effective land-use and land-cover mapping, recent developments in machine learning classifiers and a proliferation of high-performance cloud computing platforms, such as Google Earth Engine (GEE), have made it possible to merge optical and radar data (Jhonnerie et al., 2015; Midekisa et al., 2017; Erika et al., 2020).

The results show that there are differences in all three classification scenarios for each period (2009-2019). For example, classification using Synthetic Aperture Radar data showed that most structural aspects were captured but underestimated the vegetation cover and this is consistent with observations in other studies (Carreiras et al., 2013; Lucas et al., 2014; Nathan et al., 2018). In contrast, optical satellite image classification captured the tree canopy more (Erika et al., 2020) but seems to overestimated the extent. The ALOS PALSAR-2 data was more effective in characterizing mangroves than the Sentinel-1 data, likely due to the high penetrability of the L-band into mangrove tree canopy as compared to C-band.

Table 15: Confusion/Error Matrix of Land Cover Classification using Landsat-7 Image.

Classes	Open Water	Mangroves	Bare Land	Vegetation/Wetland	Row Total	User's Accuracy (%)
Open Water	76	0	2	3	81	93.8
Mangroves	4	615	1	27	647	95.1
Bare Land	1	4	26	1	32	81.3
Vegetation/Wetland	0	12	0	933	945	98.7
Column Total	81	631	29	964	**1705**	
Producer's Accuracy (%)	93.8	97.5	89.7	96.8		

Overall Accuracy = 96.8%; Kappa Coefficient = 0.936.

105

Table 16: Confusion/Error Matrix of Land Cover Classification using ALOS PALSAR-2 Image.

Classes	Open Water	Mangroves	Bare Land	Vegetation/ Wetland	Row Total	User's Accuracy (%)
Open Water	76	0	0	5	81	93.8
Mangroves	0	**615**	0	32	647	95.1
Bare Land	1	4	**23**	4	32	71.9
Vegetation/Wetland	0	12	0	**933**	945	98.7
Column Total	77	631	23	974	**1705**	
Producer's Accuracy (%)	98.7	97.5	100	95.8		

Overall Accuracy = 96.6%; Kappa Coefficient = 0.938.

The LULC changes for the study area between 2009 and 2019 are as presented in Figure 22 - 28. The results of the scenario that combined both optical and radar images showed that there have been changes in the various LULC (water body, mangrove, bare lands/built-up and other vegetation/wetland) over the two-time period. In 2009, mangrove covered 1613 ha, bare land/built-up areas accounted for 370 ha, other vegetation/wetland accounted for 2617 ha while water body covered about '1770 ha' equivalent. In 2019, mangrove decreased to 1340 ha, bare lands/built-up increased to 549 ha, other vegetation/wetland decreased to 2062 ha while water body increased to 1891 ha. There is significant change in mangrove cover (16.9% loss), bare land/built-up areas (45% gain), other vegetation/wetland (21% loss) and water body (7% gain). This indicates that mangrove and other vegetation have been converted to either bare land (which could be agricultural land) or built-up areas. Water body has also taken up part of the areas which were previously covered by either mangrove or other vegetation.

Table 17: Confusion/Error Matrix of Land Cover Classification using a combination of Landsat-7 Image and ALOS PALSAR-2.

Classes	Open Water	Mangroves	Bare Land	Vegetation/ Wetland	Row Total	User's Accuracy (%)
Open Water	81	0	0	0	81	93.8
Mangroves	0	647	0	0	647	95.1
Bare Land	0	1	26	5	32	81.3
Vegetation/Wetland	0	1	0	944	945	98.7
Column Total	81	649	26	964	1705	
Producer's Accuracy (%)	93.8	97.5	96.9	99.5		

Overall Accuracy = 99.6%; Kappa Coefficient = 0.992.

We used confusion matrices and an independent accuracy assessment to provide detailed statistical information for each classification scenario. The confusion matrix for Sentinel-1 image classification alone showed that out of 647 pixels which were identified as Mangrove, 521 pixels were correctly classified while the confusion matrix for the corresponding optical image alone showed that out of 647 pixels which were identified as Mangroves, 635 pixels were correctly classified (Table 12-17). However, relatively high confusion was found between mangrove and other vegetation for Sentinel-1 and ALOS PALSAR-2 classification as revealed by the independent accuracy assessment (Figure 7 - 9). It was also revealed that the Sentinel-1 and ALOS PALSAR-2 images alone tend to underestimate the mangrove vegetation canopy, however, ALOS PALSAR-2 performed better than Sentinel-1 (Figure 22). On the other hand, Landsat 7 and Landsat 8 alone tend to overestimate the vegetation cover. The overall classification accuracy for the Sentinel-1 image was 84.6%, while the overall accuracy for the Landsat 8 alone was 98.9%. The overall accuracy when both images were combined was 99.1% with kappa coefficient of 0.984 showing that the classification using a combination of optical and radar data has a better agreement in the observations (Table 15-

17). It was observed that the combination of Landsat-7 and ALOS PALSAR-2 produced better accuracy indicating that L-band performs better than C-band.

The third classification scenario that combines optical and radar data yielded the best classification results for 2009 and 2019 as the classes were relatively well distributed, capturing both clustered mangroves and mangrove patches near the water body (Figure 23-28). The visual interpretation showed that the third classification scenario achieved a better result, indicating the high potential of this mangrove assessment and monitoring method. The independent accuracy assessment underscores the robustness of this approach, as shown in Figure 7 - 9. Despite the fact that the same 'training sample' was used to train the classifier, the accuracies differ depending on the scenario. The scenario combining both optical and radar data showed better agreement and less confusion compared to when either optical or radar data was used.

This study confirms that combining synthetic aperture radar data with optical satellite data is the way forward in mangrove assessment and mapping, as recommended by several authors (Attarchi & Gloaguen, 2014; Ayman et al., 2017; Hu et al., 2020). The random forest algorithm performed well to clearly classify the different land cover classes within the study area. The resulting classification is consistent with other studies that used random forest algorithms for land cover classification (Ming et al., 2016; Thanh et al., 2020).

Estimation of Canopy Height and Above Ground Biomass

The mangrove canopy height map was generated for the year 2000 using the global mangrove distribution vector file, SRTM DEM, and SAR data. This was then utilized to create estimates of AGB for the same time period.

108

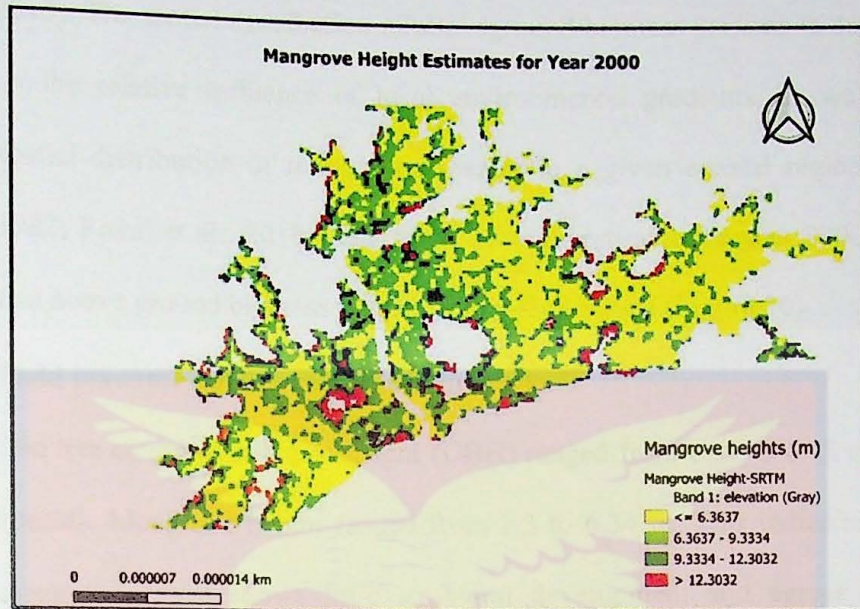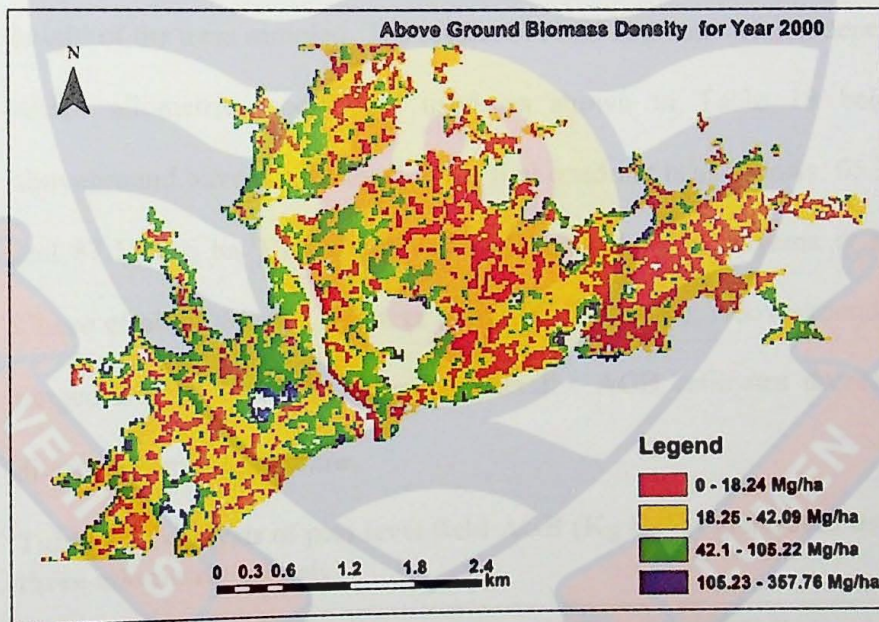*Figure 29: Mangrove Height Estimates for Year 2000*

Figure 30: Mangrove AGB Estimates for Year 2000

The analysis of mangrove canopy height distribution shows that in year 2000, mangrove canopy height ranges from about 6.3 – 12.7 m (Figure 29). This estimate of mangrove height significantly corresponds to previously reported values in different estuaries in Ghana (Aheto et al., 2011 and Nortey et al.,

2015). The spatial distribution of aboveground biomass patterns is determined by the relative influence of local environmental gradients, as well as the spatial distribution of mangroves species in a given coastal region (Thom, 1982; Rovai et al., 2018). The result of AGB estimate for year 2000 showed that above ground biomass ranged from 0–368 mg/ha (Figure 30).

Field inventory of above ground biomass

The tree diameter at breast height (DBH) ranged from 0.67 to 6.48 cm for all species. Mangrove height ranged from 2.3 to 6.34 m. This indicates that the mangrove forest shows little structural development and agrees with the results of Aheto et al., 2011 and Nortey et al., 2015 at different estuaries in Ghana. There is a strong correlation between height and diameter at breast height of the trees sampled. The results of AGB estimates varied depending on which allometric model was used, as shown in Table 18 below. The aboveground biomass observed in the first quadrant is as follows: 65.33, 39.80 and 87.52 (kg ha^{-1}) for the equation developed by Komiyama et al., 2005; Chave et al., 2005 and Njana et al., 2015 (Table 17). Aboveground biomass ranged from 0 to 87.52 kg ha^{-1}. Generally, AGB estimates decreased with distance from the shoreline.

Table 18: Analysis of plot level field AGB (Kg ha−1) generated using three allometric models

Quadrant	H (m)	DBH (cm)	AGB (kg) A	AGB (kg) B	AGB (kg) C
1	3.2- 6.3	1.4 – 6.48	65.33	39.80	87.52
2	2.3 -6.0	0.67 – 4.91	32.77	19.16	43.40
3	0	0	0	0	0
4	2.5-6.10	4.48	8.75	5.43	11.54

The best estimate of aboveground biomass was obtained with the regression model coupling tree height, wood density, and diameter at breast height, which agrees with the results of other researchers (Nortey et al., 2015; Fatoyimbo et al., 2018). It was found that GEE has the potential to estimate the spatial distribution of AGB densities in mangroves. The SRTM canopy elevation was also very strongly correlated with the field elevation measurements. The main aim of using GEE in this study was to explore its ability to estimate AGB using SRTM data. Previously, AGB estimation involved highly complex calculations that required Python or Java code in MATLAB software (Lagomasino et al. 2016; Nsset et al., 2016; Qi & Dubayah, 2016).

Preliminary Hydrodynamic Simulations

Model Calibration Result

The model was calibrated by comparing simulated water surface elevation results against gauge measurements. The comparisons between simulated and measured water surface elevation for the Takoradi Gauge Station are shown in Figure 31 - 33. The simulated and measured water surface elevations matched better when the Manning's roughness value was set to 0.1825 and this setting was used for the simulation of 100 tidal cycles. For the standard error of estimate (Sy.x), the smaller the values, the better the estimates. The corresponding goodness-of-fit statistics are presented in Table 19.

111
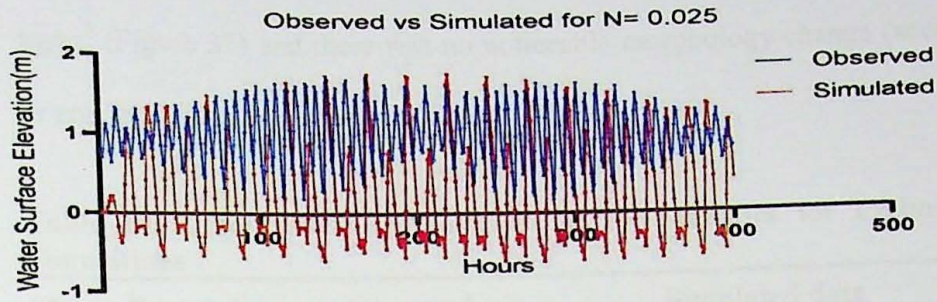
Figure 31: Computed vs Observed Water Surface Elevation (Manning's N=0.025)
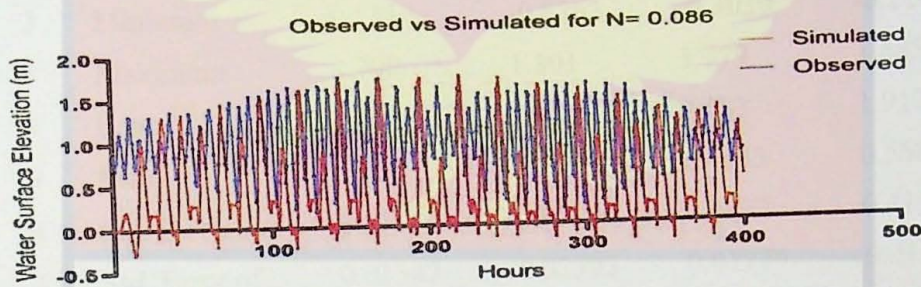
Figure 32: Computed vs Observed Water Surface Elevation (Manning's N=0.086)
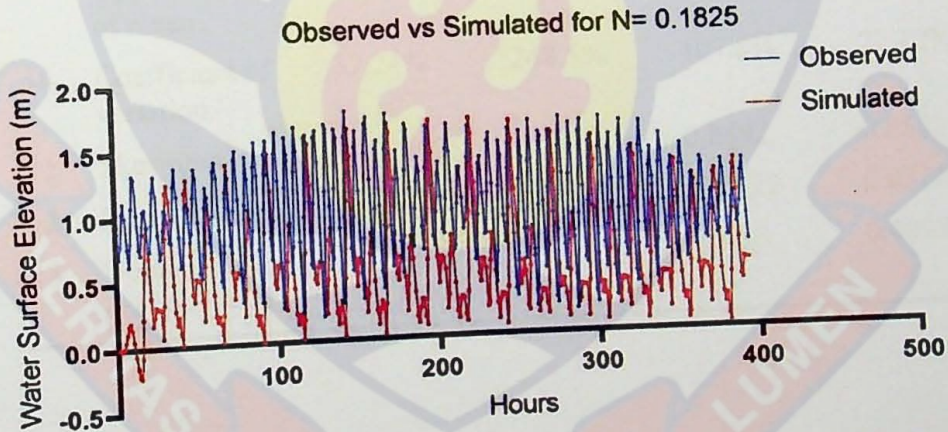
Figure 33: Computed vs Observed Water Surface Elevation (Manning's N=0.1825)

For the one-month simulation using Manning's N=0.1825 and without SLR, the maximum current velocity was 0.06 m/s (Figure 34), the maximum sediment concentration recorded in a small section of the domain was 0.001

112

kg/m³ (Figure 35) and there was no noticeable morphology change (accretion or erosion) throughout the area (Figure 36).

Table 19: Descriptive and Goodness of Fit Statistics for Preliminary Simulations

SN	Description	Observed data	Simulated data		
			N=0.025	N=0.086	N=0.1825
1	Number of values	773	773	773	773
2	Minimum	0.1310	-0.6362	-0.3039	-0.2267
3	Maximum	1.798	1.801	1.779	1.685
4	Range	1.667	2.437	2.083	1.912
5	Mean	1.005	0.2702	0.4633	0.5688
6	Std. Deviation	0.3744	0.6714	0.4992	0.4102
7	Std. Error of Mean	0.01347	0.02393	0.01779	0.01475
8	Lower 95% CI of mean	0.9790	0.2232	0.4283	0.5398
9	Upper 95% CI of mean	1.032	0.3172	0.4982	0.5977
10	Coefficient of variation	37.24%	248.5%	107.8%	72.12%
11	Skewness	-0.03162	0.5930	0.8492	0.8582
12	Kurtosis	-0.8560	-0.9393	-0.3122	0.03129
13	Goodness of Fit (Sy.x)	0.3764	0.6732	0.5001	0.4098

113
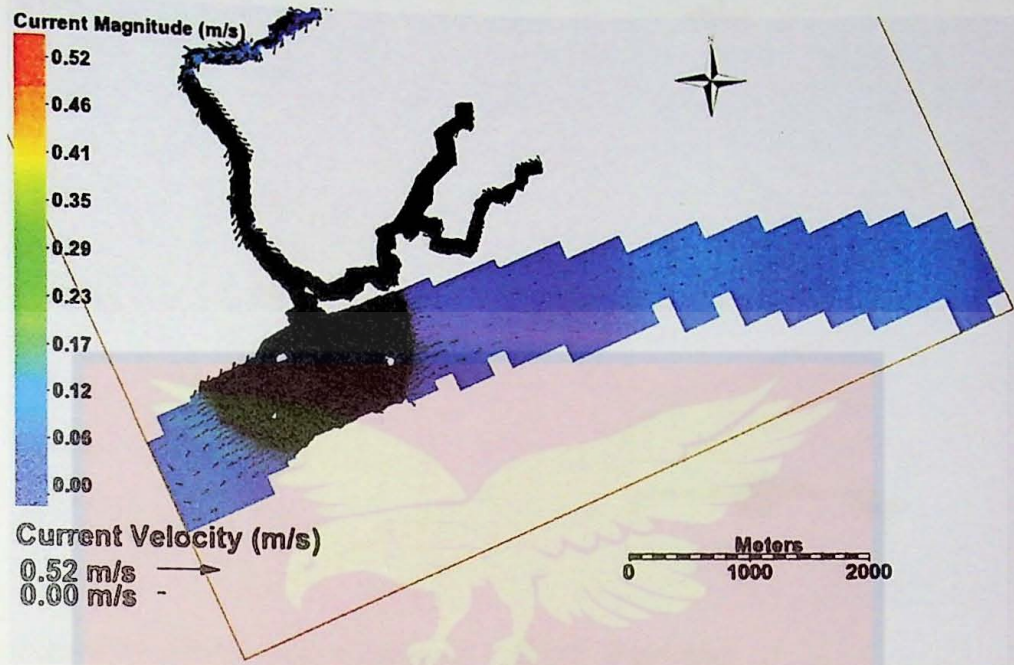
Figure 34: Current Magnitude and Velocity for 1 Month Simulation
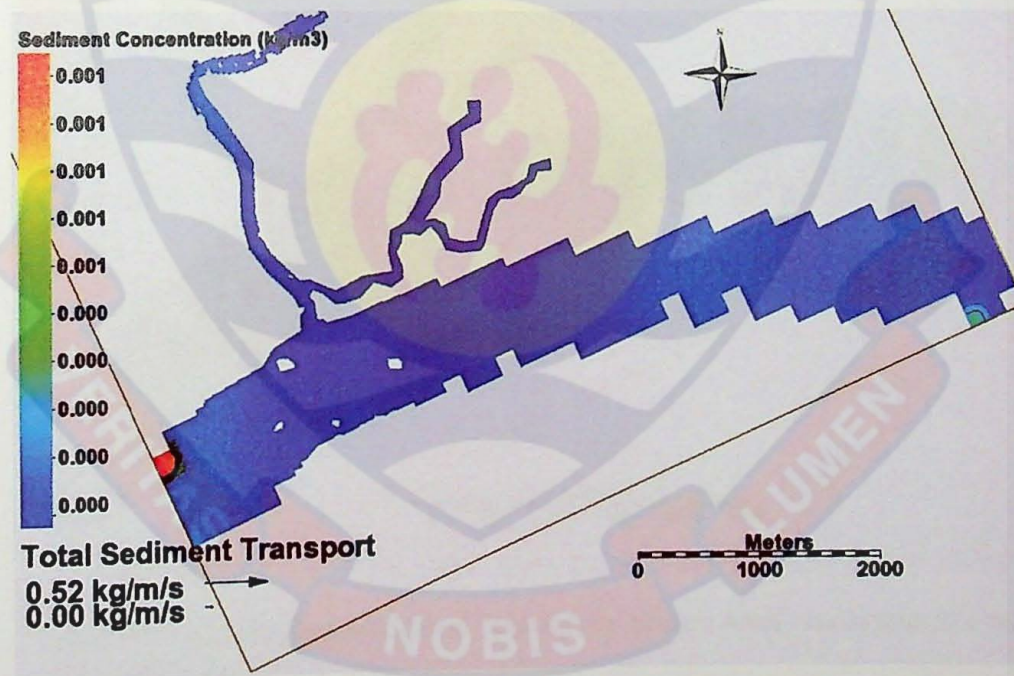
Figure 35: Sediment Concentration and Transport for 1 Month Simulation

114
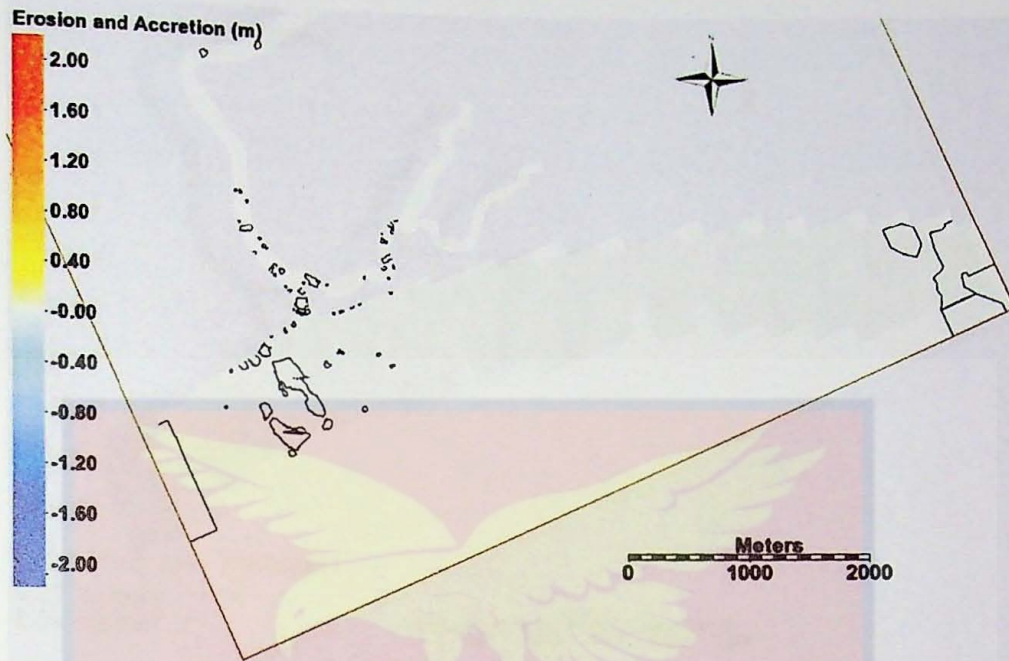
Figure 36: Morphology Change for 1 Month Simulation
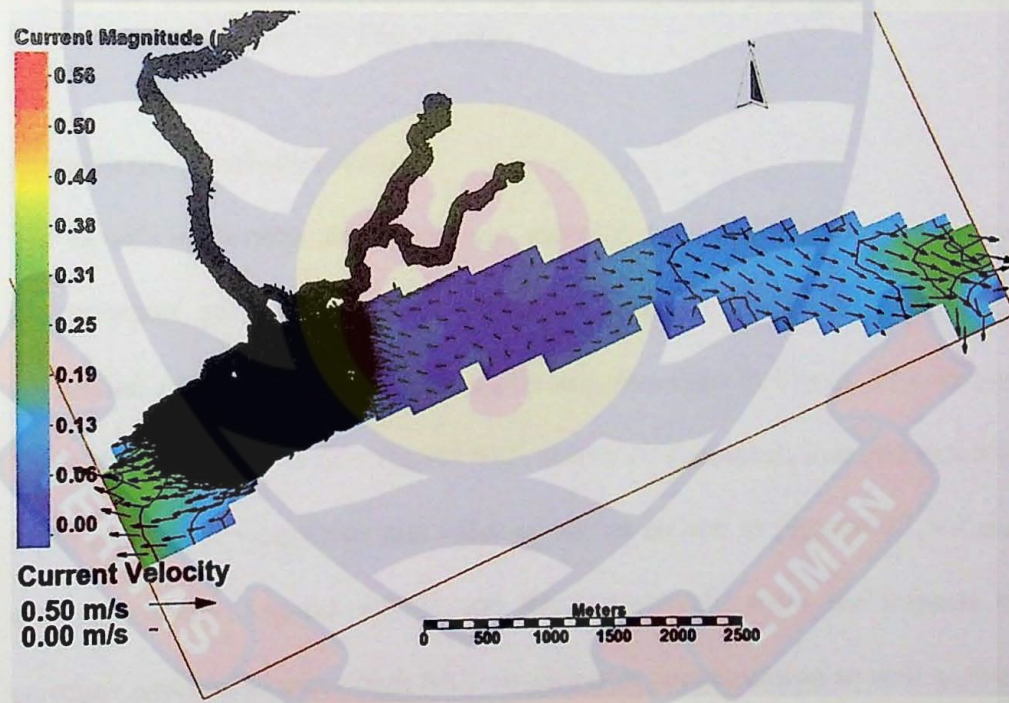
Figure 37: Current magnitude and velocity for no-sea level rise scenario over 100 Tidal Cycles

115
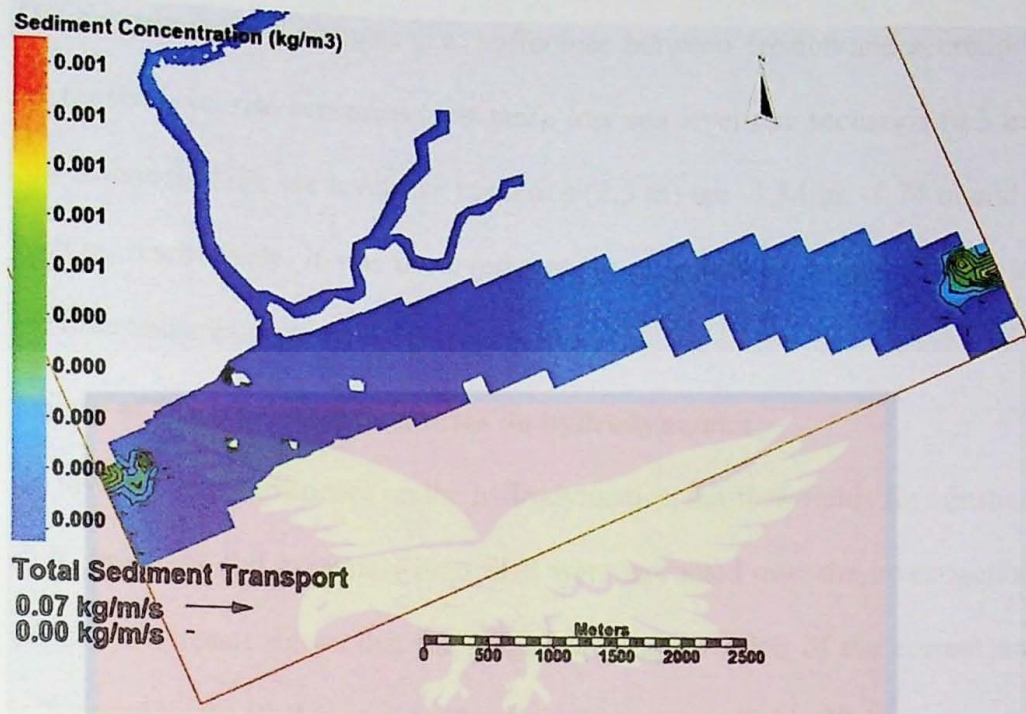
Figure 38: Sediment concentration and total sediment transport for no-sea level rise scenario for 100 Tidal Cycles

Long Term Simulation Result

The results of current magnitude and velocity, total sediment concentration and transport, and morphological changes after a 100 tidal cycle (~8.4 years) simulation under varying sea level curve are presented in Figure 37 - 45 and Table 19. The impacts of different SLR scenarios (constant, low and extreme high) on current magnitude and velocity are as shown in Figures 37, 40 and 43, respectively. Figures 38, 41 and 44, respectively show the impacts of constant, low and extreme high SLR on sediment concentration as well as total sediment transport. Figures 39, 42 and 45 show the impacts on accretion and erosion. These values appear to be similar in Figure 37 – 45, however, Table 19 clearly shows the variations. Morphology change was calculated by subtracting the accretion from the erosion and this is interpreted as net morphology change (Table 19).

116

The net morphology changes (i.e., difference between erosion and accretion) for no sea level rise scenarios (constant), low sea level rise scenarios (0.3 m) and extremely high sea level rise scenarios (2.5 m) are -1.84 m, -1.74 m and -2.29 m, respectively. It was observed that the area will be inundated 71% of the time under extreme high sea level scenario.

Effects of Different SLR Scenarios on hydrodynamics

To investigate the influence on the hydrodynamics, the flow fields for constant SLR, low SLR and extremely high SLR were extracted over the investigation period. The result shows that the magnitude and direction of the current are influenced by the SLR scenario. This result is shown in Table 20.
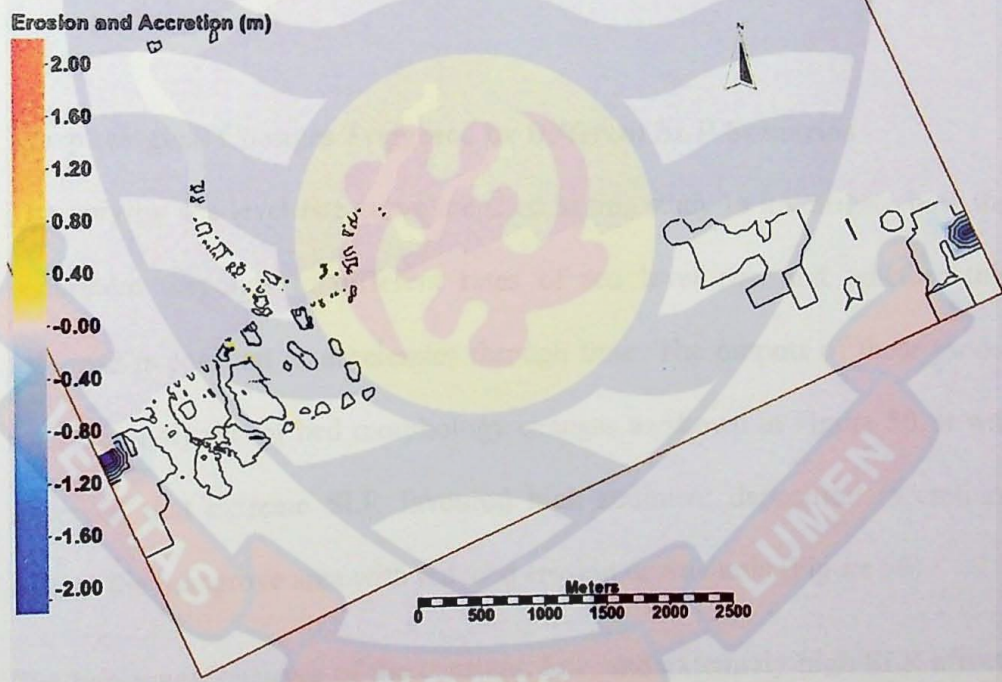
Figure 39: Change in morphology for no-sea level rise scenario for 100 Tidal Cycles
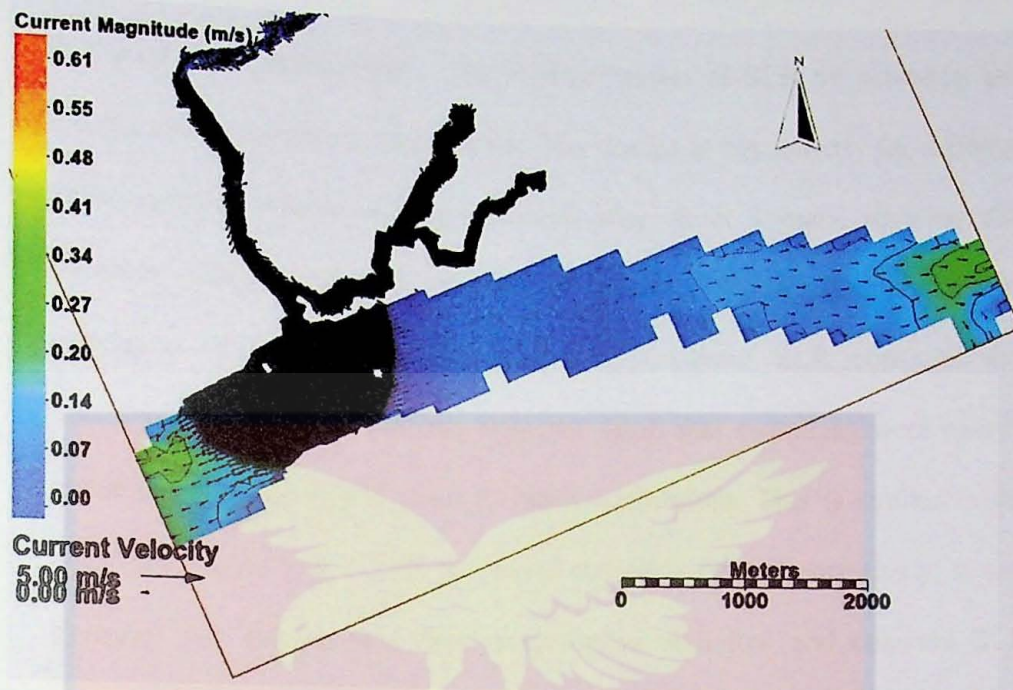
Figure 40: Current magnitude and velocity for low sea level rise scenario for 100 Tidal Cycle

Morphological Changes Triggered by Different SLR Scenarios

The varying sea level rise curve are used in this study to investigate how the ecosystem responds to different rates of sea level rise and whether this response is constant or accelerates through time. The outputs of these model runs are analyzed for bed morphology changes as shown in Figure 50. It was observed that extreme SLR favoured high sediment deposition (accretion) around the mangrove area with reduced erosion downwards (Figure 50).

The hypsometric curves of the constant, low, and extremely high SLR effects on morphological changes after 100 tidal cycles as shown in black, blue, and red-coloured lines in Figure 50 show that, although the differences are small, significant morphological changes occurred toward the end of the simulation period. This finding is similar to the observations of van Maanen et al., 2013

118

in a sandy tidal embayment. The relative impact of SLR on accretion and erosion can be seen from these curves. The change in hypsometry for different SLR scenarios became more pronounced after about 5 years, showing that accretion mainly occurred before this period. The Preliminary model simulation of one month (one tidal cycle) without SLR confirms this observation. It could be inferred from the result that sediments were mainly redistributed in the first 4 years to reach equilibrium. This is similar to the observation of Li et al., 2013 at a naval station in USA. Interestingly, it was observed that erosion was more pronounced with low and constant SLR whereas erosion decreased with extreme high SLR scenario at the end of the simulation period. Again, van Maanen et al. (2015) and Khojasteh et al. (2021) recorded that during sea level rise, mangrove can enhance accretion while hindering erosion downwards. In general, sea level rise resulted in downward erosion of the shoreline, a process which was influenced by the presence of mangroves in the upper part around the inlet.
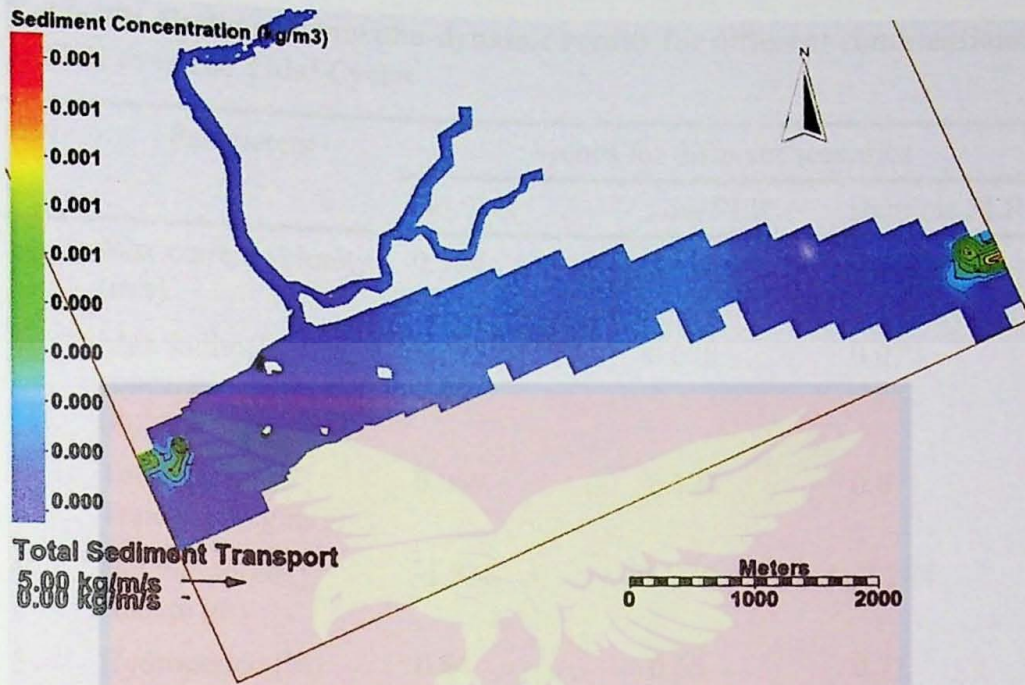
Figure 41: Sediment concentration and total sediment transport for low sea level rise scenario over 100 Tidal Cycles
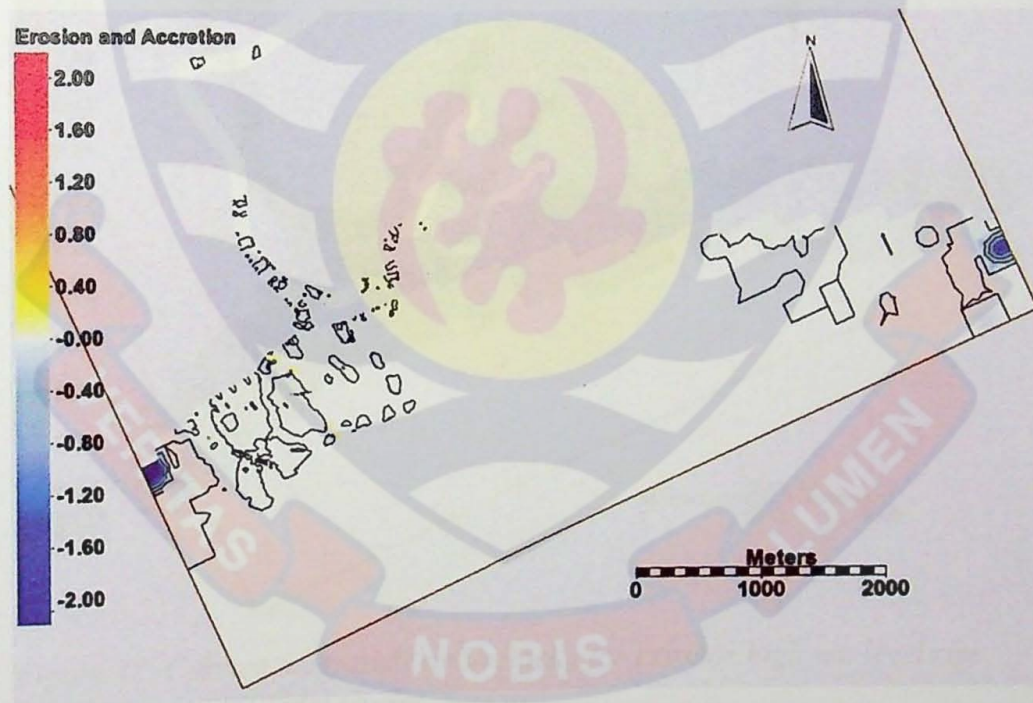
Figure 42: Change in morphology (m) for low sea level rise scenario over 100 Tidal Cycles

Table 20: Hydro and morpho-dynamic results for different combinations of SLR over 100 Tidal Cycles

SN	Parameters	Values for different scenarios		
		No SLR	Low SLR	Extreme SLR
1	Max current velocity (m/s)	0.564	0.613	0.548
2	Max sediment concentration (kg/m^3)	0.075	0.078	0.077
3	Total Sediment Transport (kg/m/s)	0.069	0.124	0.071
4	Net morphology change (m)	-1.836	-1.74	-2.288
5	Hydroperiod (%)	0.64	0.65	0.71
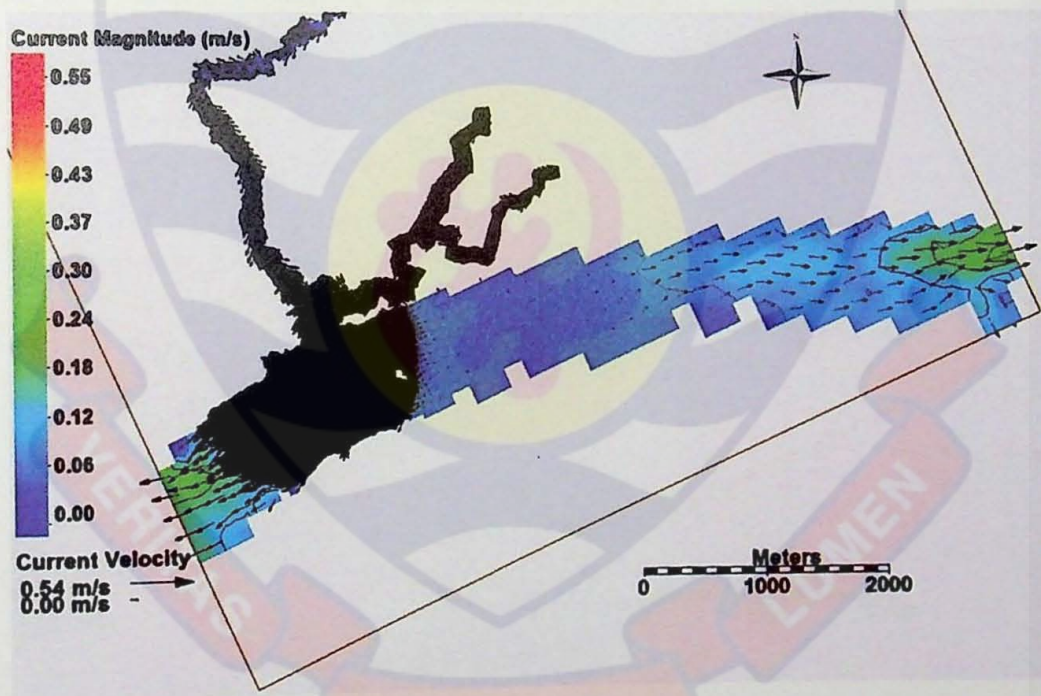
Figure 43: Current magnitude and velocity for extreme high sea level rise scenario over 100 Tidal Cycles

121
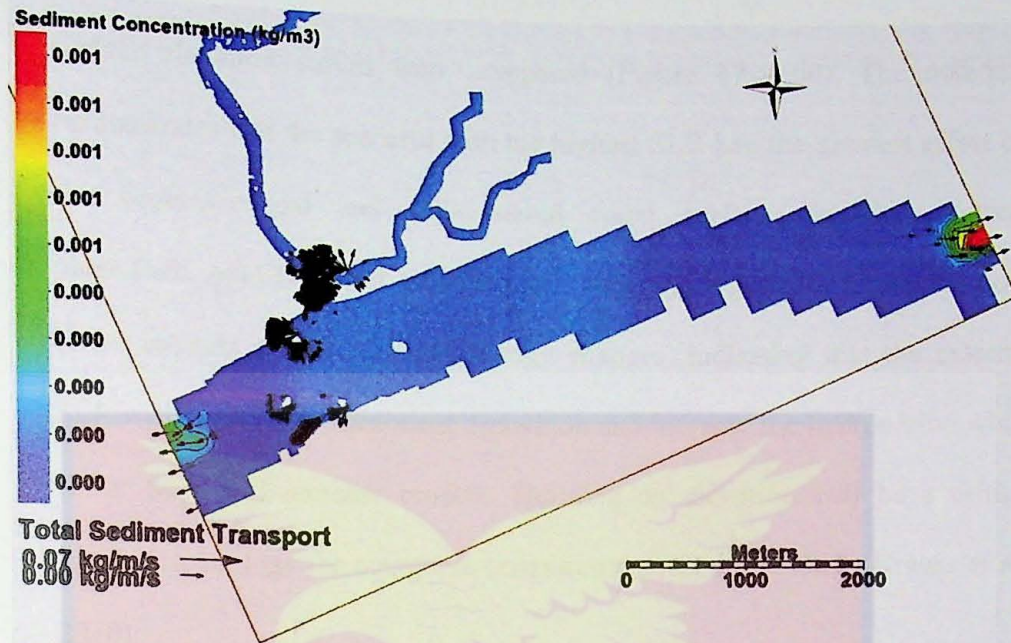
Figure 44: Sediment concentration and total sediment transport for extreme high sea level rise scenario over 100 Tidal Cycles
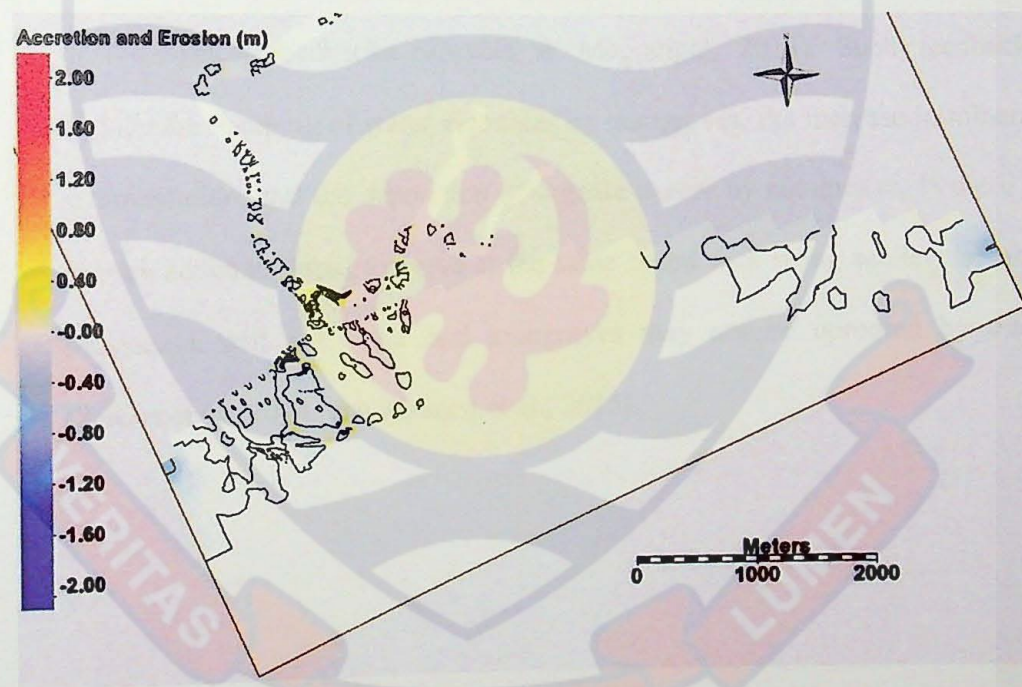
Figure 45: Change in morphology for extreme high sea level rise scenario over 100 Tidal Cycles

Additional details about the flow characteristics in tidal environments can be found in velocity curves, total sediment transport, and water surface elevation (Hunt et al., 2015). As a result, each SLR scenario's generated current magnitude, total sediment concentration, total sediment transport, and water

122

surface elevation curves were compared (Figure 47 - 50). The outcome demonstrates that the scenario with the highest SLR had the greatest effect on the depth-averaged and cell-centered water surface elevation, current magnitude, total sediment transport, and velocity. Figure 46 shows the non-linear impacts of SLR on morphology changes, indicating that the extreme SLR will favour more sediment deposition and increase the hydroperiod while lower SLR will increase erosion. Building up elevation will be a critical adaptation strategy for mangrove ecosystems under lower SLR (Krauss et al., 2010).

Changes in bed elevation in the mangrove ecosystem depend on a combination of biophysical feedbacks (Kirwan & Megonigal, 2013). Such feedbacks include the damping of water velocities by mangroves, the increase in mineral sedimentation, and the deposition of organic matter by mangroves. If there is enough sediment input to move at the same speed with rising sea levels, land subsidence will not occur and mangroves may not be uprooted by tides (Perona et al., 2014; van Maanen et al., 2015).
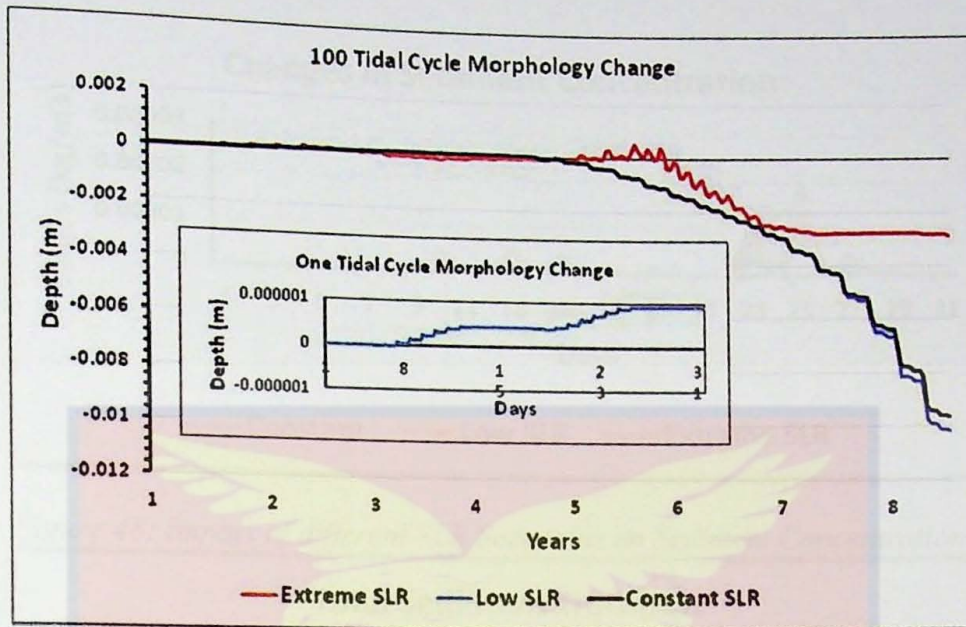
Figure 46: Hypsometric Curve for Morphological Changes induced by SLR
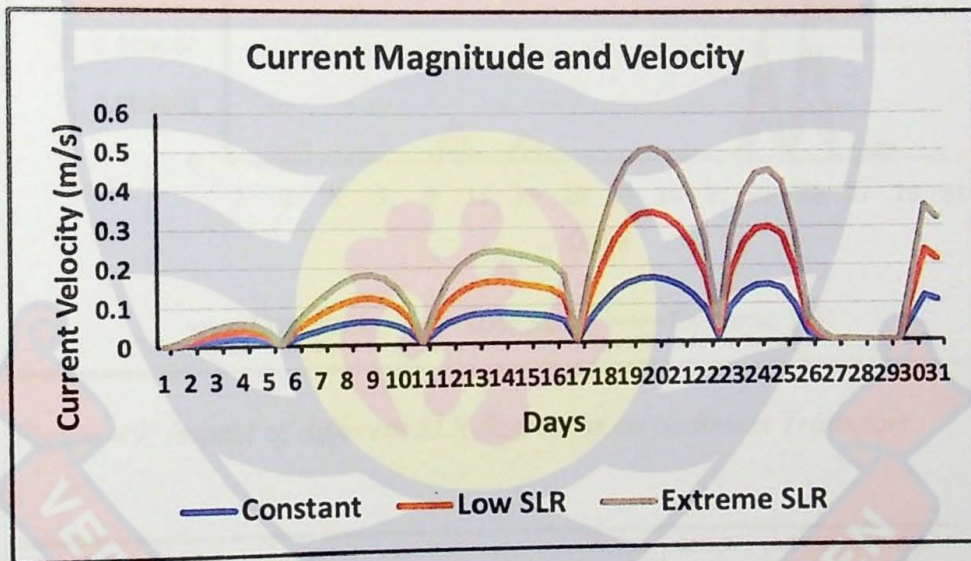
Figure 47: Impact of different SLR Scenarios on Current Magnitude and Velocity

124

Changes in Sediment Concentration
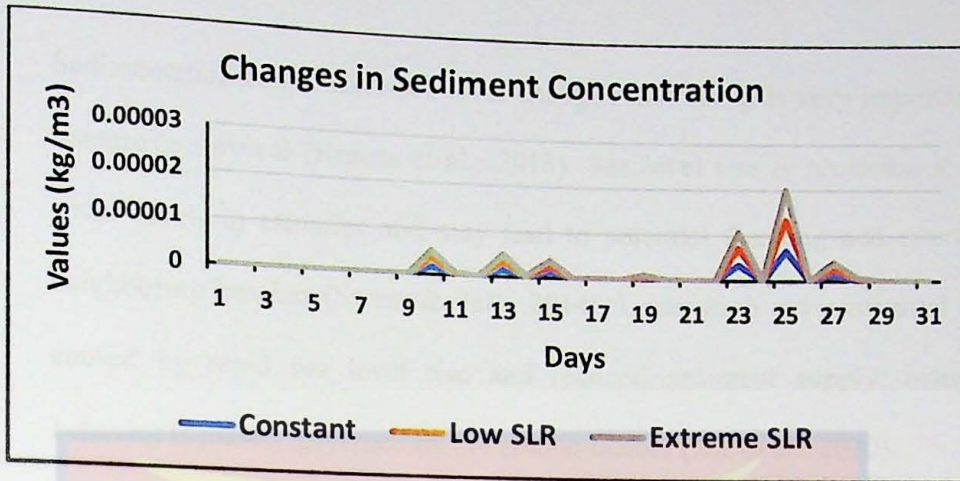
Figure 48: Impact of different SLR Scenarios on Sediment Concentration

Total Sediment Transport
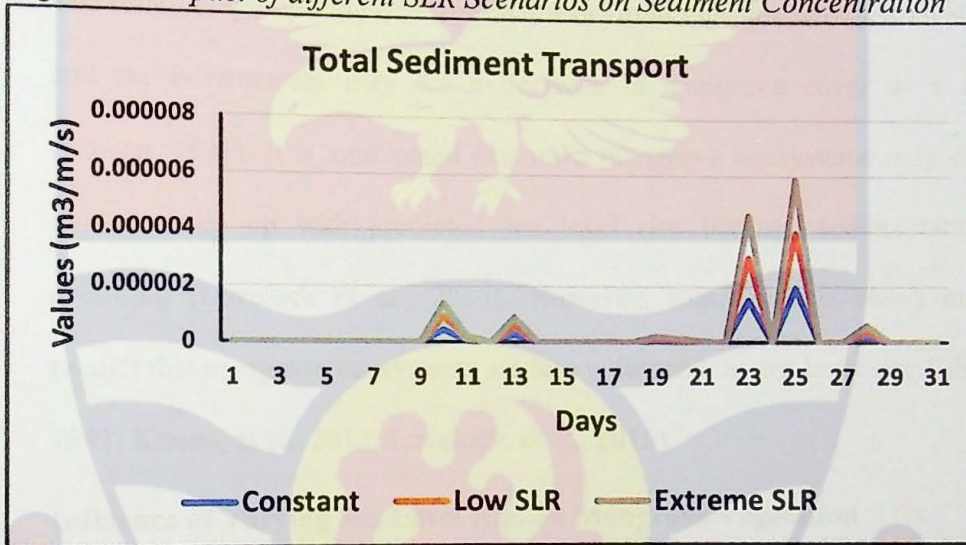
Figure 49: Impact of different SLR Scenarios on Sediment Transport

Water Surface Elevation Changes
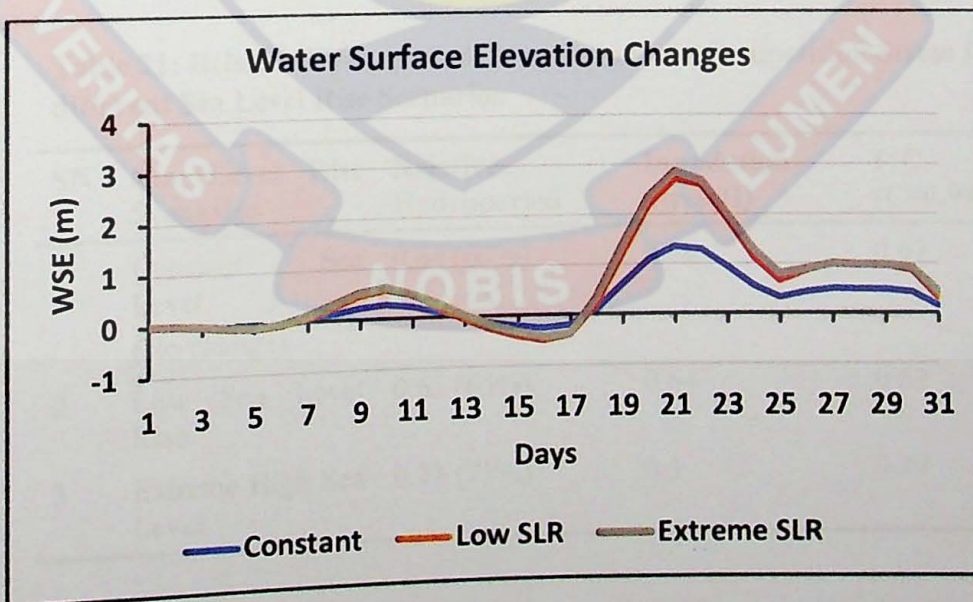
Figure 50: Impact of different SLR Scenarios on Water Surface Elevation

125

Sedimentation and relative sea level change relationship is very important for mangrove survival (Krauss et al., 2013). Sea level rise is projected to raise water levels in estuaries and may lead to potential flooding and erosion of neighboring beaches (Sweet & Park, 2014). Under high environmental stress caused by rapid sea level rise and reduced sediment supply, mangrove behavior is mainly governed by the abiotic factors (Xie et al., 2020).

The relative hydroperiod of mangrove ecosystem changes with sea level rise, and the environment may see a decrease in mangrove cover as a result (Ellison, 1991). It is anticipated that most mangrove ecosystems may not be able to keep up with predicted sea level rise because sedimentation is declining (Lovelock et al., 2015). However, some process-based models predict that mangrove ecosystems are less vulnerable to sea level rise (Ellison, 1991; Krauss, et al., 2013; Lovelock, et al., 2015).

Influence of Varying Sea Level Rise on Mangrove Vegetation

To examine the possible impacts of SLR on mangrove ecosystem, this study focused on how different scenarios of SLR will impact the inundation regime.

Table 21: Relative Hydroperiod, Inundation and Competition Stress for different Sea Level Rise Scenarios

SN	Sea Level Rise Scenarios	Relative Hydroperiod	Inundation Stress(I)	I*C (C=0.99)
1	Constant Sea Level (No change)	0.64 (64%)	0.68	0.67
2	Low Sea Level Rise	0.65 (65%)	0.64	0.63
3	Extreme High Sea Level	0.71 (71%)	0.3	0.29

The inundation regime is an important factor that controls mangrove survival. The results are presented in Table 21. It was observed that the mangrove will be inundated for too long (71% of the time) under extreme SLR. According to van Maanen et al., (2015), Mangrove mortality occurs when the product of the correction factors for mangrove growth caused by inundation (I) and competitive stress (C) is less than 0.5. According to our findings, under the extreme high SLR scenario, the product of inundation (I) and competitive stress (C) is 0.29 which is less than 0.5 (Table 21), indicating that during periods of extreme sea level rise, the mangroves may stay submerged for a longer time, which may have an impact on their growth and general productivity. This finding is consistent with the observations of other researchers from different places (Geselbracht et al., 2015; van Maanen et al., 2015; Xie et al., 2020). According to Crase et al. (2013), mangrove roots cannot withstand being submerged for more than half of the tidal cycle.
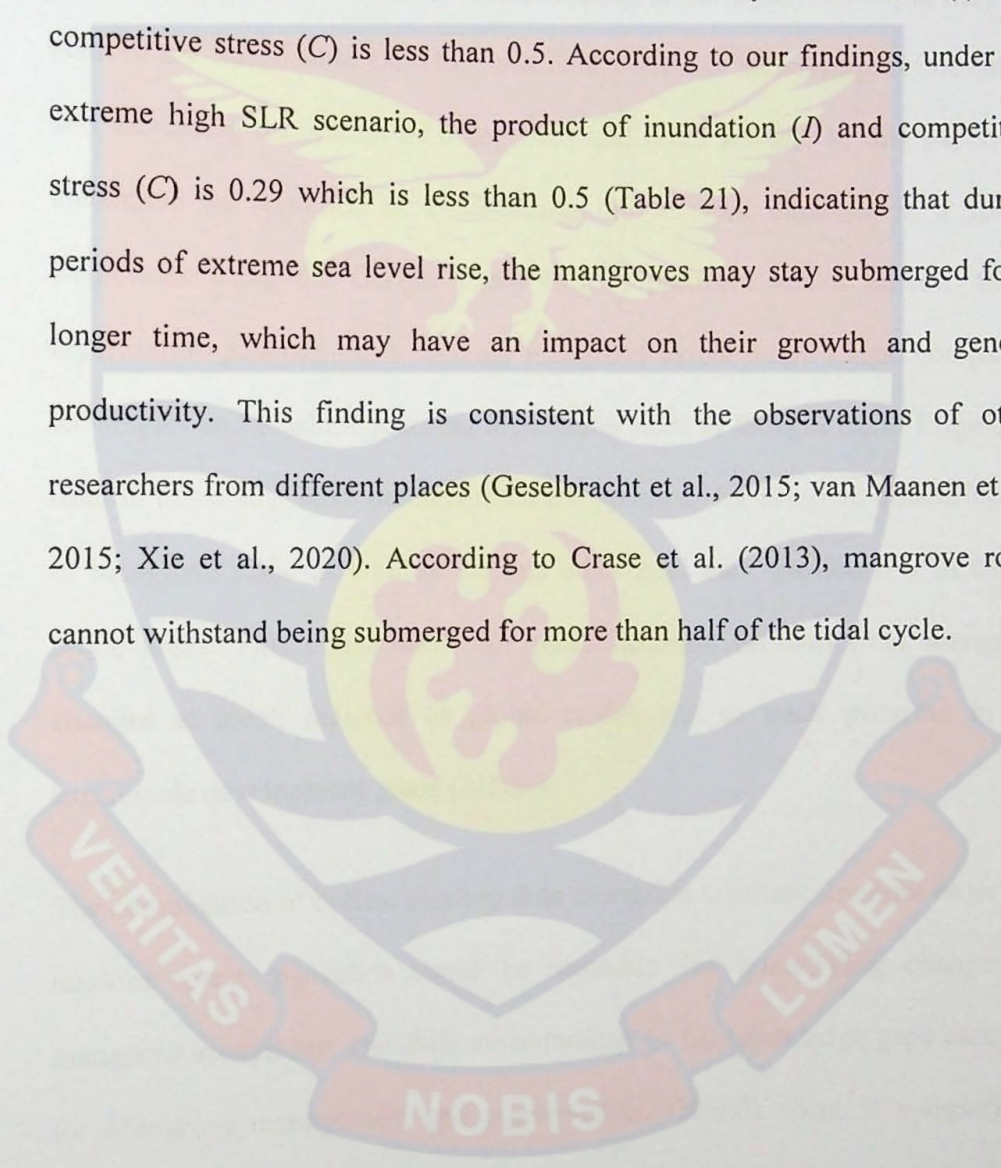
CHAPTER FIVE

CONCLUSION AND RECOMMENDATIONS

Conclusion

The destruction of tropical and subtropical mangrove forests worldwide is one of the most urgent environmental catastrophes of our time. The world may not achieve the Sustainable Development Goals without addressing deforestation and increasing restoration of mangroves and other forests. In this paper, we elaborated an approach to synthesizing the relevant database in a spatial framework using the Google Earth Engine platform and a random forest algorithm to generate more accurate mangrove extent maps. Cloud computing techniques and machine learning algorithms such as Google Earth Engine, as used in this study, have demonstrated the potential for accurate quantification of mangrove stand as well as various other land uses, particularly in cloud-prone areas. This could allow for more accurate estimation of mangrove changes at local, regional or global scales and to track progress in the sustainable development goals (SDGs).

The combination of optical satellite data alongside synthetic aperture radar and random forest algorithm could be valuable for quantifying changes in mangrove ecosystems and their surroundings to fill knowledge gaps essential for Mangrove management and conservation. Overall, there is a significant (16.9%) decadal decline in mangrove extent at the study site which could be attributed to land conversion, reflecting the need for conservation and appropriate monitoring and management.

128

The hydrodynamics of the ecosystem are significantly impacted by the tidal flow caused by various sea level rise scenarios. This in turn impacted the morpho-dynamics, which in turn influenced the growth and development of Mangroves. The rate of morphological change is affected by the rate of sea level rise, with higher sea level rise leading to greater accretion and inundation. The bed profile hypsometric curve shows the impacts of the sea level rise scenario on morphology. For the three sea level scenarios tested, hypsometry appears to be relatively linear over the first half of the simulation. However, after 5 years there was a sharp change in morphology that lasted until the end of the simulation period. The influence of sea level rise on mangrove dynamics could be significant, particularly in situations with extremely high sea levels. Additionally, the relative hydroperiod for the three scenarios tested are 64%, 65%, and 71%, suggesting that for the scenario with a substantial rise in sea level, the ecosystem is submerged 71% of the time, adding to the stress on mangroves.

This type of study can help coastal managers to understand where mangroves are currently found and how they have changed over time. The maps produced in this study are suitable to inform coastal management in the region and the methodology can be reproduced for the entire coastal zone of Ghana and beyond. In order to manage mangrove ecosystems effectively, it will be crucial to comprehend the intricate interactions between tidal flow, coastal hydrodynamics, morpho-dynamics, sea level rise, and their effects on mangrove vegetation. Policymakers in charge of preparing coastal mangrove ecosystems for the effects of climate change will find this information useful.

Although our model estimates mangrove extent fairly well, the main limitation to this study is the lack of up-to-date data for the study area e.g., 2020 data and high-resolution images (e.g., 10m) as at the time of this analyses. Another drawback is that only uniform vegetation was taken into account. To investigate how these species interact with one another and whether zoning happens as indicated in the literature, more vegetation types could be added (Alongi, 2002; Liu et al., 2018).

It is important to mention that the hydrodynamic model for this study was calibrated with water surface elevation from a single station outside the study domain. In the future, the model will be calibrated with not only water surface elevation from the location but also with current velocity. This will help inform further research that will also take longer-term simulation into account.

Recommendations

Based on the findings of this study, it is advised that the government should develop a conscious management strategy that goes beyond meeting immediate community needs and includes current and alternative livelihood strategies, sustainable resource management systems, and sustained public awareness on mangrove services and their value under climate change. In areas where degradation has taken place, it should be encouraged to continually replant mangrove propagules.

To promote resilience and adaptation, rules that protect at-risk coastal communities must be upheld. These rules control illicit mining, indiscriminate sand mining, selective logging and deforestation, as well as the spread of settlement into low-lying and flood-prone areas. The reduction of non-climate

stressors such as pollution, deforestation and land conversion are therefore recommended as adaptation options to enhance the resilience of the existing ecosystem. Reducing non-climate stressors can help to build the resilience of ecosystems by lowering the burden of existing stressors and enabling them to better cope with the additional stresses imposed by climate change. For example, reducing deforestation and land conversion can help to maintain the integrity of ecosystems and reduce the risk of habitat loss and fragmentation.

It is advised that the government of Ghana implements a deliberate management plan to reduce GHG emissions and work with the university to create a database that includes information on rivers (such as water levels, currents, bathymetry, and water quality), land (such as topography, land use, and land cover), estuaries (such as water quality, water levels, and rivers), wetlands (such as area, biodiversity, and vegetation), and nearshore (such as area, water levels/tide changes, land use, etc.) in order to facilitate more coastal research. In other words, more measurement and surveying stations ought to be set up at various points along Ghana's coast.

References

Aerts, J.C., Wouter B.W.J, Emanuel K, Lin N, de Moel H, & Michel-Kerjan E.O, (2014). Evaluating flood resilience strategies for coastal megacities. *Science*, 344, 473–475, https://doi.org/ 10.1126/ science. 1248222.

Aheto, D.W., Aduomih, A.A.O. & Obodai, E.A., (2011). Structural Parameters and Above-ground Biomass of Mangrove Tree Species around the Kakum River Estuary of Ghana. *Annals of Biological Research*, 2 (3), 504-514.

Aicardi, I., Chiabrando, F., Grasso, N., Lingua, A. M., Noardo, F., & Spano, A. (2016). UAV Photogrammetry with Oblique Images: First Analysis on Data Acquisition and Processing. ISPRS International Archives of the Photogrammetry, *Remote Sensing and Spatial Inf. Sci.*

Aja, D., Eyasu, E. & Ota, H.O., (2019). Flood risk zone mapping using rational model in a highly weathered Nitisols of Abakaliki Local Government Area, Southeastern Nigeria, *Geology, Ecology, and Landscapes,* https://doi.org/10.1080/24749508.2019.1600912

Alizad, K., Hagen, S.C., Morris, J. T., Bacopoulos, P., Bilskie, M. V., Weishampel, J., & Medeiros, S. C. (2016a). A coupled, two-dimensional hydrodynamic-marsh model with biological feedback, *Ecological Modeling,*327,29 43, doi:10. 1016/j.e colm odel. 2016. 01.013.

Alizad, K., Hagen, S.C., Morris, J. T., Bacopoulos, P., Bilskie, M. V., Weishampel, J., & Medeiros, S. C. (2016b). Coastal wetland response

to sea-level rise in a fluvial estuarine system, *Earth's Future*, 4, 483–497, doi:10. 1002/ 2016 EF000385.

Alongi, D. M. (2008). Mangrove forests: resilience, protection from tsunamis, and responses to global climate change. Estuarine, *Coastal and Shelf Science* **76**(1): 1-13.

Alongi, D. M. (2012). Carbon sequestration in mangrove forests. *Carbon Management* **3**: 313-322.

AMN/RAM, (2009). A decade of mangrove reforestation in Africa (1999-2009): Serie 1: An assessment in five West African Countries: Benin, Ghana, Guinea, Nigeria and Senegal/ Une décennie de reboisement de mangrove en Afrique: Serie 1: Evaluations dans cinq pays en Afrique de l'Ouest: Benin, Ghana, Guinea, Nigeria and Senegal. African Mangrove Network/ Réseau Africain pour la conservation de la Mangrove.144pp.

Armah, A.K., Diamé, A., Ajonina, G. & Kairo, J. (2009). Protecting mangroves: The role and work of the African Mangrove Network (AMN). *FAO Nature and Fauna* 24(1), 26-29.

Arns, A., Dangeldorf, S., Jensen, J., Talke, S., Bender, J., & Pattiaratchi, C. (2017). Sea-level rise induced amplification of coastal protection design heights. *Sci. Rep.* 7, 40171.

Asbridge, E. (2018). Mangrove Response to Environmental Change in Northern Australia, A dissertation submitted to department of biological, earth and environmental sciences, Faculty of science, university of new south wales, Australia

Asbridge, E., Lucas, R., Accad, A., & Dowling, R. (2015). Mangrove response to environmental   changes predicted under varying climates: Case studies from Australia. *Current Forestry Reports*, 1(3), 178-194.

Atkinson, J., Smith, J.M., Bender, C. (2013). Sea-Level Rise Effects on Storm Surge and Nearshore Waves on the Texas Coast: Influence of Landscape and Storm Characteristics. J. Waterway, Port, Coastal, *Ocean Engineering*, 139, 98-117.

Attarchi, S., & Gloaguen, R. (2014). Classifying Complex Mountainous Forests with L-Band SAR and Landsat Data Integration: A Comparison among Different Machine Learning Methods in the Hyrcanian Forest. *Remote Sensing, 6*, 3624-3647.

Ayman, A.H, Olena, D., Islam, A.E., & Gunter, M. (2017). Integration of SAR and Optical Remote Sensing data for mapping of mangroves extents. In: From Science to Society: The Bridge provided by Environmental Informatics. (Ed. Benoît Otjacques, Patrik Hitzelberger, Stefan Naumann, Volker Wohlgemuth) Germany: *Shaker Verlag GmbH*, p. 1 – 8.

Babcock, C., Finley, A.O., Bradford, J.B., Kolka, R., Birdsey, R., & Ryan, M.G. (2015). LiDAR based prediction of forest biomass using hierarchical models with spatially varying coe_cients. *Remote Sensing Environment*, 169, 113–127.

Balmford, A., & Bond W., (2005). Trends in the state of nature and their implications for human well-being. Ecology Letters 8: 1218–1234.

Barbier, E. B., S. D. Hacker, C. Kennedy, E. A. Kocj, A. C. Stier & Silliman B. R. (2011). The value of estuarine and coastal ecosystem services. *Ecological Monographs* 81(2): 169-193.

Barenblitt, A., & Fatoyinbo, L. (2020a). Intro to SDG 6.6 and Remote Sensing Techniques for Mangroves. NASA's Applied Remote Sensing Training Program.

Barenblitt, A., & Fatoyinbo, L. (2020b). Mangrove Extent Mapping and Time Series. NASA's Applied Remote Sensing Training Program.

Berger, U., & Hildenbrandt, H. (2000). A new approach to spatially explicit modelling of forest dynamics: spacing, ageing and neighbourhood competition of mangrove trees. *Ecological Modeling,* 132, 287–302. doi:10.1016/S0304-3800(00)00298-2

Bilskie, M.V, Hagen, S.C, Medeiros, S. C, & Passeri, D.L. (2014). Dynamics of sea level rise and coastal flooding on a changing landscape. Faculty Bibliography2010s.5077.https://stars.library.ucf.edu/facultybib2010/5077.

Bilskie, M.V., & Hagen S.C. (2013). Topographic accuracy assessment of bare earth lidar-derived unstructured meshes, Adv. *Water Resource,* 52,165–177, doi:10.1016/j.adv watres. 2012.09.003.

Blasco, F., Aizpuru, M. & Besnehard, J. (2019). Mangroves, Ecology. Encyclopedia of Coastal Science, Springer Nature Switzerland AG Finkl. W. Charls and Makowski Christopher (eds.) https://doi.org/10.1007/978-3-319-93806-6

135

Boateng, I., Wiafe, G., & Jayson-Quashigah P. (2017). Mapping Vulnerability and Risk of Ghana's Coastline to Sea Level Rise, *Marine Geodesy*, 40:1,23-39, DOI:10. 1080/0149 0419. 2016. 1261745

Breithaupt, J. L., Smoak J. M., Smith, T. J., Sanders, C. J. & Hoare, A. (2012). Organic carbon burial rates in mangrove sediments: Strengthening the global budget. *Global Biogeochemical Cycles* 26(3).

Brown S., Abiy S.K., & Robert J.N. (2011). Sea-Level Rise and Impacts in Africa, 2000 to 2100. School of Civil Engineering and the Environment University of Southampton, SO17 1BJ, UK.

Brown, I., Mwansasu, S., & Westerberg, L.O. (2016). L-Band Polarimetric Target Decomposition of Mangroves of the Rufiji Delta, Tanzania. *Remote Sensing*, 8, 140.

Brown, S. & Iverson L.R. (1992). *Biomass estimates for tropical forests. World Resources Review*, 4, 366-384.

Bunting, P., Rosenqvist, A., Lucas, R., Rebelo, L.M., Hilarides, L., Thomas, N., Hardy, A., Itoh, T., Shimada, M., & Finlayson, C. (2018). The Global Mangrove Watch—A New 2010 Global Baseline of Mangrove Extent. *Remote Sensing.*, 10, 1669.

Buttolph, A.M., Reed, C.W., Kraus, N.C., Ono, N., Larson, M., Camenen, B., Hanson, H., Wamsley, T., & Zundel, A.K. (2006). Two-dimensional depth- averaged circulation model CMS-M2D: Version 3.0, Report 2: Sediment transport and morphology change. *Tech.Rep. ERDC/CHL TR-06-9*, U.S. Army Engineer Research and De-velopment Center, Coastal and Hydraulic Engineering, Vicksburg, MS.

Carreiras, J.M.B, Melo, J.M., & Vasconcelos, M.J. (2013). Estimating the above-ground biomass in Miombo Savanna woodlands (Mozambique, East Africa) using L-band synthetic aperture radar data. *Remote Sensing,* 5(4):1524–1548.

Carrivick, J., Smith, M., & Quincey, D. (2016). Structure from Motion in the Geosciences; John Wiley & Sons, Ltd.: Hoboken, NJ, USA.

Chang, S. E., B. J. Adams, J. Alder, P. R. Berke, R. Chuenpagdee, S. Ghosh & Wabnitz, C. (2006). Coastal ecosystems and tsunami protection after the December 2004 Indian Ocean Tsunami. Earthquake Spectra 22(S3): 863-887.

Change (2007). Impacts, Adaptation and Vulnerability. Contribution of Working Group II to the Fourth Assessment Report of the Intergovernmental Panel on Climate Change. CambridgE, UK: Cambridge university press. *Change*, 63-82. *International Journal of Water Governance,* 3(4), 25-46. doi:10.7564/15-IJWG90

Chapman, V.J. (1976). Mangrove vegetation. Cramer, Vaduz

Chave, J., Andalo, C., Brown, S., Cairns, M.A., Chambers, J.Q., Eamus, D., Fölster, H., Fromard, F., Higuchi, N., Kira, T., Lescure, J.P., Nelson, B.W., Ogawa, H., Puig, H., Riéra, B., & Yamakura, T. (2005). Tree allometry and improved estimation of carbon stocks and balance in tropical forests *Oecologia* 145 87–99. DOI: 10.1007/s00442-005-0100-x

Chen, B., Xiao, X., Li, X., Pan, L., Doughty, R., Ma, J., Dong, J., Qin, Y., Zhao, B., & Wu, Z. (2017). A mangrove forest map of China in 2015: Analysis of time series Landsat 7/8 and Sentinel-1A imagery in Google

Earth Engine cloud computing platform. *ISPRS Journal of Photogrammatry and Remote Sensing,* 131, 104–120.

Chen, L., Wang W., Zhang, Y. & Lin, G. (2009). Recent progresses in mangrove conservation, restoration and research in China. *Journal of Plant Ecology* 2, 45-54.

Chen, R., & Twilley, R.R. (1998). A gap dynamic model of mangrove forest development along gradients of soil salinity and nutrient resources. *Journal of Ecology.* 86, 37–51. doi:10.1046/j.1365-2745.1998.00233.x

Chiu, C.Y., Lee, S.C., Chen, T.H. & Tian G. (2004). Denitrification associated N loss in mangrove soil. Nutrient Cycling in Agroecosystems 69, 185-189.

Clarke, L., Edmonds, J., Jacoby, J., Pitcher, H., Reilly, J., Richels, R., & Parson, E. (2007). Scenarios of Greenhouse Gas Emissions and Atmospheric Concentrations. A Report by the U.S. Climate Change Science Program and the Subcommittee on Global Change Research. Synthesis and Assessment Product 2.1. Climate Change Science Program (CCSP), Department of Energy, Office of Biological and Environmental Research.

Comley, B.W.T. & McGuinness, K.A. (2005). Above and below ground biomass, and allometry, of four common northern Australian mangroves. *Australian Journal of Botany,* 53, 431–436. doi:10.1071/ BT04162.

Conley, L. M., R. I. Dick and L. W. Lion (1991) An assessment of the root zone method of wastewater treatment. *Res. J. War. Pollut* 63(3), 239-247.

138

Davis, R.A., (1985). Beach and nearshore zone. In: DAVIS, R.A. (ed.), Coastal Sedimentary Environments. New York: Springer-Verlag, 379-4.

De Santiago, F.F., Kovacs, J.M., & Lafrance, P. (2013). An object-oriented classification method for mapping mangroves in Guinea, West Africa, using multi-polarized ALOS PALSAR L-band data. *International Journal of Remote Sensing*, 34, 563–586.

Dellepiane, S., de Laurentiis, R., & Giordano, F. (2004). Coastline Extraction from SAR Images and a Method for the Evaluation of the Coastline Precision. *Pattern Recognition Letters, 25*, 1461–1470.

Di Baldassarre, G., Schumann, G., & Bates, P.D. (2009). A technique for the calibration of hydraulic models using uncertain satellite observations of flood extent. *Journal of Hydrology, 367*(3-4), 276–282. doi:10.1016/j.jhydrol.2009.01.020

Diniz, C., Cortinhas, L., Nerino, G., Rodrigues, J., Sadeck, L., Adami, M., & Souza-Filho, B.P. (2019). Mangrove Status: Three Decades of Satellite Data Analysis. *Remote Sensing*, 11, 808.

Dodgson, N.A. (1992). Image Resampling; University of Cambridge, Computer Laboratory: Cambridge, UK, p. 264. DOI https://doi.org/10.5670/oceanog.2017.317

Donato, D. C., Kauffman, B., Murdiyarso, D., Kurnian, S., Stidham M. & Kanninem, M. (2011). Mangroves among the most carbon-rich forests in the tropics. *Nature Geoscience*, 4, 293-297.

Duarte, C.M., Marbà, N., Gacia, E., et al. (2010). Seagrass community metabolism: assessing the carbon sink capacity of seagrass

meadows. *Global Biogeochemical Cycle,* 24, GB4032; doi: 10. 1029/ 2010GB003793.

Duke, N.C., Ball, M., & Ellison, J.C. (1998). Factors influencing biodiversity and distribution gradients in mangroves. *Global Ecological Biogeography Letters,* 1(7), 27–47.

Egbert, G.D., & Erofeeva, S.Y. (2002). Efficient inverse modeling of barotropic ocean tides, *Journal of Atmosphere and Ocean Technology,* 19 (2), 183–204, doi:10.1175/1520-0426.

Egbert, G.D., Bennett, A.F. & Foreman, M.G.G. (1994), TOPEX/POSEIDON tides estimated using a global inverse model, *Journal of Geophysical Research and Oceans*, 99 (C12), 24821–24852, doi: 10.1029/ 94J C01 894.

Elizabeth, M., Gail, L.C, Bouillon S., Rodney, S., Björk M., Carlos, M.D., Catherine, E.L., William, H.S. & Brian, R.S. (2011). A blueprint for blue carbon: toward an improved understanding of the role of vegetated coastal habitats in sequestering CO_2 . *Frontiers in Ecology and the Environment*, 9(10), 552-560.

Ellison, A., Farnsworth, E., & Moore, G. (2015). Rhizophora Mangle. The IUCN Red List of Threatened Species.

Ellison, J.C. (1993). Mangrove retreat with rising sea-level, Bermuda. *Estuarine, Coastal and Shelf Science, 37*(1), 75-87.

Ellison, J.C. (2009). Geomorphology and sedimentology of mangroves.

El- Shahat, S., Abbas, M.E., Tarek, A.E., & Safaa, A.G. (2019). Vulnerability assessment of African coasts to sea level rise using GIS and remote

sensing. Environment, Development and   Sustainability. https://doi.org/10. 1007/s10668-020-00639-8

Ericson, J., Vorosmarty, C., Dingman, S., Ward, L., & Meybeck, M. (2006). Effective sea level rise and deltas: causes of change and human dimension implications. *Journal of Planetary.*

Erika, P., Amber M., Juan L.T.P., & Sean M. (2020).   Forest   Mapping and Monitoring with SAR Data: Time Series Analysis. NASA's Applied Remote Sensing Training Program

ESA. (2012). *Space in Images: mean sea level trends*. Retrieved November 16, 2016, from European Space Agency: http://www.esa.int/ spaceinimages/Images/2012/09/Mean_sea_level_ trends

Ezer, T., & Atkinson, L.P. (2014). Accelerated flooding along the U.S. East Coast: On the impact of sea-level rise, tides, storms, the Gulf Stream, and the North Atlantic Oscillations. Earth's Future, 2, 362–382.

Fabrizio, A., Giovanni, D.F., Valeria, L.P., Lorenzo, M., Giovanni, S., Marco, A., Davide, B., Sandro, C., Gabriele, L., Stefano, F., Antonella, M., Marcello, P., Giovanni, R., Giovanni, S. & Giuseppe, M. (2020). Relative Sea-Level Rise and Potential Submersion Risk for 2100 on 16 Coastal Plains of the Mediterranean Sea. *Water*, 12, 2173, https://doi.org/10.3390/ w12082173.

FAO (2007) The World's Mangroves 1980-2005. FAO Forestry Paper Rome: Forest Resources Division: 77.

Fatoyinbo, T. E., & Simard, M. (2013). Height and biomass of mangroves in Africa from ICESat/GLAS and SRTM. *International Journal of Remote Sensing* 34, 668–681. doi:10.1080/01 431161. 2012.712224

Fatoyinbo, T., Feliciano, E.A., Lagomasino, D., Lee, S.K., & Trettin, C. (2018). Estimating mangrove aboveground biomass from airborne LiDAR data: a case study from the Zambezi River delta. *Environmental Research Letters,* 13, 025012. https://doi.org/10.1088/1748-9326/aa9f03.

Friends of the Nation (2014), Assessment of flora and fauna of ecological and socioeconomic significance within the Anlo Beach Wetland Complex for improved management and livelihood outcomes, Parks and Gardens, Adiembra, 60 pp.

Friess, D.A., Spencer, T., Smith, G.M., Möller, I., Brooks, S.M., & Thomson, A.G. (2012). Remote sensing of geomorphological and ecological change in response to saltmarsh managed realignment, The Wash, UK. *International Journal of Applied Earth Observation and Geoinformation*, 18, 57-68. http://doi.org/10.1 016/j.jag .2012.01.016

Fromard, F., Puig, H., Mougin, E., Marty, G., Betoulle, J.M., & Cadamuro, L. (1998). Structure, above ground biomass and dynamics of mangrove ecosystems: new data from French Guiana. *Oecologia* 115:39–53.

Ganju, K.N., Mark, J.B., Brenda, R., Alfredo, L., Aretxabaleta, P.B., Jason, S.G., Lora, A., Harris, S.J., Lake, G.M., James, O., David, K.R., Richard, P., Signell, J.M., Testa, J.M., & Vaudrey P. (2016). Progress and Challenges in Coupled Hydrodynamic, *Ecological Estuarine Modeling Estuaries and Coasts*, 39:311–332 DOI 10.1007/s12237-015-0011-y.

Gedan, K.B., Kirwan, M.L., Wolanski, E., Barbier, E.B., & Silliman, B.R. (2011). The present and future role of coastal wetland vegetation

142

in protecting shorelines: Answering recent challenges to the paradigm. *Climate Change*, 106, 7–29.

Geselbracht, L.L., Freeman, K., Birch, A.P., Brenner, J., & Gordon, D.R. (2015). Modeled Sea Level Rise Impacts on Coastal Ecosystems at Six Major Estuaries on Florida's Gulf Coast: Implications for Adaptation Planning. *PLoS ONE*   10(7):e0132079. doi:10.1371/journal.pone. 0132079.

Giosan, L., Syvitski, J., Constantinescu, S., & Day, J. (2014). Protect the world's deltas. *Nature*, 516(7529), 31–33,https://doi.org/ 10.1038/ 516031a.

Giri, C., Long, J., Abbas, S., Murali, R.M., Qamer, F.M., Pengra, B., & Thau, D. (2015). Distribution and dynamics of mangrove forests of South Asia. *Journal of Environmental Management*, 148, 101–111.

Giri, G., Ochieng, E., Tieszen, L. L., Zhu, Z., Singh, A., Loveland, T., Masek, J., & Duke, N. (2011). Status and distribution of mangrove forests of the world using earth observation satellite data. *Global Ecology and Biogeography*, 20, 154–159, doi:10.1111/J.1466-8238. 2010.00584.X.

Gordon, N.A, Felix, A.A., Abdoulaye, D., & Ayaa, K.A. (2015). Overview of Experience of Mangrove Reforestation in West And Central Africa. 38th Annual   Conference of Forestry Association of Nigeria (FAN).

Gornitz, V., Couch, S., & Hartig, E.K. (2001). Impacts of sea level rise in the New   York City metropolitan area. *Global Planet Change*, 32, 61–88.

Hagen, S.C., Morris, J.T., Bacopoulos, P., & Weishampel, J.F. (2013). Sea-Level Rise Impact on a Salt Marsh System of the Lower St. Johns

River, *American Society of Civil Engineers*, DOI: 10.1061/(ASCE) WW.1943-5460.0000177.

Hamilton, L.S., & Snedaker, S.C. (1984). Handbook for mangrove area management. East-West Center, Honolulu

Hamilton, S.E. & Casey, D. (2016). Creation of a high spatio- temporal resolution global database of continuous mangrove forest cover for the 21st century (CGMFC- 21). *Global Ecology and Biogeography* 25(6): 729-738.

Held, A., Ticehurst, C., Lymburner, L., & Williams, N. (2003). High resolution   mapping of tropical mangrove ecosystems using hyperspectral and radar remote sensing. *International Journal of Remote Sensing*, 24, 2739–2759. doi:10.1080/0143116031 0000 66 323

Hoppe-Speer, S.C.L., Adams, J.B., & Bailey, D. (2015) Present state of mangrove forests along the Eastern Cape coast, South Africa. *Wetland Ecological Management,* 23, 371–383.

Hu, T., Su, Y., Xue, B., Liu, J., Zhao, X., Fang, J., & Guo, Q. (2016). Mapping Global   Forest Aboveground Biomass with Spaceborne LiDAR, Optical Imagery, and Forest Inventory Data. *Remote Sensing*. 8, 565.

Hughes, A.R., Williams, S.L., Duarte, C.M., Heck, K.L., & Waycott, M. (2009). Associations of concern: declining seagrasses and threatened dependent species. *Frontiers in Ecology and the Environment*, 7(5), 242-246.

Hunt, S., Bryan, K.R., & Mullarney, J.C. (2015). The influence of wind and waves on the existence of stable intertidal morphology in meso-tidal estuaries.   *Geomorphology,*   228,   158–174. doi:10.1016/j.geomorph.2014.09.001.

Hutchison, J., Manica, A., Swetnam, R., Balmford, A., & Spalding, M. (2014). Predicting Global   Patterns in Mangrove Forest Biomass: Global patterns in mangrove biomass. *Conservation Letters.*, 7, 233–240.

Idier, D., Paris, F., Le Cozannet, G., Boulahya, F., & Dumas, F. (2017). Sea-level rise impacts on the tides of the European Shelf. *Continental Shelf Research,* 137, 56–71.

Iglesias, I., Paulo, A., Ana, B. & Luísa, B. (2019). Modelling the Main Hydrodynamic Patterns in Shallow Water Estuaries: The   Minho Case   Study.   Water,   11,   1040;   doi:10.3390/   w11051040. www.mdpi.com/journal/water

Intergovernmental Panel on Climate Change (IPCC), (2007a). *Natural System responses to climate Change Drivers.* Working group 11: Impacts, Adaptation and Vulnerability. Inter-governmental   panel   on   Climate Change. Retrieved   from http://www.ipcc.ch/publications_and_data/ar4/wg1/en/ch5s5-5-2-2.html

Intergovernmental Panel on Climate Change (IPCC), (2007b). *Regional Impacts   of   Climate   Change.* IPCC.   Retrieved   from https://www.ipcc.ch/ipccreports/sres/regional/503.htm, November 17, 2015,

Intergovernmental Panel on Climate Change (IPCC), (2014). *Climate Change 2014: Synthesis Report.* Geneva, Switzerland.

Intergovernmental Panel on Climate Change (IPCC). (2021). IPCC AR6 Sea-Level Rise   Projections. Version 20210809. PO.DAAC, CA, USA. Dataset accessed[2021-11-18] at https://podaac.jpl.nasa.gov /announcements/2021-08-09-Sea-level-projections-from-theIPCC-6th-Assessment-Report.

Irene, B.S, José, M.P, Jorge, T.S, Francisco, J.M.C & Francisca, L.G, (2015). Spatial Quality Evaluation of Resampled Unmanned Aerial Vehicle-Imagery for Weed Mapping. *Sensors*, 2015, 15, 19688-19708; doi: 10.3390/s150819688.

Jhonnerie, R., Siregar, V.P., Nababan, B., Prasetyo, L.B., & Wouthuyzen, S. (2015). Random Forest Classification for Mangrove Land Cover Mapping Using Landsat 5 TM and Alos Palsar Imageries. *Procedia Environmental Sciences*, 24:215-221.https://doi.org/ 10.1016/j. proenv. 2015.03.028.

Jongejan, R., Ranasinghe, R., Wainwright, D., Callaghan, D.P., & Reyns, J. (2016).   Drawing the line on coastline recession risk. *Ocean and Coastal Management*, 122, 87–94.

José, F.R, Patricia, M.S, Steven, S., Neil, S. & Gerardo, R. (2017). Potential increase in coastal wetland vulnerability to sea-level rise suggested by considering hydrodynamic attenuation effects. *Nature communications,* 8, 16094, DOI:10.1038/ncomms16094.

Jung, C.H., Hamski, J., Durand, M., Alsdorf, D., Hossain, F., Lee, & Hasan, K.H. (2010). Characterization of complex fluvial systems using remote

146

sensing of spatial and temporal water level variations in the Amazon, Congo, and Brahmaputra Rivers. *Earth Surface Processes and Landforms, 35*(3), 294-304. doi:10.1002/esp.1914

Justyna, J. (2019). UAS for Wetland Mapping and Hydrological Modeling. *Remote Sensing,* 2019, 11, 1997; doi:10.3390/rs11171997

Kamal, M., Phinn, S., & Johansen, K. (2015). Object-Based Approach for Multi-Scale Mangrove Composition Mapping Using Multi-Resolution Image   Datasets. *Remote Sensing,* 7, 4753–4783.

Kennedy H, Beggins J, Duarte CM, et al (2010). Seagrass sediments as a global carbon sink: isotopie constraints. *Global Biogeochemical Cycle,* 24; doi: 10.1029/2010GB003848.

Kenward, T. (2000). Effects of digital elevation model accuracy on hydrologic predictions. *Remote Sensing of Environment,* 74, 432–444.

Kim, J., Lu, Z., Lee, H., Shum, C. K., Swarzenski, C. M., Doyle, T. W., & Baek, S.H. (2009). Integrated analysis of PALSAR/Radarsat-1 InSAR and ENVISAT altimeter data for mapping of absolute water level changes in Louisiana wetlands. *Remote Sensing of Environment, 113*(11), 2356-2365.

Kinnmark, I. (1985). The shallow water wave equations: formulation, analysis and application. In: Brebbia, C.A., Orszag, S.A. (Eds.), Lecture Notes in Engineering, vol. 15. Springer, New York, pp. 1–187.

Kirwan, M.L., & Megonigal, J.P. (2013). Tidal wetland stability in the face of human impacts and sea-level rise. *Nature, 504,* 53-60.

147

Kolar, R.L., Westerink, J.J., Cantekin, M.E., & Blain, C.A. (1994). Aspects of nonlinear simulations using shallow-water models based on the wave continuity equation. *Computational Fluids*, 23 (3), 523–538.

Kovacs, J.M., de Santiago, F.F., Bastien, J., & Lafrance, P. (2010). An Assessment of Mangroves in Guinea, West Africa, using a Field and Remote Sensing Based Approach. *Wetlands*, 30, 773–782.

Krauss, K.W., Cahoon, D. R., Allen, J. A., Ewel, K. C., Lynch, J. C., & Cormier, N. (2010).   Surface Elevation Change and Susceptibility of Different Mangrove Zones to Sea-Level   Rise   on   Pacific   High Islands of Micronesia. *Ecosystems, 13*(1), 129-143.

Krauss, K.W., Lovelock, C.E., McKee, K.L, López-Hoffman, L., Ewe, S.M.L., & Sousa, W.P. (2008). Environmental drivers in mangrove establishment and early development: a review. *Aquat. Bot.* 89, 105–127. doi:10.1016/j.aquabot.2007.12.014.

Kuenzer, C., & Tuan, V.Q. (2013). Assessing the ecosystem services value of Can Gio Mangrove   Biosphere   Reserve: Combining   earth-observation- and household-survey-based analyses. *Appl. Geogr.*, 45, 167–184.

Kuenzer, C., van Beijma, S., Gessner, U., & Dech, S. (2014). Land surface dynamics and environmental challenges of the Niger Delta, Africa: Remote sensing-based analyses spanning three decades (1986–2013). *Appl. Geogr.*, 53, 354–368.

Laffoley, D. & Grimsditch, G. (2009) The management of natural coastal carbon sinks. Gland, Switzerland: IUCN (Eds).

Lagomasino, D., Fatoyinbo, T., Lee, S., Feliciano, E., Trettin, C. & Simard, M. (2016). A comparison of mangrove canopy height using multiple independent measurements from land, air, and space. *Remote Sensing.* 8 327.

Lagomasino, D., Fatoyinbo, T., Lee, S., Feliciano, E., Trettin, C., Shapiro, A., & Mangora, M.M. (2019). Measuring mangrove carbon loss and gain in deltas. *Environmental Research Letters*, 14, 025002.

Lahmann, E.J. (1988). Effects of different hydrological regimes on the productivity of Rhizophora mangle L. A case study of mosquito control impoundments at Hutchinson Island. Saint Lucie County, Florida. PhD thesis, University of Miami, Miami

Lee, S.Y., Primavera, J.H., Dahdouh-Guebas, F., McKee, K., Bosire, J.O., Cannicci, S., Diele, K., Fromard, F., Koedam, N., & Marchand, C. (2014). Ecological role and services of tropical mangrove ecosystems: A reassessment: Reassessment of mangrove ecosystem services. Glob. *Ecological Biogeography*, 23, 726–743.

Lesser, G., Roelvink, J., Van Kester, J., & Stelling G. (2004). Development and Validation of a Three-Dimensional Morphological Model. *Coastal Engineering*, 51, 883–915.

Li, H. & Brown, M.E. (2019). Modeling Sea Level Change Using the Coastal Modeling System. ERDC/CHL CHETN-IV-119. Vicksburg, MS: U.S. Army Engineer Research and Development Center. http:// dx. doi.org /10.21079/11681/33204.

Lim, K., Treitz, P., Wulder, M., St-Onge, B., & Flood, M. (2003). LiDAR remote sensing of forest structure. *Prog. Phys. Geogr. Earth Environ.,* 27, 88–106.

Lin, L., Demirbilek, Z., Mase, H., Zheng, J., & Yamada, F. (2008). CMS-Wave: a nearshore   spectral wave processes model for coastal inlets and navigation projects. *Tech. Report ERDC/CHL TR-08-13.* Vicksburg, MS: U.S. Army Engineer Research and Development Center.

Lovelock, C.E., Cahoon, D.R., Friess, D.A., Guntenspergen, G. R., Krauss, K. W., Reef, R., & Triet, T. (2015). The vulnerability of Indo-Pacific mangrove forests to sea-level rise. *Nature, 526,* 559-563.

Lucas, R., Rebelo, L., Fatoyinbo, L., Rosenqvist, A., Itoh, T., Shimada, M., Simard, M., Pedro, W.S., Nathan, T., Carl, T., Arnon, A., Joao, C., & Lammert, H. (2014). Contribution of L-band SAR to systematic global mangrove monitoring. *Marine and Freshwater Research*, 65, 589–603 http://dx.doi.org/10.1071/MF13177.

Lucas, R.M., Mitchell, A.L., Rosenqvist, A., Proisy, C., Melius, A., & Ticehurst, C. (2007). The potential of L-band SAR for quantifying mangrove characteristics and change: case studies from the tropics. Aquatic Conservation: *Marine and Freshwater Ecosystems,* 17, 245–264. doi:10.1002/AQC.833.

Luettich, R.A., & Westerink, J.J. (2006a). ADCIRC: A Parallel Advanced Circulation Model   for   Oceanic,   Coastal   and   Estuarine Waters;<http://adcirc.org/document/ADCIRC_title_page.html>.

Luettich, R.A., & Westerink, J.J. (2006b). Formulation and Numerical Implementation of the 2D/3D ADCIRC Finite Element Model, Version 44.XX. <http://adcirc.org/ document/ADCIRC_title_page.html>.

Lugo, A.E., Twilley, R.R., & Patterson-Zucca, C. (1980). The role of black mangrove forests in the productivity of coastal ecosystems in south Florida. Report to E.P.A. Corvallis   Environmental   Research Laboratory, Corvallis.

Lynch, D.R., & Gray, W.G., (1979). A wave equation model for finite element tidal computations. *Comput. Fluids*, 7 (3), 207–228.

MacDonald, N.J., Davies, M.H., Zundel, A.K., Howlett, J.D., Lackey, T. C., Demirbilek, Z., & Gailani, J.Z. (2006). PTM: Particle Tracking Model; Report 1: Model theory, implementation, and example ap-plications. Coastal and Hydraulics Laboratory Technical Report ERDC/CHL-TR-06-20. Vicksburg, MS: U.S. Army Engineer Re-search and Development Center.

MacKay, H., Finlayson, C.M., Fernandez-Prieto, D., Davidson, N., Pritchard, D., & Rebelo, L.M. (2009). The role of earth observation (EO) technologies in supporting implementation of the Ramsar Convention on Wetlands. *Journal of Environmental Management*, 90, 2234–2242. doi:10.1016/J.JENVMAN.2008.01.019.

Mase, H., Oki, K., Hedges, T.S., & Li, H.J. (2005). Extended energy-balance-equation wave model for multidirectional random wave transformation. *Ocean Engineering*, 32(8-9), 961-985.

Mayaux, P., Holmgren, P., Achard, F., Eva H., Stibig, H.J. & Branthomme, A. (2005). Tropical Forest cover change in the 1990s and options for

future monitoring. Philosophical Transactions of the Royal Society of London B: *Biological Sciences,* 360(1454), 373-384.

Mazda, Y., Magi, M., Kogo, M. & Hong, P. N. (1997). Mangroves as a coastal protection from waves in the Tong King delta, Vietnam. *Mangroves and Salt marshes*, 1(2): 127-135.

Mcmanus, J. (2002). Deltaic responses to Changes in River Regimes. *marine Chemistry, 79,* 155 -170.

Medeiros, S., Hagen, S., Weishampel, J., & Angelo, J. (2015). Adjusting lidar-derived digital terrain models in coastal marshes based on estimated above ground biomass density, Remote Sens., 7 (4), 3507–3525, doi:10.3390/rs70403507.

Medeiros, S.C. (2012). Incorporating remotely sensed data into coastal hydrodynamic models: Parameterization of surface roughness and spatio-temporal validation of inundated area, Univ. of Central Florida, Orlando, Fla.

Medeiros, S.C., & Hagen, S.C. (2013). Review of wetting and drying algorithms   for numerical tidal flow models, *International Journal of Numerical Methods in Fluids*, 71 (4),473–487, doi:10.1002/fld.3668.

Mehvar, S., Filatova, T., Syukri, I., Dastgheib, A., & Ranasinghe, R. (2018). Developing a framework to quantify potential Sea level rise-driven environmental losses: a case study in Semarang coastal area, Indonesia. *Environ. Sci. Pol.* 89, 216–230.

Mendoza, E.T., & Jimenez, J.A. (2006). Storm-induced beach erosion potential on the Catalonian coast. *Journal of Coastal Research.* 48, 81–88.

Meselhe, E., Roelvink, D., Wackerman, C., Xing, F., & Thanh,V.Q. (2017). Modeling the process response of coastal and deltaic systems to human and global changes: Focus on the Mekong system. *Oceanography*, 30(3), 84–97, https://doi.org/10.5670/oceanog. 2017.317.

Midekisa, A., Holl, F., Savory, D.J., Andrade-Pacheco, R., Gething, P.W., & Bennett, A. (2017). Mapping land cover change over continental Africa using Landsat and Google Earth   Engine cloud computing. *PLoS ONE* 12(9): e0184926. https://doi.org/10.137 1/journal. pone.0184926

Militello, A., & Zundel, A.K. (2002). Coupling of regional and local circulation models ADCIRC and M2D, Coastal and Hydraulics Engineering Technical Note ERDC/CHL CHETN-IV-42, U.S. Army Engineer Research and Development Center, Vicksburg, MS.

Militello, A., Reed, C.W., Zundel, A.K., & Kraus, N.C. (2004). Two-dimensional depth-averaged circulation model M2D: Version 2.0, Report 1: Documentation and user's guide, ERDC/CHLTR-04-02, U.S. Army Engineer Research and Development Center, Vicksburg, MS.

Millenium Ecosystem Assessment (MEA) (2005). Ecosystems and Human Well- being: Wetlands and Water. Synthesis. (World Resources Institute: Washington DC.)

Miller, K.G., Kopp, R.E., Horton, B.P., Browning, J.V., & Kemp, A.C. (2013). A geological perspective on sea-level rise and its impacts along the U.S. mid-Atlantic coast. *Earth's Future*, 1, 3–18.

Ming, D., Zhou, T., Wang, M., & Tian, T. (2016). Land cover classification using random forest with genetic algorithm-based parameter optimization, *Journal of Applied Remote Sensing,* 10(3), 035021. doi: 10.1117/1.JRS.10.035021

Miththapala, S. (2008). Mangroves. Coastal Ecosystems. Colombo Sri Lanka, Ecosystems and Livelihoods Group Asia. **2**.

Miziński, B. & Niedzielski, T. (2017). Fully-automated estimation of snow depth in near real time with the use of unmanned aerial vehicles without utilizing ground control points. Cold Reg. Sci. Technol., 138, 63–72.

Mondal, P., Trzaska, S., & de Sherbinin, A. (2018). Landsat-Derived Estimates of Mangrove Extents in the Sierra Leone Coastal Landscape Complex during 1990–2016. *Sensors,* 18, 12.

Morim, J., Hemer, M., Wang, X.L., et al., (2019). Robustness and uncertainties in global multivariate wind-wave climate projections. *Nat. Clim. Chang.* 9, 711–718. Ranasinghe,

Morris, J. (2007). Ecological engineering in intertidal salt marshes, *Hydrobiologia*, 577(1),161– 168, doi:10.1007/s10750-006-0425-4.

Morris, J.T., Sundareshwar, P.V., Nietch, C.T., Kjerfve, B., & Cahoon, D.R. (2002), Responses of coastal wetlands to rising sea level, *Ecology*, 83 (10), 2869–2877, doi:10.1890/0012-9658.

Morris, J.T., Sundberg, K., & Hopkinson, C.S. (2013). Salt marsh primary production and its responses to relative sea level and nutrients in estuaries at Plum Island, Massachusetts, and NorthInlet, South

Carolina, USA, Oceanography, 26 (3), 78–84, doi:10.5670/ oceanog. 2013.48.

Mousavi, M.E., Irish, J.L., Frey, A.E., Olivera, F., & Edge, B.L. (2011). Global warming and hurricanes: The potential impact of hurricane intensification and sea level rise on coastal flooding. *Climate Change*, 104(3-4), 575-597.

Murdiyarso, D., Purbopuspito, J., Kau_man, J.B., Warren, M.W., Sasmito, S.D., Donato, D.C., Manuri, S., Krisnawati, H., Taberima, S., & Kurnianto, S. (2015). The potential of Indonesian mangrove forests for global climate change mitigation. *Natural Climate Change*, 5, 1089-1092.

Musa, Z., Popescu, I., & Mynett, A. (2015). A review of applications of satellite SAR, optical, altimetry and DEM data for surface water modelling, mapping and parameter estimation. *Hydrology and Earth Sustems Sciences (HESS)*, 19, 3755-3769. doi:10.5194/hess-19-3755-2015.

Mwita, E., Menz, G., Misana, S., & Nienkemper, P. (2012). Detection of Small Wetlands with Multi Sensor Data in East Africa. *Advances in Remote Sensing*, 1, 64-73. https://doi.org/10.4236/ars.2012.13007

Næsset, E., Gobakken, T., Solberg, S., Gregoire, T.G., Nelson, R., Ståhl, G., & Weydahl, D. (2011) Model-assisted regional forest biomass estimation using LiDAR and InSAR as auxiliary data: A case study from a boreal forest area. Remote Sens. Environ. 115, 3599–3614.

Nascimento, W.R., Souza-Filho, P.W.M., Proisy, C., Lucas, R.M., & Rosenqvist, A. (2013). Mapping changes in the largest continuous

Amazonian mangrove belt using object-based classification of multisensory satellite imagery. *Estuarine, Coastal and Shelf Science* 117, 83–93. doi:10.1016/J.ECSS.2012.10.005

Nathan, T., Peter, B., Richard, L., Andy, H., Ake, R., & Temilola, F. (2018). Mapping Mangrove Extent and Change: A Globally Applicable Approach. *Remote Sensing,* 10:1466. doi:10.3390/rs10091466

Nellemann, C., Corcoran, E., Duarte, C.M., et al. (Eds). (2009). Blue car- bon. A rapid response assessment. GRID-Arendal: United Nations Environment Programme. ISBN: 978-82- 7701-060.

Neukermans, G., Dahdouh-Guebas, F., Kairo, J. G., & Koedam, N. (2008). Mangrove species   and stand mapping in Gazi Bay (Kenya) using Quickbird satellite imagery. *Journal of Spatial Science* 53, 75–86. doi:10.1080/14498596.2008.9635137.

Niang-Diop, I., Bosch, H., Burton, I., Khan, S. R., Lim, B., & North, N. (Eds.) (2005). Formulating an adaptation strategy. In B. Lim, E. Spanger-Siegfried, I. Burton, E. Malone, & S. Huq, *Adaptation policy frameworks for climate change: Developing strategies, policies   and measures* (pp. 183–204). Cambridge, UK, 2004: United Nations Development Programme (UNDP) and Cambridge University Press.

Nicholls, R., Wong, P., Burkett, V., & Codi, J. (2007). Coastal systems and low-lying areas.

Nicolls, R., Hoozemans, F., & Marchand, M. (1999). Increasing #ood risk and wetland losses due to global sea-level rise: regional and global analyses. *Global and Environmental Change,*

156

Njana, M.A, Bollands°as, O.M., Eid, T., Zahabu, E., & Malimbwi, R.E. (2015). Above-and belowground tree biomass models for three mangrove species in Tanzania: a nonlinear mixed effects modelling approach *Ann. Forest Sci.* 1–17.

Nortey, D.D.N., Aheto, D.W., Blay J, Fredrick E.J & Asare, N.K. (2016). Comparative Assessment of Mangrove Biomass and Fish Assemblages in an Urban and Rural Mangrove Wetlands in Ghana. *Society of Wetland Scientists*. DOI 10.1007/s13157-016-0783-2.

Omar, H., Hamzah, K. A., & Ismail, M.H. (2014). L-band ALOSPALSAR for biomass estimation of Matang mangroves, Malaysia. *Remote Sensing of Environment*.

Omo-Irabor, O.O., Olobaniyi, S.B., Akunna, J., Venus, V., Maina, J.M., & Paradzayi, C. (2011). Mangrove vulnerability modelling in parts of Western Niger Delta, Nigeria using satellite images, GIS techniques and Spatial Multi-Criteria Analysis (SMCA). *Environ. Monit. Assess,* 178, 39–51.

Otero, V., Quisthoudt, K., Koedam, N., & Dahdouh-Guebas, F. (2016). Mangroves at Their Limits: Detection and Area Estimation of Mangroves along the Sahara Desert Coast. *Remote Sensing,* 8, 512.

Owe, M., Brubaker, K., Ritchie, J., & Albert, R. (2001). *Remote sensing and Hydrology, 2000.* IAHS.

Page, S.E., Rieley, J.O., & Banks, C.J. (2011) Global and regional importance of the tropical peatland carbon pool. *Glob. Chang. Biol.,* 17, 798–818.

Pereira-Cardenal, S. J., Riegels, N. D., Berry, P. A., Smith, R. G., Yakovlev, A., Siegfried, T. U., & Bauer-Gottwein, P. (2011). Real-time remote

sensing driven river basin modeling using radar altimetry. *Hydrology and Earth sciences*, 241-254. doi:10.5194/hess-15-241-2011.

Peters, E.C., Gassman, N. J., Firman, J. C. Richmond R. H. & Power E. A. (1997). Ecotoxicology of tropical marine ecosystems. *Environmental Toxicology and Chemistry* 16(1), 12-40.

Pimple, U., Simonetti, D., Sitthi, A., Pungkul, S., Leadprathom, K., Skupek, H., Som-ard, J., Gond, V. & Towprayoon, S. (2018). Google Earth Engine Based Three Decadal Landsat Imagery Analysis for Mapping of Mangrove Forests and Its Surroundings in the Trat Province of Thailand. *Journal of Computer and Communications*, 6, 247-264. https://doi.org/10.4236/jcc.2018.61025

Pinki, M., Xue, L., Fatoyinbo, T.E. & Lagomasino, D. (2019). Evaluating Combinations of Sentinel-2 Data and Machine-Learning Algorithms for Mangrove Mapping in West Africa. *Remote Sensing*. 11, 2928; doi:10.3390/rs11242928.

Powell, M.D., Dunion, J.P., Kubatko, E.J., & Pourtaheri, H. (2008). A basin-to channel-scale unstructured grid hurricane storm surge model applied to Southern Louisiana. Mon. *Weather Rev*. 136 (3), 833–864.

Prasad, N. V. (2011). Remote Sensing of Mangrove Wetlands: Concept, Methods, Ecology, Zonation, Dynamics. Germany, VDM Verlag Dr. Müller.

Priya, K.L., Jegathambal, P., & James, E.J. (2012). Hydrodynamic Modeling of Estuaries: A state-of – art. *International Journal of Environmental Sciences*, 3, 0976 – 4402, doi:10.6088 /ijes.2012030131024.

Proisy, C., Couteron, P., & Fromard, F. (2007). Predicting and mapping mangrove biomass from canopy grain analysis using Fourier-based textural ordination of IKONOS images. *Remote Sensing of Environment* 109, 379–392. doi:10.1016/J.RSE.2007.01.009

Qiusheng W. (2018). GIS and Remote Sensing Applications in Wetland Mapping and Monitoring. *Comprehensive Geographic Information Systems*, 2, 140-157; doi:10.1016/B978-0-12-409548-9.10460-9

Rahmatullah, M., Ferdausi, D., Mollik, A., Jahan, R., Chowdhury, M.H. & Haque, W. M. (2010). A survey of medicinal plants used by Kavirajes of Chalna area, Khulna district, Bangladesh. *African Journal of Traditional, Complementary and Alternative Medicines* 7(2).

Ramsar (2005). 'Resolution IX.1 Annex D, Resolution IX.1 Annex D: Ecological 'Outcome-oriented' Indicators for Assessing the Implementation Effectiveness of the Ramsar Convention. Available at http://www.ramsar.org/cda/en/ramsar-documents-resol-resolutionix-1-annex-d/main/ramsar/1-31-107%5E23547_4000_0.[Accessed13 January, 2022].

Ramsar (2012). 'Resolution XI.6, Partnerships and Synergies with Multilateral Environmental Agreements and Other Institutions.' (Ramsar: Bucharest, Romania.) Available at http://www.ramsar.org/cda/en/ramsar-documents- cops-cop11-cop11-resolutions/main/ramsar/1-31-58- 500%5E25837_4000_0_. [Accessed 13 May 2013].

Ranasinghe, R. (2016). Assessing climate change impacts on open sandy coasts: a review. *Earth-Sci. Rev.* 160, 320–332.

159

Rao, A.N. (1987). Mangrove ecosystems of Asia and the Pacific. In: UNDP/UNESCO, RAS/79/002 (ed) Mangroves of Asia and the Pacific, status and management. UNESCO, New Delhi, pp 1–48.

Ratcliff, J., & Smith, J.M. (2011). Sea level rise impacts to military installations in lower Chesapeake Bay. Proc., Solutions to Coastal Disasters 2011, ASCE, Reston, VA, 740–751.

Reed, C.W., Brown, M.E., Sánchez, A., Wu, W., & Buttolph, A.M. (2011). The Coastal Modeling System Flow Model (CMS-Flow): Past and Present, *Journal of Coastal Research*, 59, 1-6.

Rehman, S., Sahana, M., Kumar, P., Ahmed, R., & Sajjad, H. (2020). Assessing hazards induced vulnerability in coastal districts of India using site-specific indicators: An integrated approach. *Geo Journal*.

Rhie, T.M. & Chow, A. (1983). Numerical study of the turbulent flow past an isolated airfoil with trailing-edge separation. *AIAA J.*, 21, 1525–1532.

Rosenqvist, A., Finlayson, M., Lowry, J., & Taylor, D. (2007*b*). The potential of long wavelength satellite borne radar to support implementation of the Ramsar Wetlands Convention. *Journal of Aquatic Conservation: Marine and Freshwater Ecosystems*, 17, 229–244. doi:10.1002/AQC.835.

Rosenqvist, A., Shimada, M., & Watanabe, M. (2007a). ALOS PALSAR: a pathfinder mission for global-scale monitoring of the environment. *IEEE Transactions on Geoscience and Remote Sensing*, 45, 3307–3316. doi:10.1109/TGRS.2007.901027.

Rovai, A.S., Twilley, R.R., Castañeda-Moya, E., Riul, P., Cifuentes-Jara, M., Manrow-Villalobos, M., Horta, P.A., Simonassi, J.C., Fonseca, A.L., & Pagliosa, P.R. (2018). Global controls on carbon storage in mangrove soils. *Nat. Clim. Chang.*, 8, 534–538. S69-S87. doi:10.1016/S0959-3780(99)00019-9.

Saenger, P, & Bellan, M.F. (1995). The mangrove vegetation of the Atlantic Coast of Africa. LET, University of Paul Sabatier, Toulouse.

Saenger, P., & Snedaker, S.C. (1993). Pantropical trends in mangrove aboveground biomass and annual litter fall. *Oecologia* 96:293–299

Salami, A.T., Akinyede, J., & de Gier, A. (2010). A preliminary assessment of NigeriaSat-1 for sustainable mangrove forest monitoring. *International Journal of Applied Earth Observation and Geoinformatics.*, 12, S18–S22.

Sánchez, A., & Wu, W. (2011). A Non-Equilibrium Sediment Transport Model for Coastal Inlets and Navigation Channels. *Journal of Coastal Research*, 59: 39–48.

Sánchez, A., Lihwa, L., Zeki, D., Tanya, B., Mitchell, B., Honghai, L., & Julie D.R. (2014). Coastal Modeling System User Manual. Coastal and Hydraulics Laboratory, U.S. Army Engineer Research and Development Center 3909 Halls Ferry Road, Vicksburg, MS 39180-6199.

Sánchez, A., Wu, W., Beck, T., Li H., Rosati III, J., Thomas, R., Rosati, J., Demirbilek, Z., Brown, M., & Reed, C. (2011). *Verification and Validation of the Coastal Modeling System, Report 3:*

Hydrodynamics. ERDC/CHL-TR-11-10. Vicksburg, MS: U.S. Army Engineer Research and Development Center.

Sassekumar, A., & Loi, J.J. (1983). Litter production in three mangrove forest zones in the Malay Peninsula. *Aquat Bot,* 17, 283–290

Schumann, G., Matgen, P., Hoffmann, L., Hostache, R., Pappenberger, F., & Pfister, L. (2007). Deriving distributed roughness values from satellite radar data for flood inundation modelling. *Journal of Hydrology,* *344*(1-2), 96–111. doi:10.1016/j.jhydrol.2007.06.024.

Sheaves, M., Johnston, R., & Connolly, R. (2010). Temporal dynamics of fish assemblages of natural and artificial tropical estuaries. Marine Ecology Progress Series 410: 143-157.

Shimada, M., & Ohtaki, T. (2010). Generating large-scale high-quality SAR mosaic datasets: application to PALSAR data for global monitoring. IEEE Journal of Selected Topics in Applied Earth Observations and *Remote Sensing*, 3, 637–656. doi:10.1109/JSTARS.2010. 2077619

Shimada, M., Tadono, T., & Rosenqvist, A. (2010). Advanced land observing satellite (ALOS) and monitoring global environmental change. Proceedings of the IEEE 98, 780–799.

Shrestha, S., Miranda, I., Kumar, A., Pardo, M.L.E., Dahal, S., Rashid, T., Remillard, C. & Mishra, D.R. (2019). Identifying and forecasting potential biophysical risk areas within a tropical mangrove ecosystem using multi-sensor data. Int. J. Appl. Earth Obs. Geoinf., 74, 281–294.

Shugart, H.H. (1984). A theory of forest dynamics: the ecological implications of forest succession models. New York, NY: Springer.

Siikamaki, J., Sanchirico, J.N., & Jardine, S.L. (2012). Global economic potential for reducing carbon dioxide emissions from mangrove loss. *Proc. Natl. Acad. Sci.* USA, 109, 14369–14374.

Simard, M., Rivera-Monroy, V.H., Mancera-Pineda, J.E., Castaneda-Moya, E., & Twilley, R.R. (2008). A systematic method for 3d mapping of mangrove forests based on shuttle radar topography mission elevation data, ICESat/GLAS waveforms and field data: application to Cienaga Grande De Santa Marta, Colombia. *Remote Sensing of Environment* 112, 2131–2144. doi:10.1016/J.RSE.2007.10.012.

Simard, M., Zhang, K.Q., Rivera-Monroy, V.H., Ross, M.S., Ruiz, P.L., Castaneda-Moya, E., Twilley, R.R., & Rodriguez, E. (2006). Mapping height and biomass of mangrove forests in Everglades National Park with SRTM elevation data. *Photogrammetric Engineering and Remote Sensing* 72, 299–311. doi:10.143 58/PER S. 72.3.299.

Smith, J.E., Bentley, S.J, Snedden, G., & White, C. (2015). What role do hurricanes play in sediment delivery to subsiding river deltas? *Scientific Reports* 5:17582, https://doi.org/10.1038/srep17582

Smith, J.M., Cialone, M.A., Wamsley, T.V., & McAlpin, T.O. (2010). Potential impact of sea level rise on coastal surges in southeast Louisiana. *Ocean Engineering*, 37(1), 37–47.

Snedaker, C.S., & Lugo, E.A. (1973). The role of mangrove ecosystems in the maintenance of environmental quality and a high productivity of desirable fisheries. Center for Aquatic Sciences, University of Florida, Gainesville.

163

Snedaker, S.C. (1982). Mangrove species zonation: why? In: Sen DN, Rajpurohit KS (eds) Task for vegetation science, vol 2. Dr. Junk Publishers, The Hague, pp 111–125.

Son, N.T., Chen, C.F., Chang, N.B., Chen, C.R., Chang, L.Y. & Thanh, B.X. (2015). Mangrove Mapping and Change Detection in Ca Mau Peninsula, Vietnam, Using Landsat Data and Object-Based Image Analysis. *IEEE Journal of Selected Topics in Applied Earth Observations and Remote Sensing*, 8, 503-510. https://doi. org/10.110 9/JSTARS.2014.2360691.

Spalding, M., Blasco, F. & Field, C. (1997). World mangrove atlas. Okinawa, Japan, International   Society for Mangrove Ecosystems.

Spalding, M., Kainuma, M. & Collins, L. (2010). World Atlas of Mangroves. UK, Earthscan.

Thanh, N.P., Verena, K., & Lukas, W.L. (2020). Land Cover Classification using Google Earth Engine   and Random Forest Classifier-The Role of Image Composition. *Remote Sensing.*, 12: 2411. https://doi. org/10. 3390/rs12152411

The American Society for Photogrammetry and Remote Sensing. (ASPRS, 1990) Accuracy standards for large scale maps. *Photogramm. Eng. Remote Sens.*, 56, 1068–1070.

Thom, B.G. (1982) in *Mangrove Ecosystems in Australia* (ed. Clough, B. F.) 3–17, Australian National Univ. Press, Canberra.

Thomas, N., Bunting, P., Lucas, R., Hardy, A., Rosenqvist, A., & Fatoyinbo, T. (2018). Mapping Mangrove Extent and Change: A Globally Applicable Approach. *Remote Sensing.* 10, 1466.

164

Thomas, N., Lucas, R., Bunting, P., Hardy, A., Rosenqvist, A., & Simard, M. (2017). Distribution and drivers of global mangrove forest change, 1996–2010. *PLoS ONE*, 12, e0179302.

Tianyu, H., YingYing Z., Yanjun S., Yi Z., Guanghui L. & Qinghua, G. (2020). Mapping the Global Mangrove Forest Aboveground Biomass Using Multisource Remote Sensing Data. Remote Sens. 12, 1690; doi:10.3390/rs12101690

Toimil, A., Camus, P., Losada, J., Le Cozannet, R., Nicholls, J., Idier, D., & Maspataud, A. (2020). Climate change-driven coastal erosion modelling in temperate sandy beaches: Methods and uncertainty treatment. *Earth-Science Reviews*, 202, 103110. https://doi.org/10.1016/j.earscirev.2020.103110

Toimil, A., Diaz-Simal, P., Losada, I.J., & Camus, P. (2018). Estimating the risk of loss of beach recreation value under climate change. Tour. Manag. 68, 387–400.

Trepel, M., Michele, D., Luigi, D.C., Marcel, D.W., Silvia, Opitz, L.P., Jesper, P., Nico, M.P., Tiemo, T., Giuseppe, B., Winfrid, K. & Sven-Erik, J. (2000). Models for wetland planning, design and management. EcoSys Bd. 8, 93-137.

Tritinger, A.S. (2015). Numerical Modeling and Analysis of Tidal Variance and Marsh Productivity in the Guana Tolomato Matanzas National Estuarine Research Reserve, Florida. *UNF Graduate Theses and Dissertations*. 569. https://digitalcommons.unf.edu/etd/569

Twilley, R.R. (1982). Litter dynamics and organic carbon exchange in black mangrove (Avicennia germinans) basin forests in a South-West Florida estuary. PhD thesis, University of Florida,   Gainesville

Valiela, I., Bowen, J.L. & York J.K. (2001). Mangrove forests: One of the world's threatened major tropical environments. *BioScience,* 51: 807-885.

Van Doormal, J.P., & Raithby, G.D. (1984). Enhancements of the SIMPLE method for predicting incompressible fluid flows," Numerical Heat Transfer, 7, 147–163.

van Maanen, B., Coco, G., & Bryan, K.R. (2015). On the eco-geomorphological feedbacks that control tidal channel network evolution in a sandy mangrove setting. *Proc. R. Soc. A* 471: 20150115. http://dx.doi. org/10.1098/rspa.2015.0115

Van Maanen, B., Coco, G., & Bryan, K.R. (2013). Modelling the effects of tidal range and initial bathymetry on the morphological evolution of tidal embayments. *Geomorphology* 191, 23–34. doi:10.1016/j.geomorph. 2013.02.023.

Van, P., Popescu, I., Van Griensven, A., Solomatine, D., Trung, N., & Green, A. (2012). A study of the climate change impacts on fluvial flood propagation in the Vietnamese Mekong Delta. *Hydrology and Earth Systems Science, 16,* 4637-4649. doi:10.5194/hess-16-4637-2012.

Vitousek, S., Barnard, P.L., Fletcher, C.H., Frazer, N., Erikson, L., Storlazzi, C.D. (2017). Doubling of coastal flooding frequency within decades due to sea-level rise. *Sci. Rep.* 7 (1), 1399.

Vousdoukas, M.I., Mentashi, L., Voukouvalas, E., Verlaan, M., Jevrejeva, S., Jackson, L.P., &   Feyen, L. (2018). Global probabilistic projections of extreme sea levels show intensification of coastal flood hazard. *Nat. Commun.* 9, 2360.

Wadey, M., Brown, S., Nicholls, R.J., & Haigh, I. (2017). Coastal flooding in the Maldives: An assessment of historic events and their implications. Nat. Hazards, 89, 131–159.

Wainwright, D.J., Ranasinghe, R., Callaghan, D.P., Woodroffe, C.D., Jongejan, R., Dougherty,   A.J., Rogers, K., & Cowell, P.J. (2015). Moving from deterministic towards probabilistic coastal hazard and risk assessment: development of a modelling framework and application to Narrabeen Beach, New South Wales, Australia. Coast. Eng. 96, 92–99.

Walsh, K.J.E., Betts, H., Church, J., Pittock, A.B., McInnes, K.L., Jackett, D.R., & McDougall, T.J. (2004). Using Sea Level Rise Projections for Urban Planning in Australia. Journal of Coastal Research., 20, 586–598.

Wamsley, T.V., Cialone, M.C., Smith, J.M., Ebersole, B.A., & Grzegorzewski, A.S. (2009). Influence of landscape restoration and degradation on storm surge and waves in southern Louisiana. *J. Nat. Hazards*, 51(1), 207–224.

Wang, L., Jia, M., Yin, D., & Tian, J. (2019). A review of remote sensing for mangrove forests: 1956–2018. Remote Sens. Environ. 231, 111223.

Wang, L., Silvan-Cardenas, J. L., & Sousa, W. P. (2008). Neural network classification of mangrove species from multi-seasonal IKONOS

imagery. *Photogrammetric Engineering and Remote Sensing* 74, 921–927. doi:10.14358/PERS.74.7.921

Wang, L., Sousa-Filho, W. P., & Gong, P. (2004). Integration of object-based and pixel-based classification for mapping mangroves with IKONOS imagery. *International Journal of Remote Sensing* **25**, 5655–5668. doi:10.1080/014311602331291215

Wenger, S.M.B. (2016). Evaluation of SfM against Traditional Stereo-photogrammetry and Lidar Techniques for DSM Creation in Various Land Cover Areas. Ph.D. Thesis, Stellenbosch University, Stellenbosch, South Africa.

Westerink, J.J., Luettich, R.A., Jr., Feyen, J.C., Atkinson, J.H., Dawson, C., Powell, M.D., Dunion, J.P., Roberts, H.J., Kubatko, E.J. & Pourtaheri H. (2008). A Basin to Channel Scale Unstructured Grid Hurricane Storm Surge Model as Implemented for Southern Louisiana, *Monthly Weather Review*, 136, 833-864

Wijedasa, L.S., Sloan, S., Michelakis, D.G., & Clements, G.R. (2012). Overcoming Limitations with Landsat Imagery for Mapping of Peat Swamp Forests in Sundaland. *Remote Sensing*, 4, 2595-2618. https://doi.org/10.3390/rs4092595

Williams, S., & Ismail, N. (2015). Climate Change, Coastal Vulnerability and the Need for Adaptation Alternatives: Planning and Design Examples from Egypt and the USA. *Marine Science and ENgineering*, *3*(2015), 591-606. doi:10.3390/jmse3030591

Wolanski, E. (2007). Estuarine ecohydrology. Amsterdam, The Netherlands, Elsevier.

Woldemicheal, A., Degu, A., Siddique-E-Akbor, A., & Hossain, F. (2010). Role of Land–Water Classification and Manning's Roughness Parameter in Space-Borne Estimation of Discharge for Braided Rivers: A Case Study of the Brahmaputra River in Bangladesh. *Ieee journal of selected topics in applied earth observations and remote sensing.* Doi:10.1109/jstars.2010.2050579

Wong, P.P., Losada, I.J., Gattuso, J.P., Hinkel, J., Khattabi, A., McInnes, K.L., Saito, Y. & Sallenger, A., (2014). Coastal systems and low-lying areas. In: Field, C.B. (Ed.), Climate Change: Impacts, Adaptation, and Vulnerability; Part A: Global and Sectoral Aspects. Contribution of Working Group II to the Fifth Assessment Report of the Intergovernmental Panel on Climate Change. Cambridge University Press, Cambridge, UK; New York, NY, USA, pp. 361–409.

Woodroffe, C.D, Bardsley, K.N., Ward, PJ. & Hanley, J.R. (1988). Production of mangrove litter in a macrotidal embayment, Darwin Harbour, N.T., Australia. *Estuary Coastal Shelf Science,* 26, 581–598

World Mangrove Network (2012). Western Indian Ocean Mangrove Network/United States Forest Service Workshop Report, Maputo, Mozambique.

Wu, W., Sánchez, A., & Mingliang, Z. (2011). An implicit 2-D shallow wa-ter flow model on an unstructured quadtree rectangular grid, *Journal of Coastal Research.*

Xie, D., Schwarz, C., Brückner, M.Z.M., Kleinhans, M.G., Urrego, D.H., Zhou, Z., & van Maanen, B. (2020). Mangrove diversity loss under sea-level rise triggered by bio-morpho-dynamic feedbacks and

anthropogenic pressures. *Environmental Research Letters,* 15:114033. https://doi.org/10.1088/1748-9326/abc122

Yool, A. & Fasham, M.J. (2001). An examination of the 'continental shelf pump in an open ocean general circulation model. Global Biogeochem. Cy. 15 (4),   831–844.

Zhang, C., Kovacs, J.M., Liu, Y., Flores-Verdugo, F. & Flores-de-Santiago, F. (2014). Separating Mangrove Species and Conditions Using Laboratory Hyperspectral Data: A Case Study of a Degraded Mangrove Forest of the Mexican Pacific. Remote Sensing, 6, 11673-11688. https://doi.org/10.3390/rs61211673

Zhu, Z., & Woodcock, C.E. (2012). Continuous monitoring of forest disturbance using all available Landsat imagery. *Remote Sensing of Environment,*   122,   75–91.   doi:10.1016/J.RSE.2011.10.030 www.publish.

Zundel, A.K., (2006). Surface-water Modeling System reference manual – Version 9.0. Brigham Young University Environmental Modeling Research Laboratory, Provo, UT.

Appendix 1: Dynamic vegetation model parameters

S/N	Growth Parameter	Value	Unit	Source
1	Growth constant G	162	cm^{-yr}	Berger and Hildenbrandt, 2000; Chen and Twilley, 1998
2	Growth constant b2	48.04	-	Berger and Hildenbrandt, 2000; Chen and Twilley, 1998
3	Growth constant b3	0.172	-	Berger and Hildenbrandt, 2000; Chen and Twilley, 1998
4	Fitness function constant a	-16	-	Xie et al., 2020
5	Fitness function constant b	16	-	Xie et al., 2020
6	Fitness function constant c	-3	-	Xie et al., 2020

171

Appendix 2:

1.// Load Sentinel-1 C-band SAR Ground Range collection (log scale, VV, descending)

```
var collectionVV = ee.ImageCollection('COPERNICUS/S1_GRD')
.filter(ee.Filter.eq('instrumentMode', 'IW'))
.filter(ee.Filter.listContains('transmitterReceiverPolarisation', 'VV'))
.filter(ee.Filter.eq('orbitProperties_pass', 'DESCENDING'))
.filterMetadata('resolution_meters', 'equals' , 10)
.filterBounds(roi)
.select('VV');
```

// Load Sentinel-1 C-band SAR Ground Range collection (log scale, VH, descending)

```
var collectionVH = ee.ImageCollection('COPERNICUS/S1_GRD')
.filter(ee.Filter.eq('instrumentMode', 'IW'))
.filter(ee.Filter.listContains('transmitterReceiverPolarisation', 'VH'))
.filter(ee.Filter.eq('orbitProperties_pass', 'DESCENDING'))
.filterMetadata('resolution_meters', 'equals' , 10)
.filterBounds(roi)
.select('VH');
```

print(collectionVV, 'Collection VH');

2.//Filter by date

```
var SARVV = collectionVV.filterDate('2019-08-01', '2019-08-10').mosaic();
var SARVH = collectionVH.filterDate('2019-08-01', '2019-08-10').mosaic();
```

3.// Add the SAR images to "layers" in order to display them

```
Map.centerObject(roi, 7);
Map.addLayer(SARVV, {min:-15,max:0}, 'SAR VV', 0);
Map.addLayer(SARVH, {min:-25,max:0}, 'SAR VH', 0);
```

4.// Function to cloud mask from the pixel QA band of Landsat 8 SR data.

```
function maskClouds(image) {
```

172

```
// Bits 3 and 5 are cloud shadow and cloud, respectively.
 var cloudShadowBitMask = ee.Number(2).pow(3).int();
 var cloudsBitMask = ee.Number(2).pow(5).int();


 // Get the pixel QA band.
 var qa = image.select('pixel_qa');


 // Both flags should be set to zero, indicating clear conditions.
 var mask =
qa.bitwiseAnd(cloudShadowBitMask).eq(0).and(qa.bitwiseAnd(cloudsBitMas
k).eq(0));


 // Return the masked image, scaled to [0, 1].
 return image.updateMask(mask).divide(10000).copyProperties(image,
["system:time_start"]);

}

5.//Add Spectral Indices for Mangrove Mapping using Landsat 8 Imagery
var addIndicesL8 = function(img) {
 // NDVI
 var ndvi = img.normalizedDifference(['B5','B4']).rename('NDVI');
 // NDMI (Normalized Difference Mangrove Index - Shi et al 2016 - New
spectral metrics for mangrove forest identification)
 var ndmi = img.normalizedDifference(['B7','B3']).rename('NDMI');
 // MNDWI (Modified Normalized Difference Water Index - Hanqiu Xu,
2006)
 var mndwi = img.normalizedDifference(['B3','B6']).rename('MNDWI');
 // SR (Simple Ratio)
 var sr = img.select('B5').divide(img.select('B4')).rename('SR');
 // Band Ratio 54
 var ratio54 = img.select('B6').divide(img.select('B5')).rename('R54');
 // Band Ratio 35
```

```
var ratio35 = img.select('B4').divide(img.select('B6')).rename('R35');
// GCVI
var gcvi = img.expression('(NIR/GREEN)-1',{
  'NIR':img.select('B5'),
  'GREEN':img.select('B3')
}).rename('GCVI');
return img
  .addBands(ndvi)
  .addBands(ndmi)
  .addBands(mndwi)
  .addBands(sr)
  .addBands(ratio54)
  .addBands(ratio35)
  .addBands(gcvi);
};

6. // Filter Landsat data by Date and Region
var year = 2019;
var startDate = (year-1)+'-01-01';
var endDate = (year+1)+'-12-31';


// Apply filters and masks to Landsat 8 imagery
var l8 = L8.filterDate(startDate,endDate)


// Mask for clouds and cloud shadows
    .map(maskClouds)


//Add the indices
    .map(addIndicesL8)
7. // Composite the Landsat image collection per pixel, per-band basis using
.median()
```

174

```
var composite = 18

        // Uses the median reducer

        .median()

        // Clips the composite to our area of interest

        .clip(roi);
```

8. // Mask to areas of low elevation and high NDVI and MNDWI

// Clip SRTM data to region

```
var srtmClip = SRTM.clip(roi);
```

//Mask to elevations less than 65 meters

```
var elevationMask = srtmClip.lt(45);
```

//Used the NDVI and MNDWI bands to create masks

```
var NDVIMask = composite.select('NDVI').gt(0.25);

var MNDWIMask = composite.select('MNDWI').gt(-0.50);
```

//Apply the masks

```
var compositeNew = composite

            .updateMask(NDVIMask)

            .updateMask(MNDWIMask)

            .updateMask(elevationMask)
```

9. // Display results

//Select bands and parameters for visualization

```
var visPar = {bands:['B5','B6','B4'], min: 0, max: 0.35};
```

//Add layer to map

```
Map.addLayer(compositeNew.clip(roi), visPar, 'Landsat Composite 2019')
```

10. //Apply filter to reduce speckle

```
var SMOOTHING_RADIUS = 50;
```

175

```
var SARVV_filtered = SARVV.focal_mean(SMOOTHING_RADIUS, 'circle',
'meters');

var SARVH_filtered = SARVH.focal_mean(SMOOTHING_RADIUS, 'circle',
'meters');

//Display the SAR filtered images

Map.addLayer(SARVV_filtered, {min:-15,max:0}, 'SAR VV Filtered',0);

Map.addLayer(SARVH_filtered, {min:-25,max:0}, 'SAR VH Filtered',0);

//Create Training Samples and Merge Feature Collections

var                    newfc                    =

Open_water.merge(Vegetation_Wetland).merge(Mangroves).merge(Bare_lan

d);

11. //Define the bands you want to include in the model

var bands = ['B5','B6','B4','NDVI','MNDWI','SR','GCVI']

//Create a variable called image to select the bands of interest and clip to
geometry

var image = compositeNew.select(bands).clip(roi)

//Assemble samples for the model

var samples = image.sampleRegions({
    collection: newfc, // Set of geometries selected for training
    properties: ['landcover'], // Label from each geometry
    scale: 30 // Make each sample the same size as Landsat pixel
}).randomColumn('random'); // creates a column with random numbers

//Here we randomly split our samples to set some aside for testing our model's
accuracy
// using the "random" column we created
var split = 0.8; // Roughly 80% for training, 20% for testing.
```

176

```
var training = samples.filter(ee.Filter.lt('random', split)); //Subset training data
var testing = samples.filter(ee.Filter.gte('random', split)); //Subset testing data

//Print these variables to see how much training and testing data you are using
    print('Samples n =', samples.aggregate_count('.all'));
    print('Training n =', training.aggregate_count('.all'));
    print('Testing n =', testing.aggregate_count('.all'));

12. //Define the SAR bands to train your data
var final = ee.Image.cat(SARVV_filtered,SARVH_filtered);
var bands = ['VH','VV'];
var training = final.select(bands).sampleRegions({
    collection: newfc,
    properties: ['landcover'],
    scale: 30 });
//Train the classifier
var classifier = ee.Classifier.randomForest().train({
    features: training,
    classProperty: 'landcover',
    inputProperties: bands
});

//Run the Classification
var classified = final.select(bands).classify(classifier);

//Display the Classification
Map.addLayer(classified,
{min: 1, max: 7, palette: ['1667fa', 'ee9a1c', '04bd23', '37fe05']},
'SAR Classification');
// Create a confusion matrix representing resubstitution accuracy.
```

177

```
print('RF- SAR error matrix: ', classifier.confusionMatrix());
print('RF- SAR accuracy: ', classifier.confusionMatrix().accuracy());


//7.1) Creating Stratified Random Samples
var stratSamples = classified.stratifiedSample({
            numPoints:150,        //Number of points per class
            classBand: 'classification',
            region:roi,
            scale: 30,
            geometries:true
    });


//Add a 15m Radius buffer around each point
var stratBuff = function(feature) {
    var num = feature.get('classification');

    return feature.buffer(15).set('classification', num);
    };


//Map the buffer across all points (see export code below
var stratPoints = stratSamples.map(stratBuff)

13. //Repeat for Landsat
//Define the Landsat bands to train your data
var bandsl8 = ['B1', 'B2', 'B3', 'B4', 'B5', 'B6', 'B7','NDVI' ];
var trainingl8 = composite.select(bandsl8).sampleRegions({
    collection: newfc,
    properties: ['landcover'],
    scale: 30
});
```

178

```
//Train the classifier
var classifierl8 = ee.Classifier.randomForest().train({
    features: trainingl8,
    classProperty: 'landcover',
    inputProperties: bandsl8
});

//Run the Classification
var classifiedl8 = composite.select(bandsl8).classify(classifierl8);

//Display the Classification
Map.addLayer(classifiedl8,
{min: 1, max: 7, palette: ['1667fa', 'ee9a1c', '04bd23', '37fe05']},
'Optical Classification');

// Create a confusion matrix representing resubstitution accuracy.
print('RF-L8 error matrix: ', classifierl8.confusionMatrix());
print('RF-L8 accuracy: ', classifierl8.confusionMatrix().accuracy());

//7.1) Creating Stratified Random Samples
```

Apendix 3: Code for Estimation of Mangrove Stand Height

```
1. //Clip the radar images and elevation to the mangrove vector files
var mangroves_2007_HH = dB_2007_HH.clip(mangroves);
var mangroves_2007_HV = dB_2007_HV.clip(mangroves);
var mangroves_2017_HH = dB_2017_HH.clip(mangroves);
var mangroves_2017_HV = dB_2017_HV.clip(mangroves);
var mangroves_1996_HH = dB_1996_HH.clip(mangroves);
var elevation = srtm.clip(mangroves)
```

179

2. //Add the images to the layers bar

Map.addLayer(mangroves_2007_HH ,{min:-15,max:-3}, 'Mangrove 2007 HH', 0);

Map.addLayer(mangroves_2007_HV ,{min:-27,max:-5}, 'Mangrove_2007 HV', 0);

Map.addLayer(mangroves_2017_HH ,{min:-15,max:-3}, 'Mangrove_2017 HH', 0);

Map.addLayer(mangroves_2017_HV ,{min:-27,max:-5}, 'Mangrove_2017 HV', 0);

Map.addLayer(mangroves_1996_HH ,{min:-25,max:0}, 'Mangrove_1997 HH', 0);

Map.addLayer(elevation ,{min:-5,max:30}, 'Elevation', 0);

3. //Calculate maximum canopy height from SRTM dem 1.697*SRTM

var canopy_height= elevation.multiply(1.697);

4. //add the maximum canopy height to the layers bar

Map.addLayer(canopy_height ,{min:0,max:1000}, 'Mangrove Height-SRTM', 0);

Appendix 4: Code for Estimation of Mangrove Above Ground Biomass

1. //Calculate above ground biomass from SRTM canopy height $3.25*(1.08*SRTM)^{1.53}$

var biomass_height= elevation.multiply(1.08).pow(1.53).multiply(3.25);

2. //add the biomass image to the layers bar

Map.addLayer(biomass_height ,{min:0,max:1000}, 'Mangrove Biomass-SRTM', 0);